AFWAL-TR-81-4021

ADVANCED SILICON MATERIAL DEVELOPMENT FOR LADIR

H. Kimura, M.H. Young, G.D. Robertson
and O.J. Marsh

Hughes Research Laboratories

3011 Malibu Canyon Road

Malibu, CA 90265

December 1981

MATERIALS LABORATORY

AIR FORCE WRIGHT AERONAUTICAL LABORATORIES

AIR FORCE SYSTEMS COMMAND

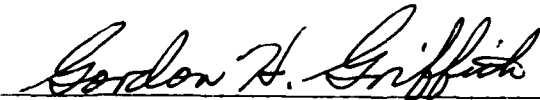Wright–Patterson AFB, OH 45433

NOV 2 1982

A

82 11 02 096

BLANK PAGES
IN THIS
DOCUMENT
WERE NOT
FILMED

NOTICE

When Government drawings, specifications, or other data are used for any purpose
other than in connection with a definitely related Government procurement operation,
the United States Government thereby incurs no responsibility nor any obligation
whatsoever; and the fact that the government may have formulated, furnished, or in
any way supplied the said drawings, specifications, or other data, is not to be
regarded by implication or otherwise as in any manner licensing the holder or any
other person or corporation, or conveying any rights or permission to manufacture,
use, or sell any patented invention that may in any way be related thereto.

This report has been reviewed by the Office of Public Affairs (ASD/PA) and is
releasable to the National Technical Information Service (NTIS). At NTIS, it will
be available to the general public, including foreign nations.

This technical report has been reviewed and is approved for publication.

GORDON H. GRIFFITH
Project Engineer

G. EDWARD KUHL, Chief
Laser & Optical Materials Branch
Electromagnetic Materials Division

FOR THE COMMANDER

MERRILL L. MINGES, Chief
Electromagnetic Materials Division
Materials Laboratory
Air Force Wright Aeronautical Laboratories

REPORT DOCUMENTATION PAGE		READ INSTRUCTIONS BEFORE COMPLETING FORM
1. REPORT NUMBER AFWAL-TR-81-4021	2. GOVT ACCESSION NO. AD-A12 0980	3. RECIPIENT'S CATALOG NUMBER
4. TITLE (and Subtitle) ADVANCED SILICON MATERIAL DEVELOPMENT FOR LADIR		5. TYPE OF REPORT & PERIOD COVERED Final Report 15 Aug 1978 – 1 Sep 1981
		6. PERFORMING ORG. REPORT NUMBER
7. AUTHOR(s) H. Kimura, M.H. Young, G.D. Robertson, and O.J. Marsh		8. CONTRACT OR GRANT NUMBER(s) F33615-78-C-5062
9. PERFORMING ORGANIZATION NAME AND ADDRESS Hughes Research Laboratories 3011 Malibu Canyon Road Malibu, CA 90265		10. PROGRAM ELEMENT, PROJECT, TASK AREA & WORK UNIT NUMBERS PE62102F, Proj. 2423, W.U. 24230114
11. CONTROLLING OFFICE NAME AND ADDRESS Materials Laboratory (AFWAL/MLPO) Air Force Wright Aeronautical Laboratories Air Force Systems Command Wright-Patterson AFB, OH 45433		12. REPORT DATE December 1981
		13. NUMBER OF PAGES 149
14. MONITORING AGENCY NAME & ADDRESS(if different from Controlling Office)		15. SECURITY CLASS. (of this report) UNCLASSIFIED
		15a. DECLASSIFICATION DOWNGRADING SCHEDULE

16. DISTRIBUTION STATEMENT (of this Report)

Approved for public release; distribution unlimited.

17. DISTRIBUTION STATEMENT (of the abstract entered in Block 20, if different from Report)

18. SUPPLEMENTARY NOTES

19. KEY WORDS (Continue on reverse side if necessary and identify by block number)

Float-zoned silicon, IR detector material, Gallium-doped silicon, LADIR materials study, Diffusion during growth of Si:Ga

20. ABSTRACT (Continue on reverse side if necessary and identify by block number)

Results from several float-zoned <100> Si:Ga crystals show that the uniformity of Ga distribution improves as the growth rate is decreased and the rotation rate during growth is increased, in agreement with diffusion theory. For 2-in. diameter crystals, the lowest growth rate that will yield dislocation-free crystals in our equipment is about 3 mm/min. The onset of mechanical resonance and vibration of the growing crystal ___

supported on its slender seed crystal limits the rotation rate to about 10 rpm. Crystals grown under these conditions, and later neutron transmutation counterdoped, show very good spatial uniformity of both major and compensating dopants. Thermal diffusion studies showed that annealing at 1300°C for several hundred hours also reduced Ga concentration fluctuations.

Longitudinal detectors were fabricated from processed FPA wafers covering a Ga concentration range from 0.2 to 2 x 10^{17} Ga atoms/cm^3. Experimentally determined quantum efficiency and D* for these detectors agreed very well with theoretical predictions based on a model developed by Baron and Szmulowicz. The value of this model to future FLIR system design is now firmly established.

The optical absorption cross section from 2.5 to 16.5 μm has been measured for Si:Ga in Ga concentrations useful for IR detection.

Appendices cover useful background information on float-zone crystal growth, neutron transmutation doping for improved uniformity, and impurity band conduction in Si:Ga.

PREFACE

TABLE OF CONTENTS

LIST OF ILLUSTRATIONS

8

11

SECTION 1

INTRODUCTION AND SUMMARY

The success of extrinsic Si monolithic focal plane arrays, in which
a single chip of Si material incorporates both a high density of IR-
sensitive detectors and the associated signal-processing circuitry,
depends on the availability of Si material with sufficiently uniform IR
responsivity. In contrast to detector arrays assembled from discrete
components, there is no possibility of selecting or adjusting individual
detector elements; uniformity must be built into the extrinsic Si sub-
strate material at the wafer stage of processing. There is a limited
possibility of compensating for nonuniformities by off-plane processing,
but this is feasible only to the extent that the nonuniformities are
small to begin with.

A precise specification of the required degree of uniformity is not
yet available, but it is clear that improvements in the state of the art
are desirable. The objective of the work reported here was to carry out
crystal growth and doping operations in ways that would result in the
most nearly uniform distribution of the significant impurities. The
emphasis was on Ga-doped Si. In Si:Ga detectors, the Ga concentration
affects responsivity through the quantum efficiency; since the detector
elements are likely to be fairly thick (say 0.5 mm) along the light path,
nonuniformities in Ga concentration on a smaller spatial scale may aver-
age out. The concentrations of compensating donors (mostly P) and of B
influence the responsivity through their effect on the photoconductive
lifetime and hence the photoconductive gain. In the usual operating re-
gime of Si:Ga detectors, the responsivity is proportional to $(N_P - N_B)^{-1}$.
To achieve the operating temperature appropriate to Ga-doped Si rather
than the much lower temperature necessary for B-dominated material, N_P
must exceed N_B. However, the amount by which N_P exceeds N_B should be
small enough to provide a high responsivity without being so small that
the nonuniformities of P and B separately are large compared to the

13

difference between their concentrations. Unfortunately, the best
present-day technology for Si results in an irreducible residual concen-
tration of B. Although this concentration is small, it constitutes a
lower limit for the P concentration.

Like B, P is present in the high-purity polycrystalline Si that is
the starting material for high-quality Si crystal growth. It differs
from B, however, in that it can be removed by _ succession of vacuum
float zone operations, so that a crystal can be prepared that is essen-
tially free of P. By means of neutron transmutation doping (NTD), an
inherently uniform and precise doping method, P can be reintroduced into
the crystal after the final growth step. We have verified on this con-
tract that the distribution of B as a result of growth is quite uniform,
so that $N_P - N_B$ can also be uniform. Our strategy, therefore, has been
to explore modifications in the growth process to make the Ga distribu-
tion as uniform as possible. Our proposed process is to remove P from
low-B polycrystalline silicon by successive vacuum zoning, add Ga in a
final doping zone pass with growth parameters chosen for optimum Ga uni-
formity, and add P uniformly by NTD with a dose chosen to achieve a
specified value of $N_P - N_B$ in the final material.

During the first year of the program, we emphasized the study of
the effect of float zone growth parameter variations on dopant distribu-
tion. Four 2-in.-diameter crystals, three Ga doped and one B doped,
were grown in the <100> direction. In two of the Ga-doped crystals,
Z108Ga and Z118Ga, various combinations of growth and rotation rates
were tried to examine their effects on the radial Ga distribution.
Crystal Z144B is a B-doped crystal grown to assess the uniformity of B
distribution. This is important from the standpoint of achieving a low
and uniform value of $N_P - N_B$. Crystal Z095Ga is a Ga-doped crystal
grown with a cooling ring placed near the growth interface to see if
the thermal profile at the interface can be altered sufficiently to
improve the uniformity. The uniformity on a microscopic scale was
assessed by measuring the spreading resistance across the sample in the

14

radial direction with a Mazur ASR-210 Automatic Spreading Resistance Probe in the single- and double-probe modes. The two-probe mode was used so that the spreading resistances of two contact points separated by a distance of ~ 400 μm could be measured across the sample. Resistivities of the sample at 5-mm intervals were also measured by the four-point-probe method to give an indication of average doping over a large interval. The results of the measurements made indicate that spatial fluctuations in Ga concentration can be significantly reduced by the proper choice of growth and rotation rates. However, those conditions leading to reduced Ga fluctuations (i.e., a high rotation rate and a low growth rate) are also those under which it is very difficult to maintain single-crystal growth. In the second year of this program, continued growth studies provided us with a better understanding of the segregation theory and the more detailed nature of the complex interface structure. Although other parameters, such as eccentric rotation and coil design, might have been studied, we believed that continued exploration of the effects of the growth rate and rotation rate of the crystal would be the most rewarding.

In crystal Z180Ga, we tried still slower growth rates (pull rates) and faster rotation rates, conditions that should yield better uniformity according to the segregation theory. In crystal Z179Ga, we examined the theory by exploring the other extreme by maximizing the growth rate and minimizing the crystal rotation rate. The complex morphological feature which disrupts rotation striations in a feathering pattern was also examined. We also carried out thermal diffusion experiments and showed that uniformity can be further implemented by the post-growth annealing process. Using the growth processes developed in this program we have subsequently grown several Si:Ga crystals of very high doping uniformity. Results are given for two of these in Section 4. This program has established a lower limit in our equipment of about 3 mm/min for the growth of dislocation-free crystals.

15

During this program, data on the optical absorption cross section
of Ga in Si appeared in the literature. Because those data were at vari-
ance with long-accepted values, we made independent measurements of the
cross section for samples with Ga concentrations suitable for IR detec-
tors. These new measurements are in good agreement with those that have
long been used for detector design and analysis. We estimate that these
measurements are accurate to within ±15%.

Just before the close of the crystal growth experiments, an oppor-
tunity arose to examine both the material properties and detector per-
formance for several Si:Ga crystals which had been grown and processed
for FTD/LADIR-type applications. The contract was extended so that
comparisons could be made between theory and FPA behavior. The results
were most encouraging and showed that the longitudinal detector model
of Baron and Szmulowicz predicts quantum efficiency and detectivity very
well for typical FLIR conditions. At high Ga concentrations, evidence
of impurity band conduction was observed; this conduction mechanism is
being studied further in an on-going program with the Materials Laboratory.

To furnish additional background on three technical issues of key
importance to extrinsic silicon detector arrays, we have included three
appendices. Appendix A describes the float-zone crystal growth process
and briefly discusses the factors that control the uniformity of the
gallium concentration in a doped single crystal of Si:Ga. Appendix B
presents information obtained prior to this program which shows the ben-
eficial effects of counterdoping by neutron transmutation as mentioned
above. Appendix C contains some experimental observations of impurity
band conduction in Si:Ga.

SECTION 2

TECHNICAL RESULTS

A. SEGREGATION THEORY

Compositional striations result mainly from microscopic growth rate fluctuations arising from the rotation of the crystal in an asymmetric thermal field. The growing crystal interface experiences accelerating and decelerating growth rate fluctuations as it rotates in an asymmetric thermal field. The solute in the diffusion boundary layer responds to such variations in the instantaneous microscopic growth rate and segregates in phase with the rotation to give rise to compositional variations in the crystal.

The solute distributes itself between the crystal and the melt according to the thermodynamically determined coefficient — the equilibrium distribution coefficient k. For a solute having $k < 1$, the solute accumulates in the boundary layer as it is rejected from the crystal. A concentration gradient, therefore, is established in the diffusion boundary layer, whose slope is determined by the net rate of accumulation and depletion of solute in the boundary layer. The depletion rate of solute is determined by the rate at which solute is diffused through the boundary layer to the bulk melt, where it is transported away by convection currents. Clearly then, the steady-state segregation behavior of solute depends on the microscopic growth rate and the thickness of the diffusion boundary layer.

Superimposed on the complex distribution of solute in a striated pattern is the less periodic and more random distribution of solute arising from the temporal (transient) and spatial variations in the thermal convection flows. The amplitudes of compositional variations arising from transient convection flows are less pronounced than that from the rotation of the crystal and appear as higher harmonic oscillations on the periodically varying spreading resistance fluctuations. Crystals are grown under forced convections to minimize the effect from the transient convection flows.

17

The distribution of solute between the solid and the diffusion
boundary layer at the crystal liquid boundary is determined by the equi-
librium distribution coefficient k, which differs from the effective
distribution coefficient k_e. The effective distribution coefficient is
more commonly used because it is the ratio between two measurable quan-
tities: the concentration in the solid over that in the bulk melt.
Burton, Prim, and Slichter (BPS)[1] derived the well-known expression from
the diffusion equations for the effective distribution coefficient k_e
under a steady-state condition:

$$k_e = \frac{k}{k + (1-k)\exp(-R\delta/D)} ,$$ (1)

where R is the microscopic growth rate, δ is the thickness of the inter-
facial diffusion boundary layer, and D is the diffusion coefficient of
solute in the melt. Using the above expression, k_e can be calculated
knowing the microscopic growth rate and the thickness of the boundary
layer.

The thickness of the diffusion boundary layer can be estimated from
the Cochran[2] analysis:

$$\delta = 1.6D^{1/3}\nu^{1/6}\omega^{-1/2} ,$$ (2)

where ν is the kinematic viscosity, and ω is the angular rotation rate
in radians per second. The expression was derived by Cochran for an
infinite disk rotating in an isothermal liquid with no convections or
edge effects. Under actual growth conditions, the thickness tends to be
smaller due to thermal convection flows and edge effects.

---

[1] J.A. Burton, R.C. Prim, and W.P. Slichter, J. Chem. Phys. 21 1987
(1953)

[2] W.G. Cochran, Proc. Cambridge Phil. Soc. 30, 365 (1934)

Another expression which may better describe the compositional variations, $\Delta C/C$, with growth rate variations for float-zone growth was derived[3,4] for high-frequency growth rate fluctuations ($\omega \gg D/\delta^2$):

$$\frac{\Delta C/C}{\Delta R/R} = (1-k) \frac{R\delta/D}{(2\omega\delta^2/D)^{1/2}} . \qquad (3)$$

The above expression may be more applicable to float-zone growth for the ranges in which we can vary the growth rate and rotation rate. Figure 1 shows compositional variations with growth rate fluctuations as a function of rotation rate in rpm for the three microscopic growth rates. It shows that, to minimize the compositional variations with growth rate fluctuations, the growth rate must be minimized and the rotation rate maximized. Our approach to achieving compositional uniformity will be directed toward finding the optimum combination of growth rate and rotation rate.

Since no attempts were made to determine the microscopic growth rate by the interface demarcation technique, either by the Peltier effect[5] or vibrations,[6] the term growth rate used throughout this report refers to the pull rate of the crystal and not to the instantaneous microscopic growth rate unless it is so indicated.

---

[3] D.T.J. Hurle and E. Jakeman, J. Cryst. Growth 5, 227 (1969)

[4] J.R. Carruthers and A.F. Witt, "Transient Segregation Effects in Czochralski Growth," BTL Tech. Memo. TM 74-1522-6 (1974)

[5] A.F. Witt and H.C. Gatos, J. Electrochem. Soc. 115 (1968)

[6] A.F. Witt and H.C. Gatos, J. Electrochem. Soc. 119, 1218 (1972)

$$\frac{\Delta C/C}{\Delta R/R} = (1 - k) \ \frac{R\delta/D}{[2\omega\delta^2/D]^{1/2}}$$
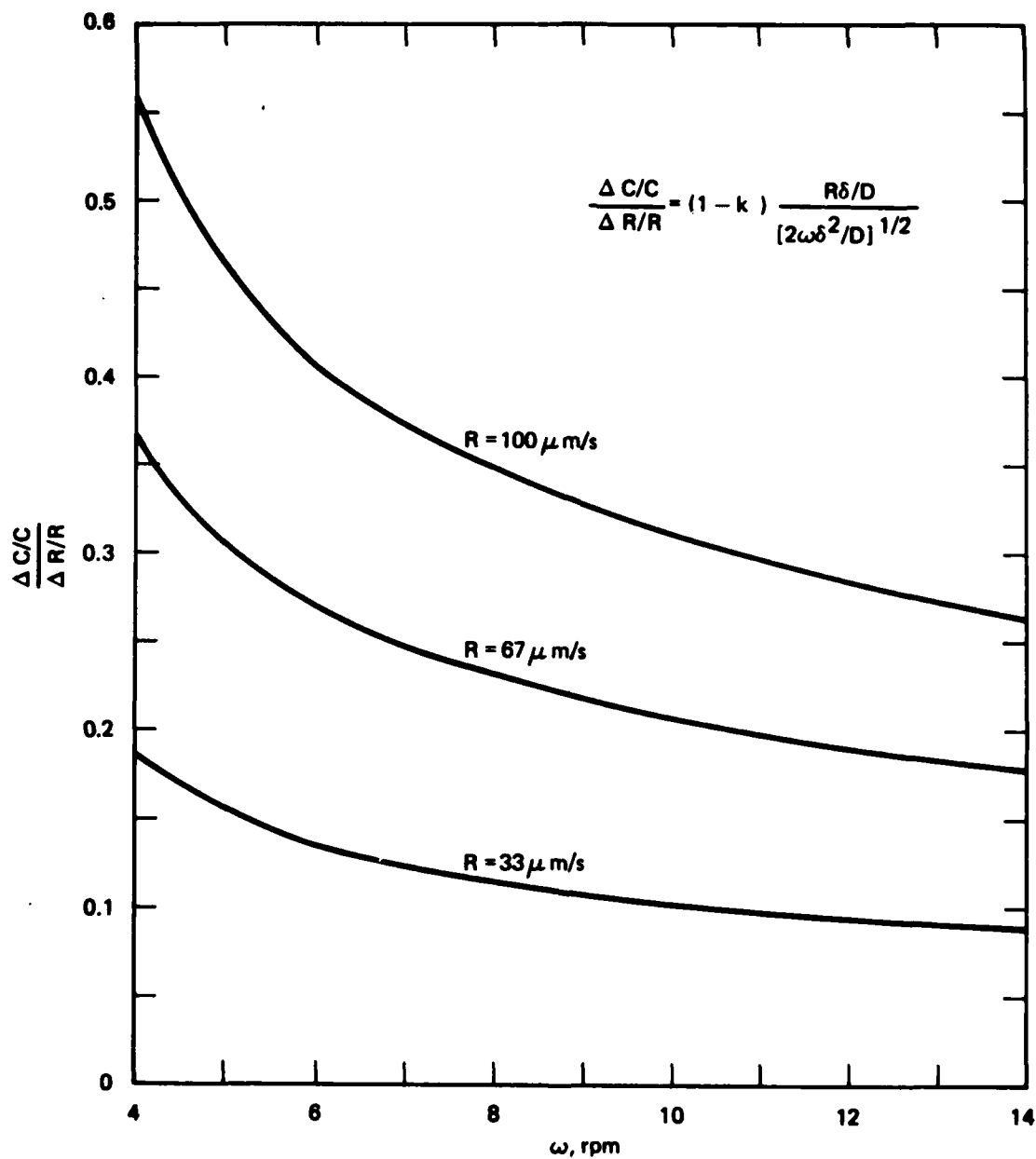
Figure 1. Theoretical dependence of compositional fluctuations
on microscopic growth rate (R) and rotation rate
(ω).

20

B.   GROWTH AND ROTATION RATE SURVEY

Crystal Z108Ga was grown to study the effect of growth rate and rotation rate on the segregation of Ga and the role these rates play in determining the shape of the solid-liquid interface. The following combinations of growth rate and rotation rate were used.

Section	1	2	3	4	5
Growth rate, mm/min	4	4	4	2	3
Rotation rate, rpm	6	8	3	3	3

Figure 2 shows the crystal after etching with a striation etch to reveal the shape of the interface. The crystal was cut where the parameters were changed, and evaluation wafers were sliced from the other half of the sectioned crystal. The first combination, a growth rate of 4 mm/min and a rotation rate of 6 rpm, was what we normally used to grow Ga-doped crystals. Striations start to appear where Ga was initially embedded in the polycrystalline Si charge. The shape of the striation shows that the interface is convex toward the growing crystal at this setting.

In the next section, where the rotation rate was increased to 8 rpm while the growth rate was kept at 4 mm/min, the core of the crystal moves further into the melt, forming a flatter interface. The distance between striations decreases because of the increased rotation rate.

The third section was grown by decreasing the rotation rate to 3 rpm while keeping the growth rate constant at 4 mm/min. As the rotation decreased, the downward velocity component of the convection flow increased to raise the temperature at the center of the crystal. The result is a very pronounced convex profile toward the crystal.

In the last two sections, the growth rate was decreased to 2 mm/min and 3 mm/min. The resulting flattening of the interface appeared clearly although not enough time was allowed to reach a steady state.

Spreading resistance measurements were made on these sections in the radial direction. Figure 3 shows the microscopic fluctuation in

SECTION NO.	1	2	3	4	5
GROWTH RATE, mm/min:	4	4	4	2	3
ROTATION RATE, rpm:	6	8	3	3	3

M12797

Figure 2. The cross section of crystal Z108Ga etched to reveal the striations in Ga concentration.
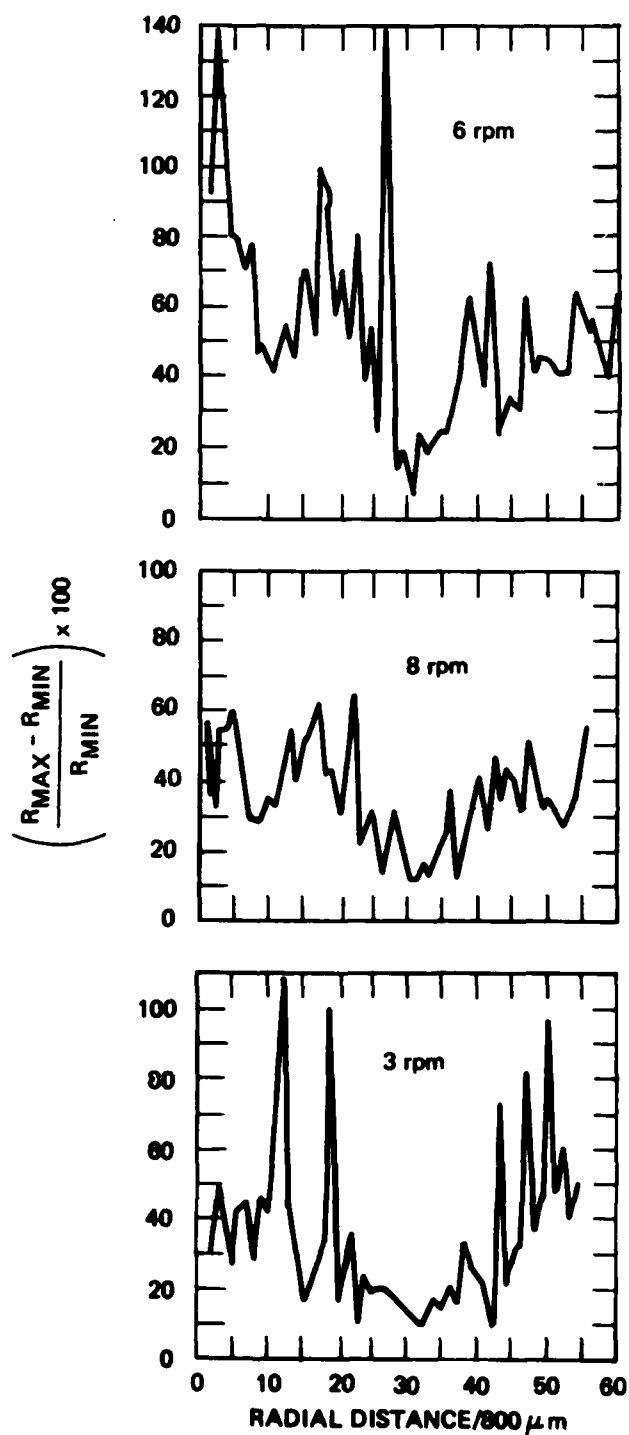
Figure 3.
Localized microscopic resistivity fluc-
tuations in Z108Ga for a growth rate
of 4 mm/hr at three rotation rates
(sections 1, 2, and 3).

23

resistance for the three sections grown at 4 mm/min. The maximum
resistance minus the minimum resistance divided by the minimum resis-
tance times 100 in each 800-μm interval along the radial direction is
plotted on the ordinate and the radial distance is plotted on the
abscissa in normalized increments of 800 μm width. The traverse in this
and following figures is made across a diameter of the wafer.

Comparing the three sections in Figure 3, the uniformity of Ga dis-
tribution is clearly worst for the case where the crystal was grown with
a 6 rpm rotation ("normal" condition). Comparing the two cases where
the crystal was rotated at 8 rpm and 3 rpm, the faster rotation appears
to be better. The measurements do indicate, however, that the result is
not in agreement with the predictions from the segregation theory or
with the shape of the interface, as discussed later. Ambiguity may
arise from the two-point-probe spreading resistance measurement, which
gives the total value of the two spots separated by the probe separation
of 400 μm. Single probe measurements were made and the results are
discussed in Section 3.

Figure 4 shows the uniformity in the last two sections of the crys-
tal where the rotation rate was kept constant at 3 rpm, but the growth
rate was reduced to 2 mm/min and 3 mm/min. We were unable to make a
complete scan across the wafer because the crystal cracked (during cut-
ting) in the fourth section, where the growth rate was 2 mm/min. The
figure shows that the uniformity is considerably better for the 3 mm/min
growth rate. It appears, however, that the time allowed to reach a steady
state was not sufficient to yield a fair assessment of the effect of the
slowest growth rate. The uniformity of the last section, grown at
3 mm/min with 3 rpm rotation, appears comparable to that of section two,
which was grown at 4 mm/min and 8 rpm rotation. In Figure 5, the aver-
age values of the concentration of Ga in 800-μm intervals determined by
the spreading resistance measurements (Figures 5(a) and (b)) are plotted
together with the values obtained by the four-point probe measurements
(Figures 5(c) and (d)). This averaging over 800-μm intervals provides a

24
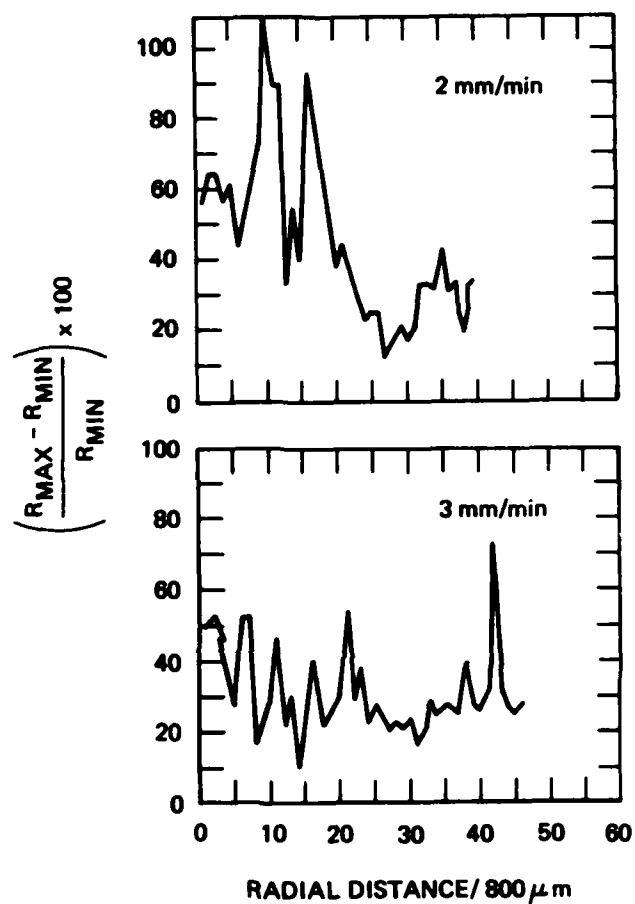
Figure 4.
Microscopic spreading resistance fluctuatio.s in
Z108Ga for a rotation rate of 3 rpm and
two relatively slow growth rates
(sections 4 and 5).
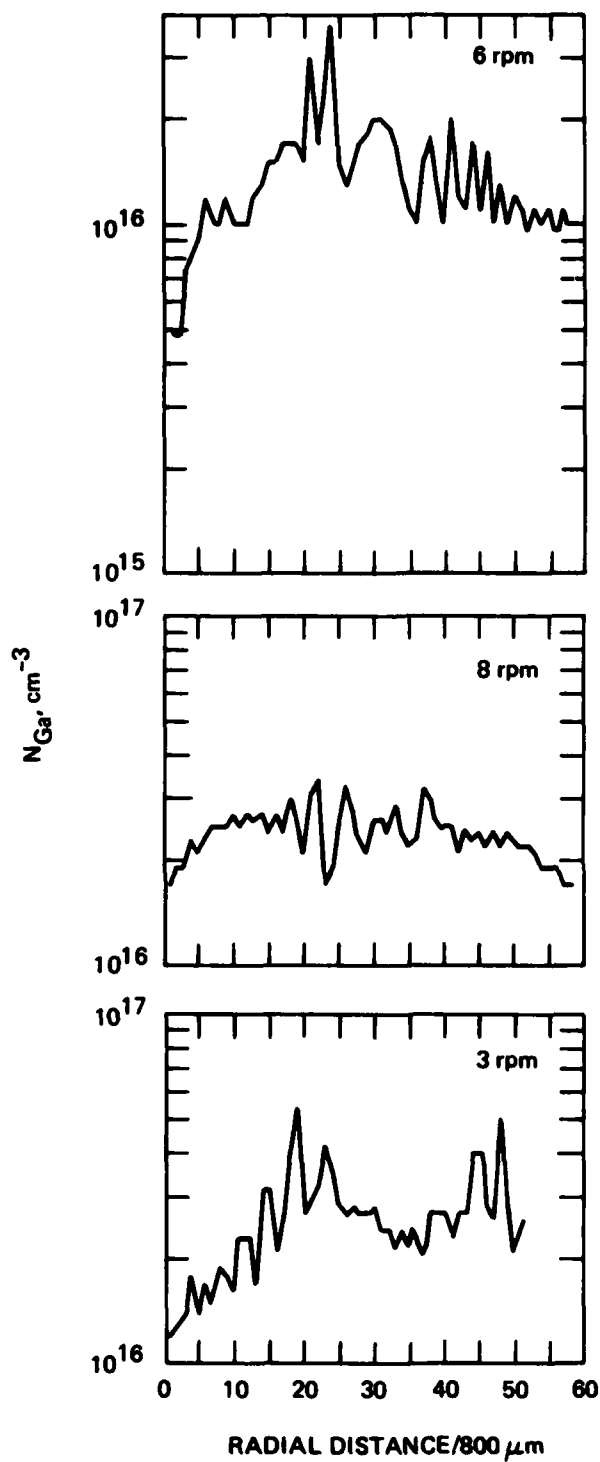
(a) Section 1, 2, and 3 by spread-
      ing resistance technique.

Figure 5.   Ga concentrations in Z108Ga
             in each of the 5 sections.

26
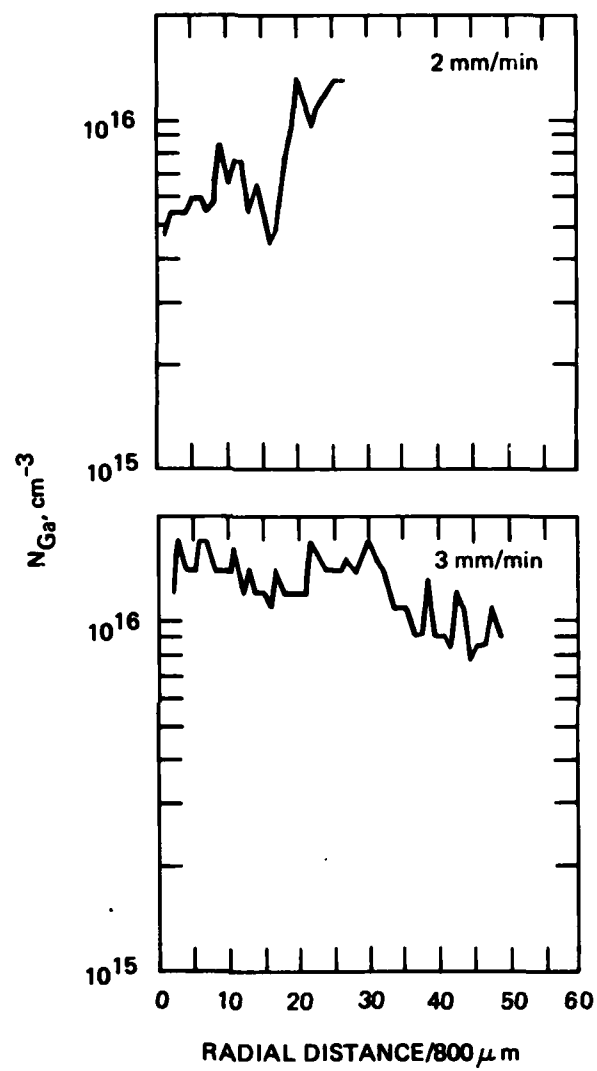
(b)　Sections 4 and 5 by spreading
　　 resistance technique.

Figure 5.　Continued.

27
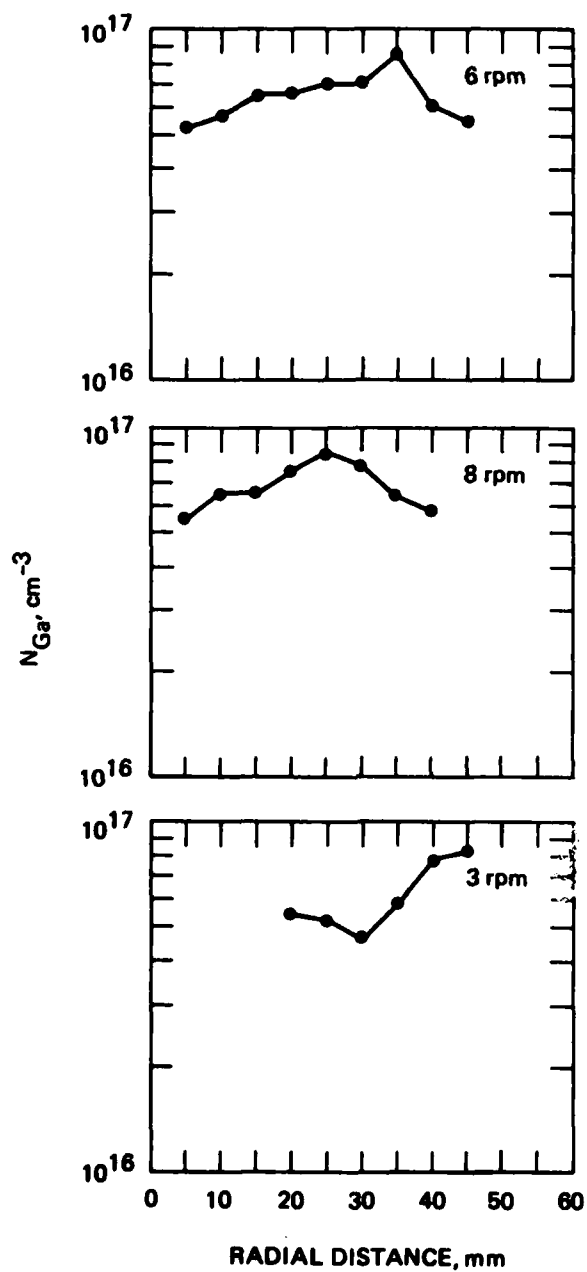
(c) Sections 1, 2, and 3 by four-
point probe method.

Figure 5. Continued.

28
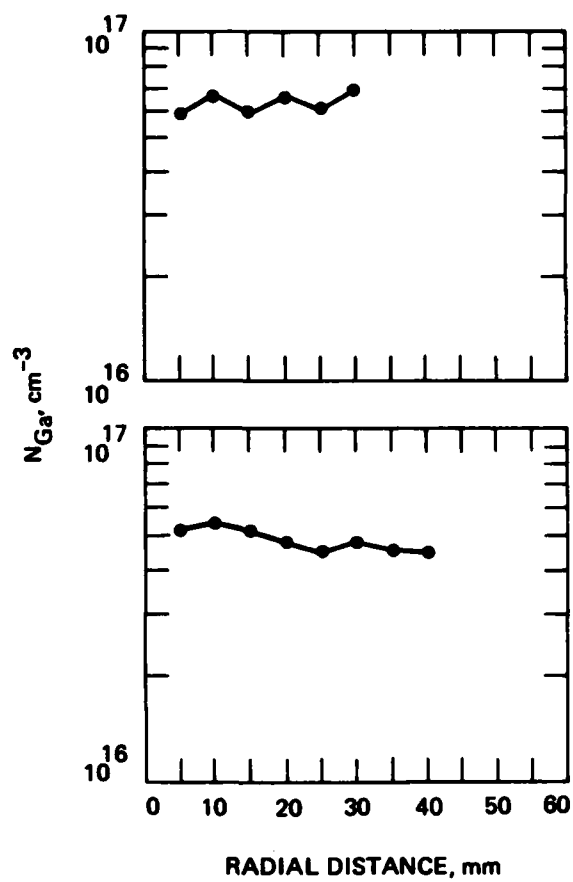
(d) Sections 4 and 5 by four-point probe method.

Figure 5. Continued.

scale intermediate between that of the direct spreading resistance measurements and that of the four-point probe. The absolute values of concentration do not agree with the four-point probe values because of our use of an uncorrected calibration curve to convert spreading resistance to concentration. Since our interest lay in assessing the fluctuations within a wafer, we did not recalibrate after each run.

The mean values, $\overline{X}$, and the associated standard deviations, σ, taken from Figures 3 and 4, are tabulated below.

Z108	Section				
	1	2	3	4	5
$\overline{X}$	53	36	34	46	31
σ	28	14	22	24	13
$\overline{X} = \dfrac{\overline{R_{max} - R_{min}}}{R_{min}} \times 100$					

The fluctuations in the average concentration are considerably less in the second and fifth sections, where the rotation rate was increased or the growth rate was decreased from the normal values used in section 1. As seen in Figures 5(a) and (b), the lower concentration of Ga near the periphery that usually occurs arises mainly from the thinner interfacial layer, which results from the higher tangential and radial velocities of convection flows. The mean concentrations from the spreading resistance measurements and the associated standard deviations are tabulated below.

Z108Ga	Section				
	1	2	3	4^a	5
$\overline{N}_{Ga} \times 10^{-16}$, cm^{-3}	1.4	2.4	2.6	0.79	1.3
$\sigma \times 10^{-16}$, cm^{-3}	0.58	0.39	0.88	0.30	0.25
[a] Only 1/2 wafer was available for analysis.					

30

Following the growth and preliminary evaluation of Z108Ga, we grew a series of crystals as part of our investigations of the various growth parameters controlling the microscopic fluctuations in Ga concentration. For the convenience of the reader, we have summarized these crystals in Table 1 in chronological order and listed the primary purpose for which they were grown. Detailed discussions of the significant results from these crystals constitute the bulk of this report.

Table 1. Crystals Grown for the LADIR Materials Program

Crystal Number	Purpose
Z108Ga	Initial survey of growth parameters
Z118Ga	Enhanced rotation rate studies
Z144B	Uniformity of boron distribution
Z145B	
Z095Ga	Cooling ring study
Z050Ga	Growth at 2 mm/min; crystal twinned
Z179Ga	Enhanced effective distribution coefficient
Z180Ga	Low growth and high rotation rates
Z196Ga	Growth at 2 mm/min; crystal twinned
Z203Ga	Verify Ga doping levels; crystal twinned
Z204Ga	For FPA wafers at 2.5 mm/min and 10 rpm
Z205Ga	For FPA wafers at 2.5 mm/min and 10 rpm
Z206Ga	For FPA wafers at 2.5 mm/min and 10 rpm; successful

C. ENHANCED ROTATION AT FIXED GROWTH RATE

The effect of rotation rate and growth rate as predicted by the segregation theory was further investigated. Crystal Z118Ga was grown at the maximum rotation rate and at the slowest growth rate possible for that rotation rate. The growth rate was kept constant at 4 mm/min while the rotation rate was increased from 8 rpm to 13 rpm.

Figure 6 is a photograph of this crystal after it had been cut longitudinally and striation etched. The transition to 13 rpm is clearly visible by the more closely spaced striations and the bulging at the core of the crystal.

Figure 7 shows the spreading resistance in the radial direction of the two sections in which 8 rpm and 13 rpm rotation rates were used. The correlation between the etched pattern and the spreading resistance scan is shown in Figure 8. Large amplitude fluctuations toward the edges of the wafer correlate with the two probes intersecting the rotational striations. At the core of the wafer, where the interface is flat and almost perpendicular to the growth axis, the spreading resistance profile shows fewer fluctuations.

Figure 9 shows the microscopic fluctuations in the 800-μm segments along the radial direction. Noticeable improvement is seen in the central core region in the part of the crystal rotated at 13 rpm. Although the mean value of the fluctuations across the diameter is the same, the 13 rpm part appears to have a smaller standard deviation in the central region, as can be seen in Figure 7. The following tabulation shows the values averaged across the entire diameter.

M12843

13 rpm   8 rpm
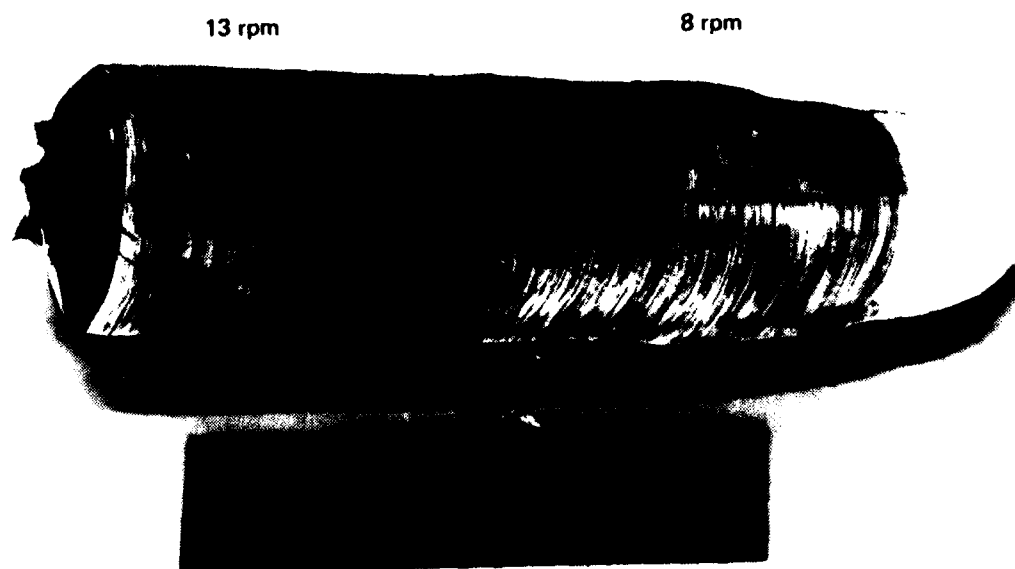
Figure 6. Cross section of Z118Ga etched to show Ga concen-
           tration striations at two rotation rates. Growth
           rate was 4 mm/min.
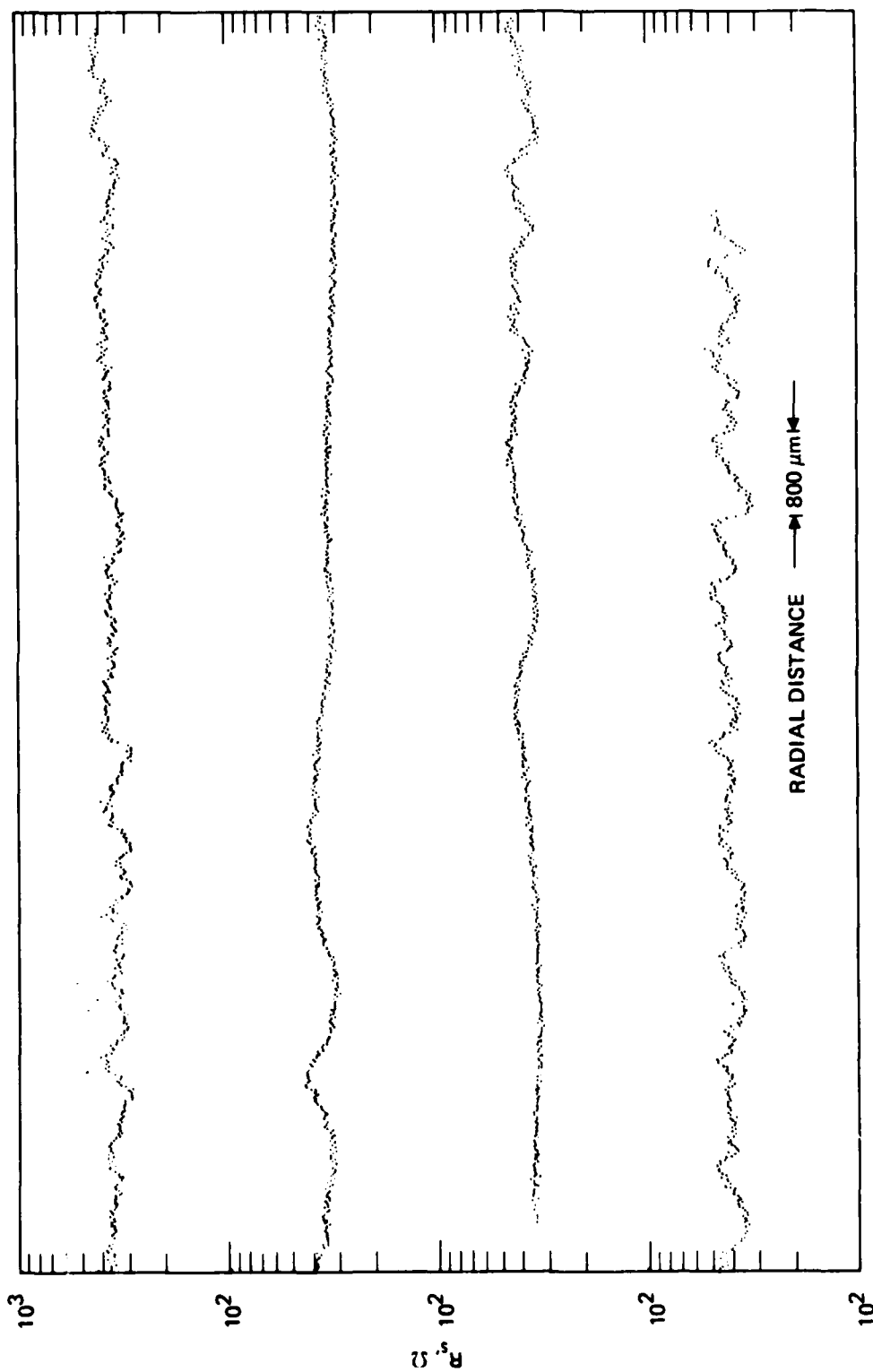
(a) 8 rpm section

Figure 7(a). Spreading resistance profile in the radial direction from Z118GA, 8 rpm section. The travers begins in the upper left at one edge of the wafer and proceeds sequentially across the diameter in each successively lower trace, ending at the bottom right which corresponds to the other edge of the wafer.

RADIAL DISTANCE ⟶ ◄800 μm►

R_s, Ω

10^3 10^2 10^2 10^2 10^2
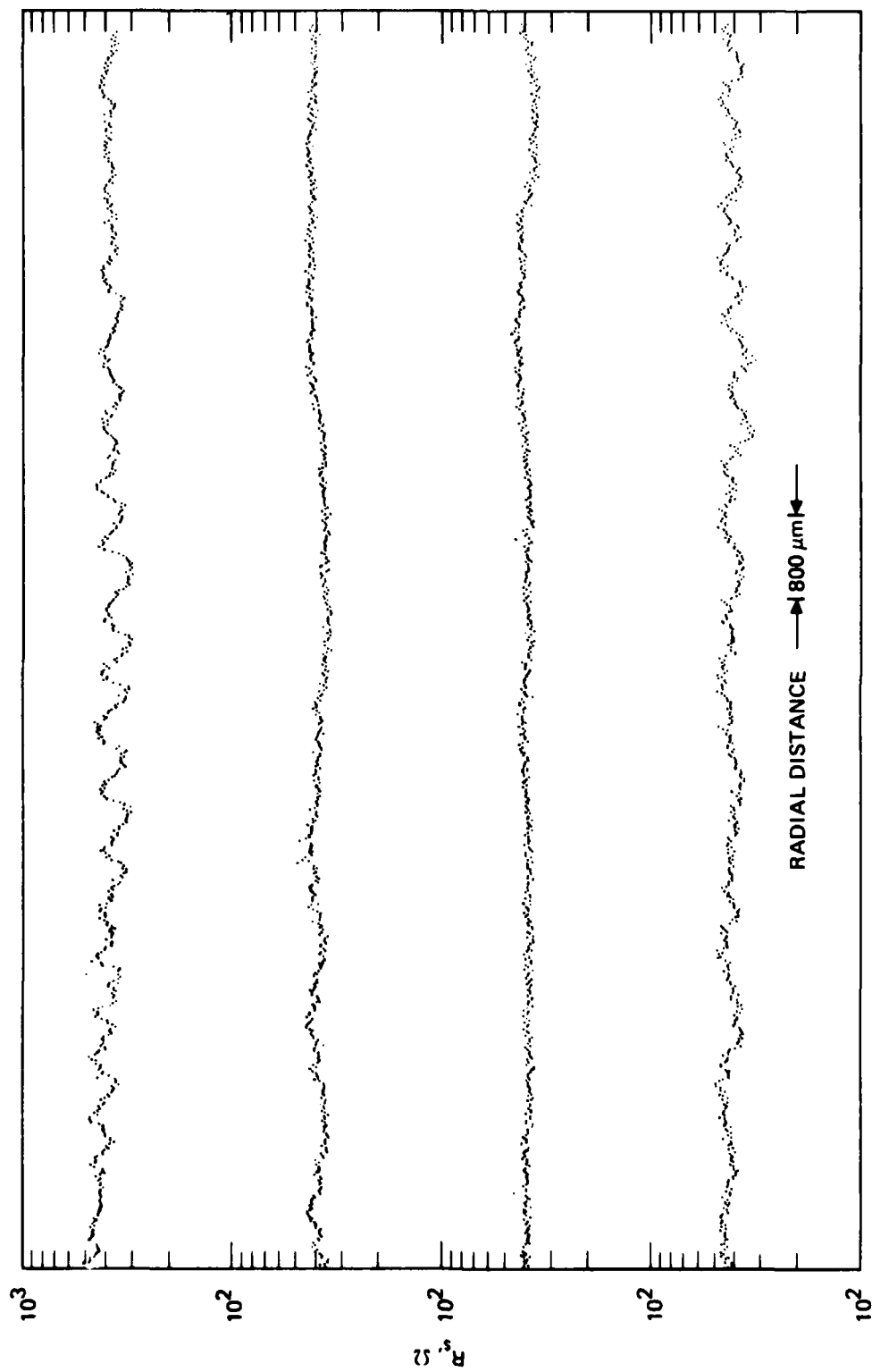
(b) 13 rpm section

Figure 7(b). Spreading resistance profile in the radial direction
for Z118Ga , 13 rpm section.

RADIAL DISTANCE, 800 μm

ETCH PATTERN, (R_S), Ω

10^3

10^3

10^3
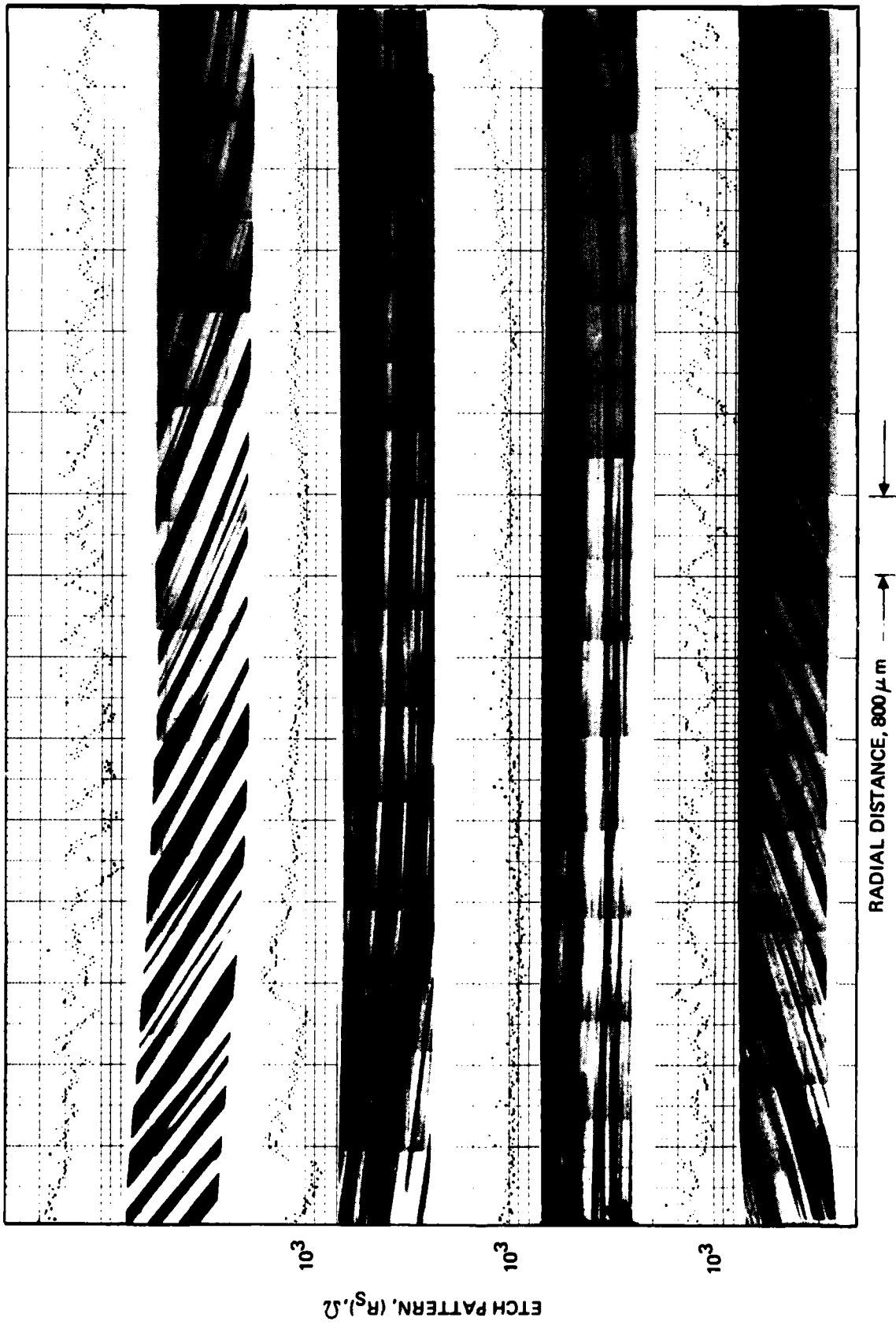
Figure 8. Spatial correlation of etched striation pattern and microscopic spreading resistance fluctuations for Z118Ga.

36
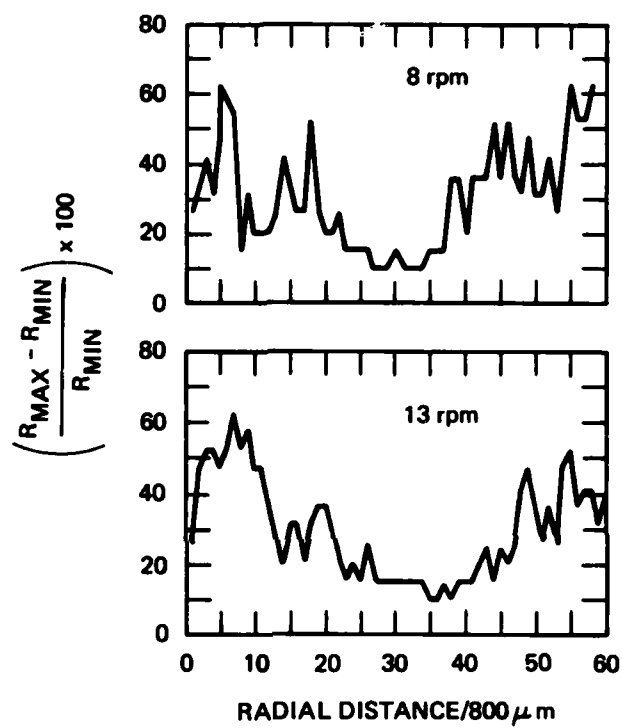
Figure 9. Microscopic spreading resistance fluctuations for Z118Ga at two rotation rates.

Z118Ga	8 rpm	13 rpm
$\overline{X}$	30	30
σ	16	15

The average concentrations in each 800-μm segment along the radial direction are plotted in Figure 10. The uniformity is about the same in the two sections. The mean concentration values and the standard deviations are tabulated below.

Rotation Rate	8	13
$\overline{N}_{Ga} \times 10^{-16}$, cm^{-3}	4.6	4.7
$\sigma \times 10^{-16}$, cm^{-3}	0.51	0.55

Figure 11 shows the concentration variation measured by the four-point probe method; it is in good agreement with the data in Figure 10.

D. ENHANCED ROTATION AT SLOW GROWTH RATES

We achieved a marked improvement in uniformity by reducing the growth rate to 4 mm/min and increasing the rotation rate to 8 and 13 rpm in crystal Z118Ga. The final experimental crystal, Z180Ga, was grown to examine whether further improvement could be attained by trying the extreme conditions — the slowest growth rate and the fastest rotation rate used to grow a dislocation-free crystal. As with earlier experimental crystals growth was started at a high growth rate and a low rotation rate, and then progressively the growth rate was lowered and the rotation rate increased.

The following growth conditions were employed in Z180Ga.
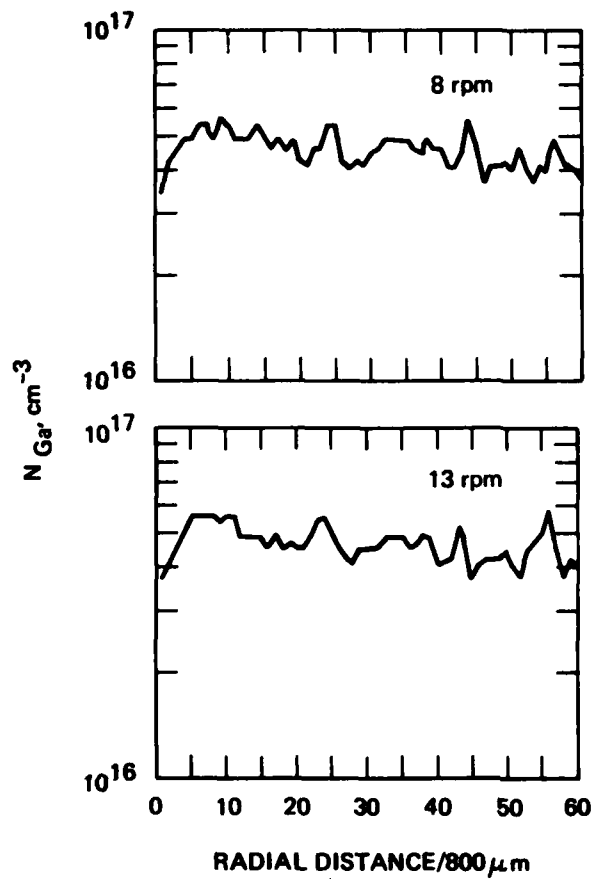
Figure 10.
Radial distribution of Ga in
Z118Ga for two rotation
rates.

Figure 11.
Radial distribution
of Ga in Z118Ga as deter-
mined by four-point probe
resistivity measurements.

39
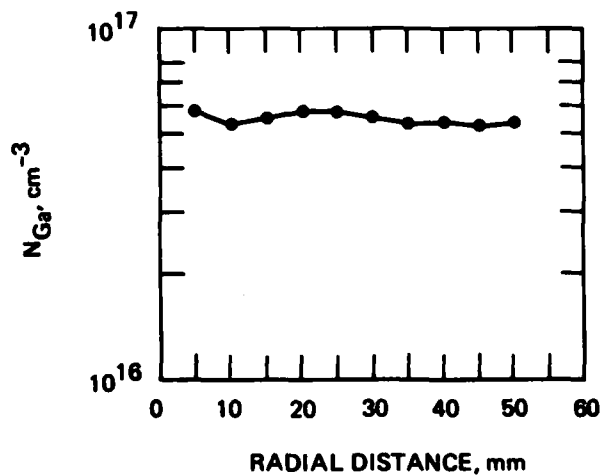
Z108Ga	Section						
	1	2	3	4	5	6	7
Growth Rate, mm/min	3.2	3	3	3	3	2.5	2
Rotation Rate, rpm	4	4	6	8	10	10	10

In the last section, the crystal twinned out when the growth rate was reduced to 2 mm/min at 10 rpm. We typically experience difficulty in maintaining crystal perfection at growth rates of 2.5 mm/min or less.

After growth, this crystal was sliced along the growth axis and spreading resistance measurements were carried out on all sections except on the last, where the crystal twinned. The spreading resistance measurements were made using both a double-probe and a single-probe method, which required ion implanting on the back side to form a low resistance Ohmic contract.

The microscopic variations were measured as previously in 800-μm segments and plotted in Figure 12. The averages of the percentage variations and standard deviations for the single- and double-probe spreading resistance measurements are tabulated below.

Growth Rate, mm/min.	3.2	3	3	3	2.5
Rotation Rate, rpm	4	4	6	10	10
$\overline{X}$ (single)	27	29	21	29	16
σ (single)	14	17	11	12	9
$\overline{X}$ (double)	22	20	28	24	22
σ (double)	9	13	14	9	12

No definite trends are associated with the increase in the rotation rate from 4 to 10 rpm or the reduction in growth rate from 3.2 to 2.5 mm/min, although the average microscopic fluctuations are reduced
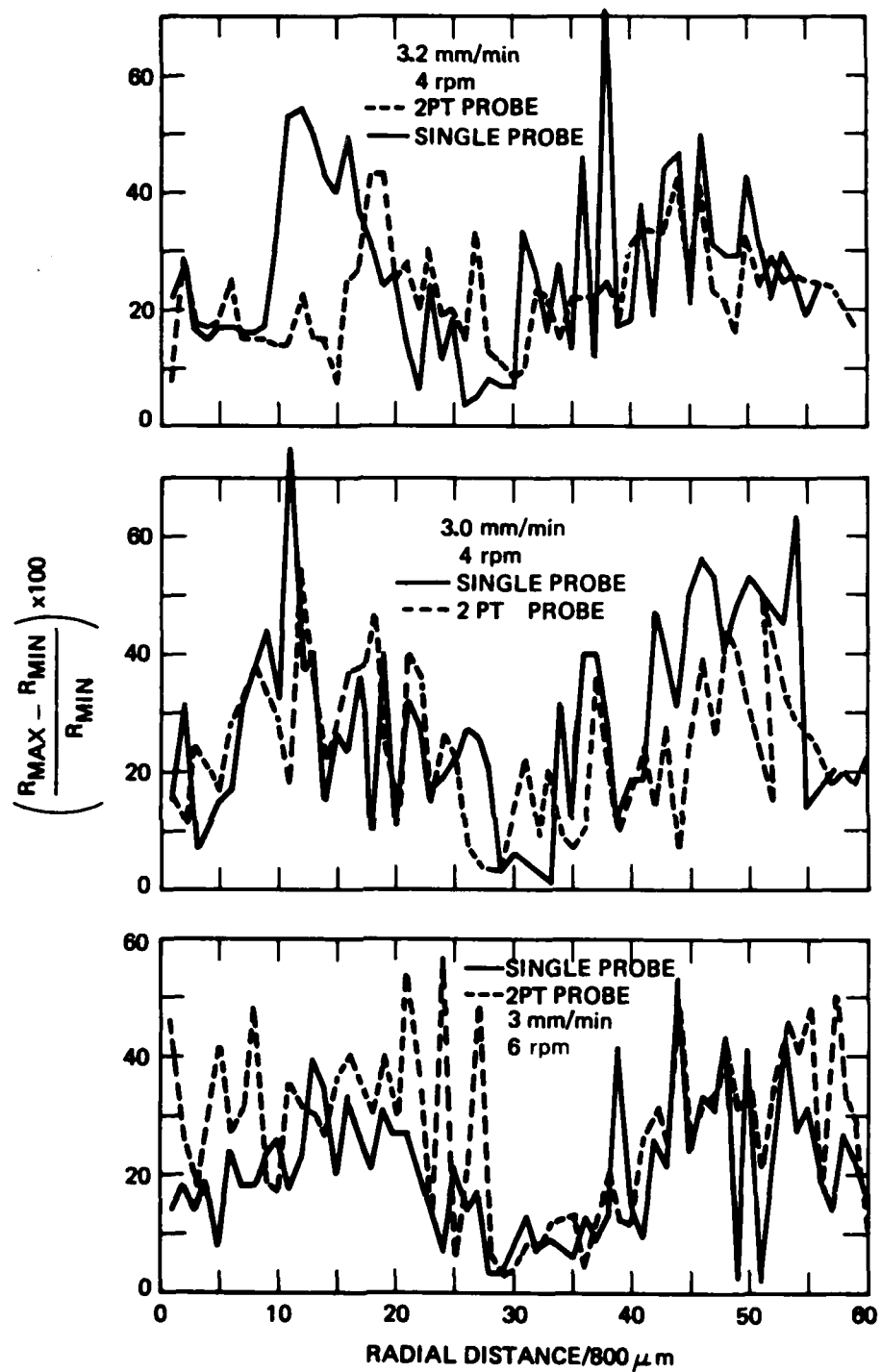
(a) Sections 1, 2, 3, single- and double-probe
    measurements.

Figure 12. Microscopic spreading resistance fluctuations
            in Z180Ga.

41
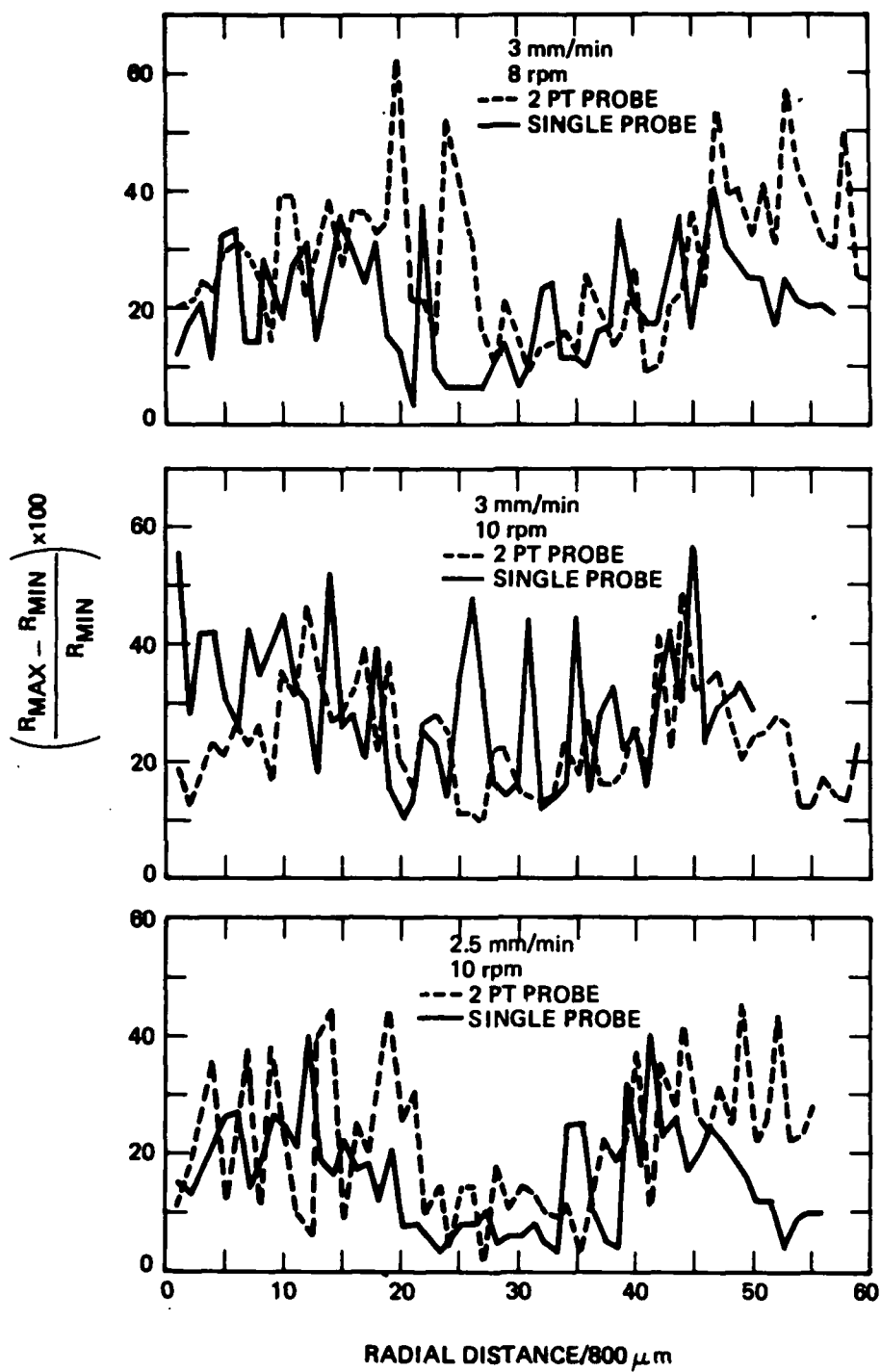
(b) Sections 4, 5, 6, single- and double-probe
measurements.

Figure 12. (Continued).

42

considerably from the segments of crystal Z108Ga where higher growth rates were employed. This will be analyzed in more detail in Section 3.

E.   ENHANCED EFFECTIVE DISTRIBUTION COEFFICIENT

As another approach to smoothing out dopant striations, we have explored the possibility of growing under conditions in which the effective distribution coefficient k_e is maximized. According to the analysis by Burton, Prim, and Slichter,[1] k_e is expressed as

$$k_e = \frac{k}{k + (1-k)\exp(-R\delta/D)} , \qquad (4)$$

where k is the equilibrium distribution coefficient, R is the microscopic growth rate, δ is the interfacial diffusion boundary layer thickness, and D is the diffusion coefficient of dopant in the liquid. Figure 13 shows the plot of k_e/k versus the rotation rate ω at microscopic growth rates of 33, 67, and 100 μm/sec calculated from the equation using 0.008 as the equilibrium distribution coefficient of Ga.

The effective distribution coefficient can be substantially increased to approach unity if:

●   Backmelting of the newly grown layer on each rotational cycle is eliminated by growing the crystal at a fast rate

●   The microscopic growth rate is increased by growing the crystal at a fast rate assuming that the microscopic growth rate varies sinusoidally about the average microscopic growth rate, which is the same as the pull rate

●   The interfacial boundary layer thickness δ is increased according to Cochran's analysis by decreasing the rotation rate.

On the basis of the above analysis, crystal Z179Ga was grown at the maximum growth rate of 6 mm/min, and the rotation rate was reduced during growth from 8 to 4 to 2 rpm. This crystal thus represents the opposite extreme from Z180Ga, in which growth rate was minimized and

43
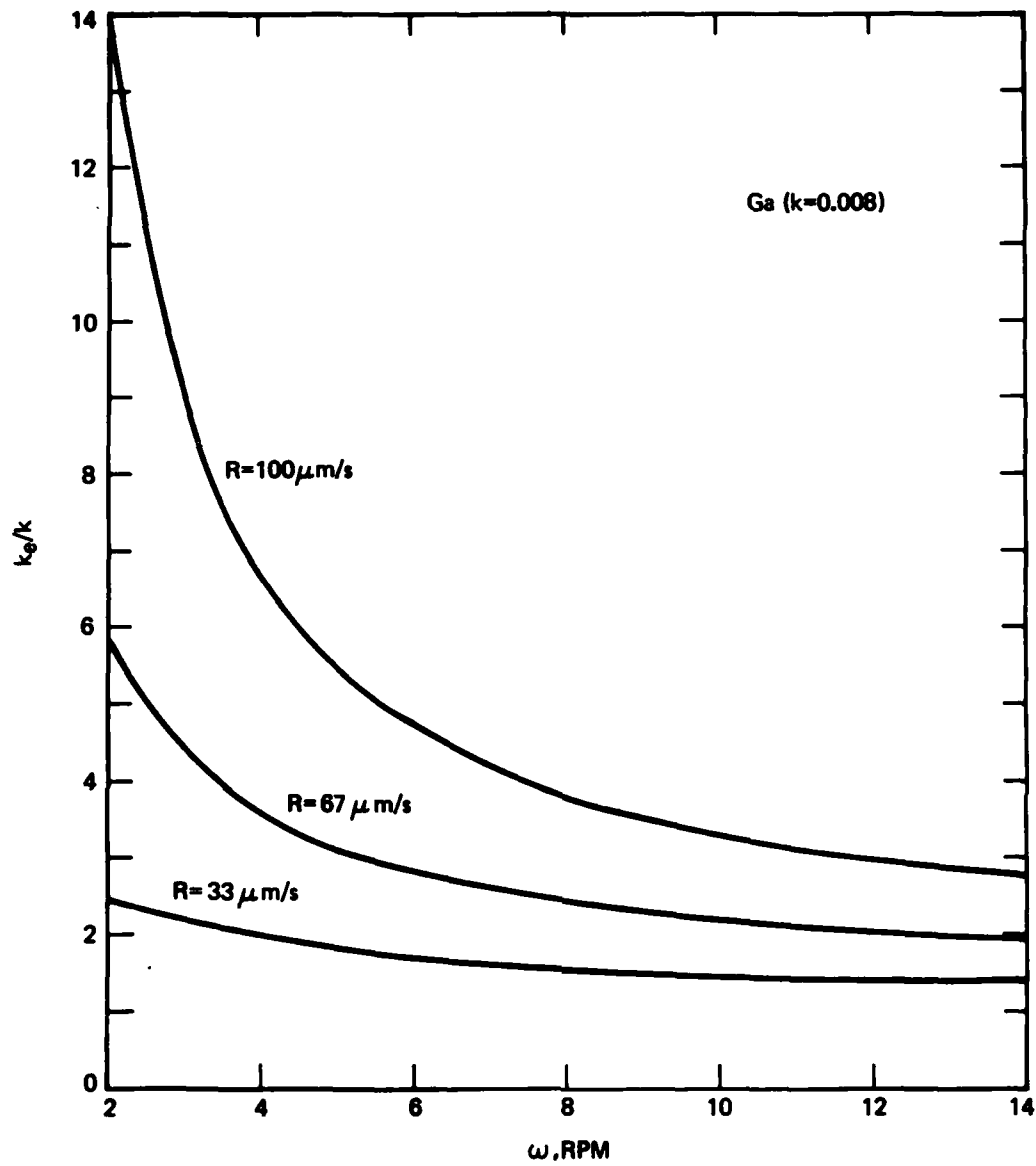
Figure 13. Change in effective distribution coefficient
of Ga with rotation rate and growth rate.

44

rotation rate maximized. Figure 14 shows the microscopic variations versus radial distance. The average variations and standard deviations are tabulated below.

rpm	8	4	2
$\overline{X}$	45	54	37
σ	19	23	12

The analysis shows that a substantial improvement can be achieved by lowering the rotation rate. Further experiments are needed to explain the sudden increase in the average microscopic fluctuation at 4 rpm, which is not clearly understood.

Experiments in this direction, that is to optimize uniformity via increased effective distribution coefficient, were not pursued further because of the generally higher microscopic variations. The reason for this unfavored dopant distribution may partly be the severe concavity of the interface toward the melt when the combination of a fast growth rate and a slow crystal rotation rate is employed.

F. EFFECT OF COOLING RING

Since the shape of the freezing interface and therefore the radial uniformity are governed by the heat balance at the interface, crystal ZO95Ga was grown with a cooling ring. The cooling ring was placed ~1 in. below the crystal-to-melt interface and was cooled with Ar gas. The growth parameters used are given below.

Distance from Seed, cm	Growth Rate, mm/min	Crystal Rotation Rate, rpm
0 to 8	4.2	8.0
8 to 12	4.2	3.3
12 to 19	3.0	3.3
19 to 21	2.5	3.5
21 to 24	2.5	8.0
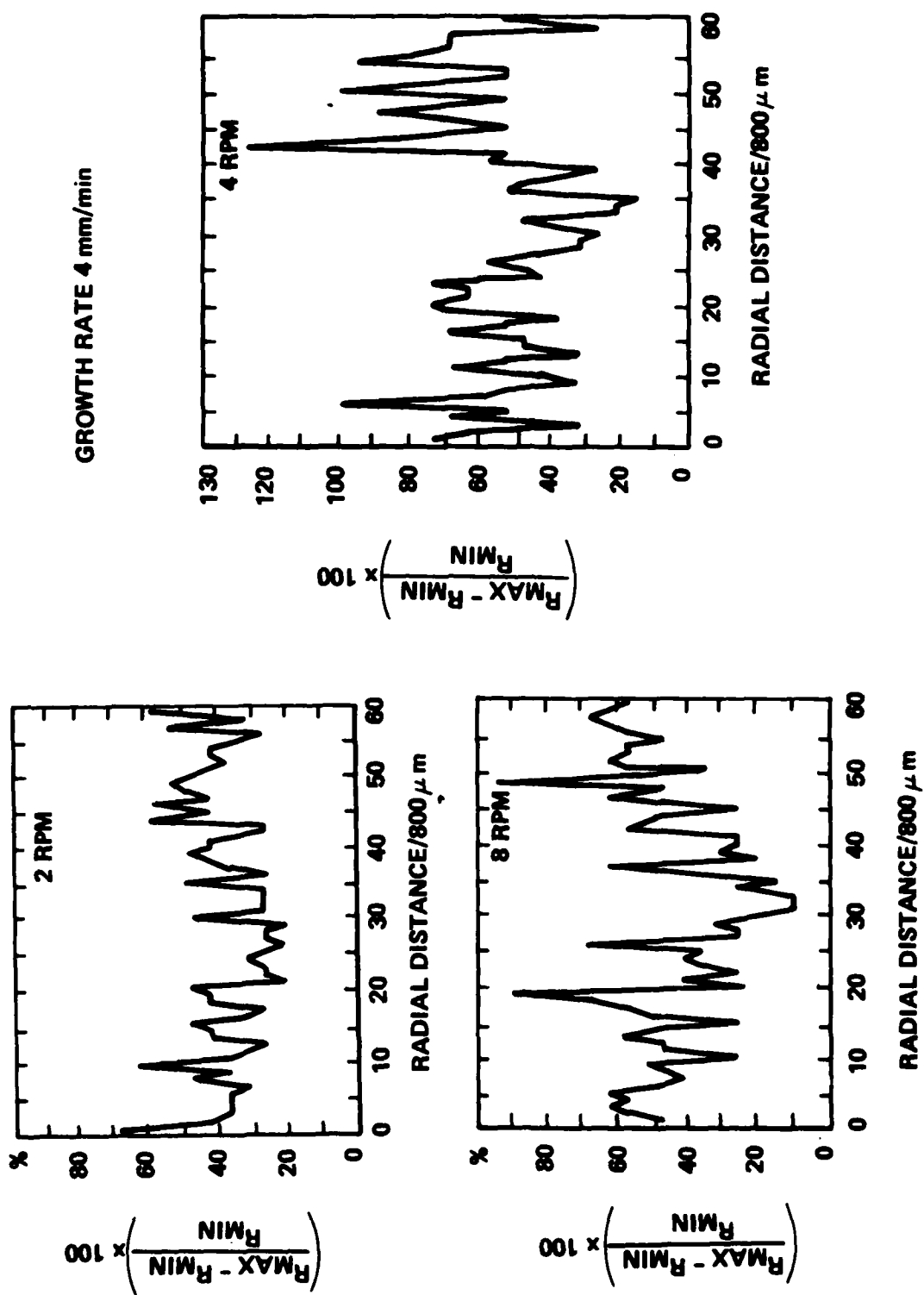
Figure 14. Microscopic spreading resistance fluctuations with enhanced effective distribution coefficient in Z179Ga.

46

The spreading resistance profiles and the shapes of the interface show the effect of growth and rotation rates, as previously reported, but there was no noticeable improvement due to the cooling ring. No further studies were made on this crystal, and we did not conduct any more experiments with a cooling ring.

G. UNIFORMITY OF BORON DISTRIBUTION

A B-doped crystal, Z144B, was grown to assess the uniformity of residual B distribution. Since a wafer can be uniformly counter doped with P by neutron transmutation, the uniformity of B distribution is important in achieving a low and uniform value of $N_p - N_B$. A Czochralski-grown crystal doped with 10^{15} cm^{-3} B was used as a starting charge. The crystal was then grown in the float zone furnace at 4 mm/min and rotated at 6 rpm.

Figure 15 shows the plot of spreading resistance versus radial distance, and Figure 16 shows the plot of the microscopic fluctuations for Z144B. As expected from the near unity distribution coefficient of B ($k = 0.8$), the uniformity is excellent. The mean value was 17, and the standard deviation of the percentage fluctuations in the 800-μm segments was 5.2. The background noise of the instrument corresponds to $\sim$10% fluctuation. The nonuniformity of the B distribution in parts of the wafer, therefore, can be much less than 10%.

Figure 17 shows the concentrations of B along the radial distance as determined by the four-point-probe measurements. The uniform concentration seen here confirms the results from spreading resistance evaluation.

H. THERMAL DIFFUSION

1. Theory

In their studies of growth striations due to inhomogeneous doping of impurities in dislocation-free float-zoned and Czochralski Si

47
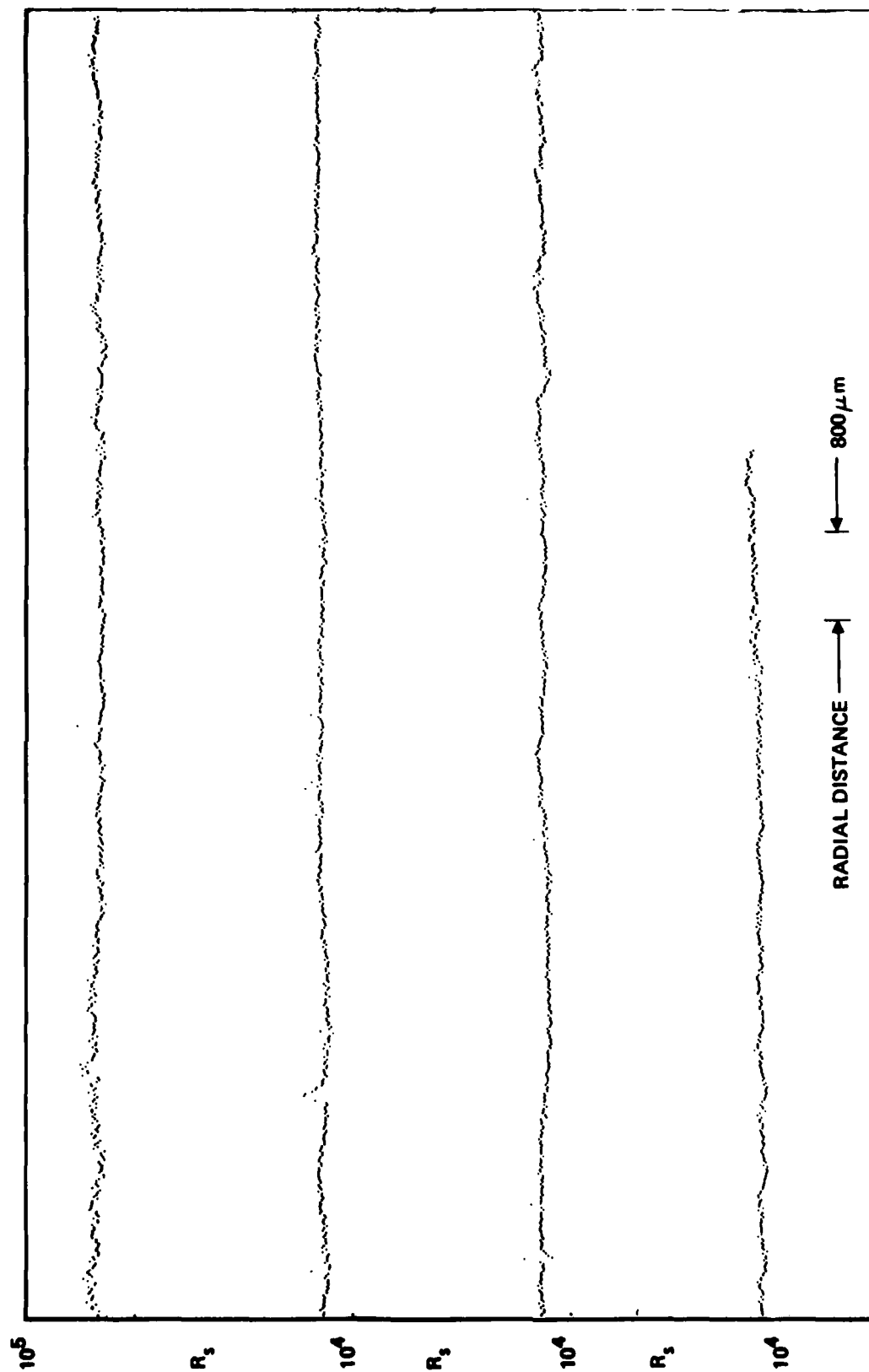
Figure 15. Radial distribution of spreading resistance in a B-doped crystal (Z144B).
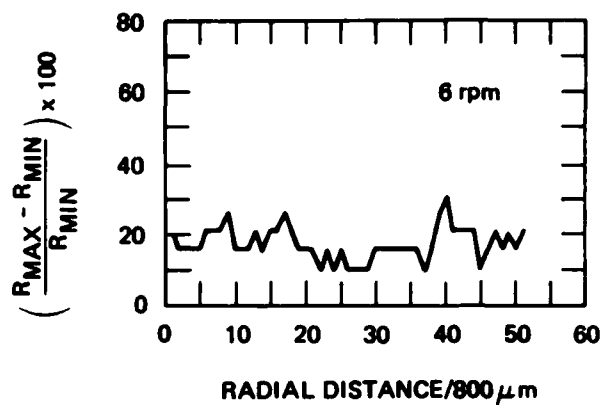
Figure 16.
Localized microscopic
spreading resistance
fluctuations in Z144B.

Figure 17.
Radial distribution of B in
Z144B as determined by
four-point probe resistivity
measurements.

49
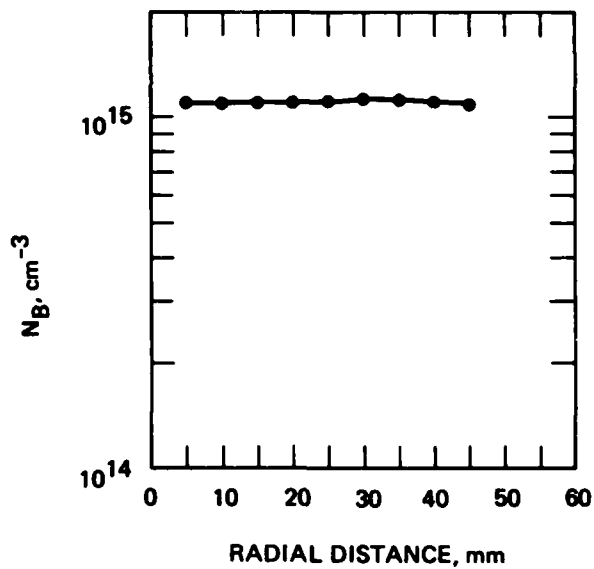
crystals, de Kock et al.[7] determined growth parameters that influence the formation of striations. They arrived at an in-situ annealing method that substantially reduced the amplitudes of striations. They showed that, if a crystal is grown at a very slow rate (e.g., 0.5 mm/min at 100 rpm), the distance between rotation striations will be so small (λ = 5 μm) as to almost completely eliminate striations due to phosphorus.

In silicon, Ga has a fairly low diffusion coefficient, D = 2.4 $\times$ 10^{-11} cm^2/sec at 1300°C. Hence, float-zoned Ga-doped crystals must be annealed at high temperatures if homogeneity is to be attained in a reasonable time. A periodic variation of dopant where k $\neq$ 1 along the growth axis x can be expressed as[7]

$$C(x) = C_o + C_1 \sin\left(\frac{2\pi}{\lambda}\right). \tag{5}$$

where C_o is the average concentration, C_1 is the amplitude of the rotational striation, and λ is the spacing between striations. During annealing, the amplitude C_1 decreases because of the diffusion of Ga. Solving the diffusion equation yields

$$C(x,t) = C_o + C_1 \left\{ \exp\left[- \left(\frac{2\pi}{\lambda}\right)^2 D(T)t \right] \right\} \sin\left(\frac{2\pi}{\lambda} x\right), \tag{6}$$

where D(T) is the diffusion coefficient at the anneal temperature T, and t is the time of anneal. The amplitude C_1 will decay exponentially with time as shown in Figure 18. As the amplitude of the striations decreases, the concentration gradient will also decrease to become less abrupt around the striations.

---

[7]A.J.R. DeKock, P.J. Roksnoer, and P.G.T. Boonen, J. Crystal Growth 28, 125-137 (1975).
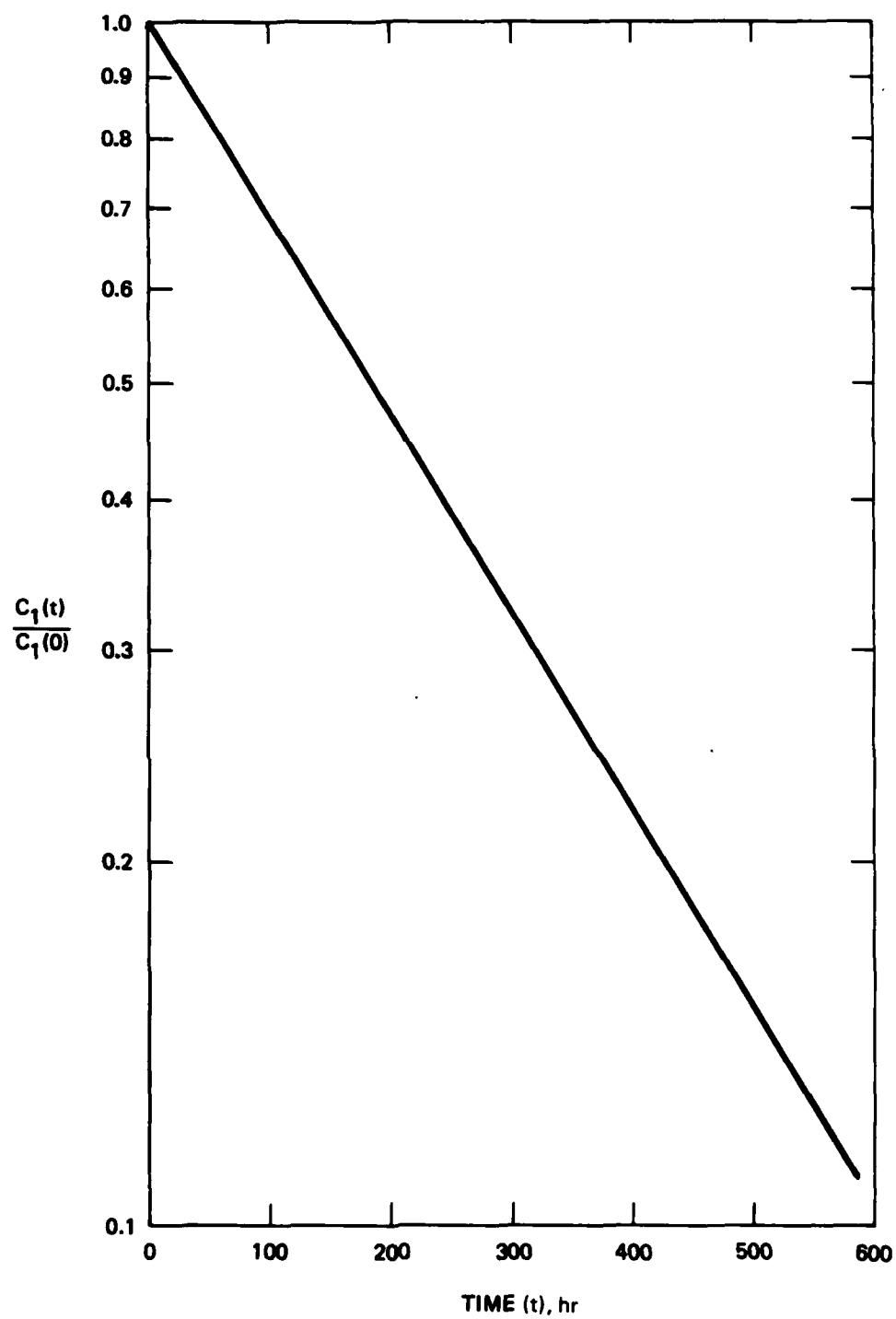
Figure 18.   Calculated decay rate of rotational striations.

2. Experimental Results

The diffusion was performed on a slab cut from a part of crystal Z118Ga that had been grown at 4 mm/min and 13 rpm. The slab was half circular in shape, 12 mm thick, and weighed 29 g. A spreading resistance measurement was made in a single-probe mode on a slice cut adjacent to the slab, as shown in Figure 19. The spacings between rotational striations are slightly more than the actual spacings because the scan was made across the diameter and the interface had a slight curvature. The calculated spacing between striations is 308 μm when the crystal is grown at 4 mm/min and 13 rpm. The amplitude varies from 8 to 11 mm near the edge of the crystal on the plot of log R_s versus radial distance. The decay of amplitude with time shown in Figure 18 was calculated using a nominal value of λ = 300 μm.

The annealing was carried out in a model B-8212 Futek furnace, which is capable of operating at 1800°C in air with lanthanum chromite heating elements. The maximum flat temperature zone at 1300°C is about 6 in. long. The sample was placed in a quartz ampoule and back filled with Ar so that the pressure was 1 atm at 1300°C. The first anneal experiment lasted for 187 hr. After the anneal, the sample was slowly taken out from the furnace and allowed to cool quickly to ambient temperature. Figure 20 shows the spreading resistance profile after the 187-hr anneal. The amplitudes are reduced to 4 to 7 mm from 8 to 11 mm before anneal, which is a reduction of 36 to 50%. From Figure 18, the reduction should be ∿50%, which is in fairly good agreement with the experiment.

The same sample was placed back into the furnace at 1300°C for an additional 181-hr anneal (a total anneal time of 368 hr). Figure 21 shows the spreading resistance profile. The maximum amplitude is 4 mm, which is a 64% reduction, slightly lower than the calculated 75%. The spacing λ increases as the microscopic fluctuations smooth out. The residual undulation is due to macroscopic variations, which take a considerably longer time to diffuse out. Figure 22 shows the annealed wafer after striation etching to reveal the diffused striations.
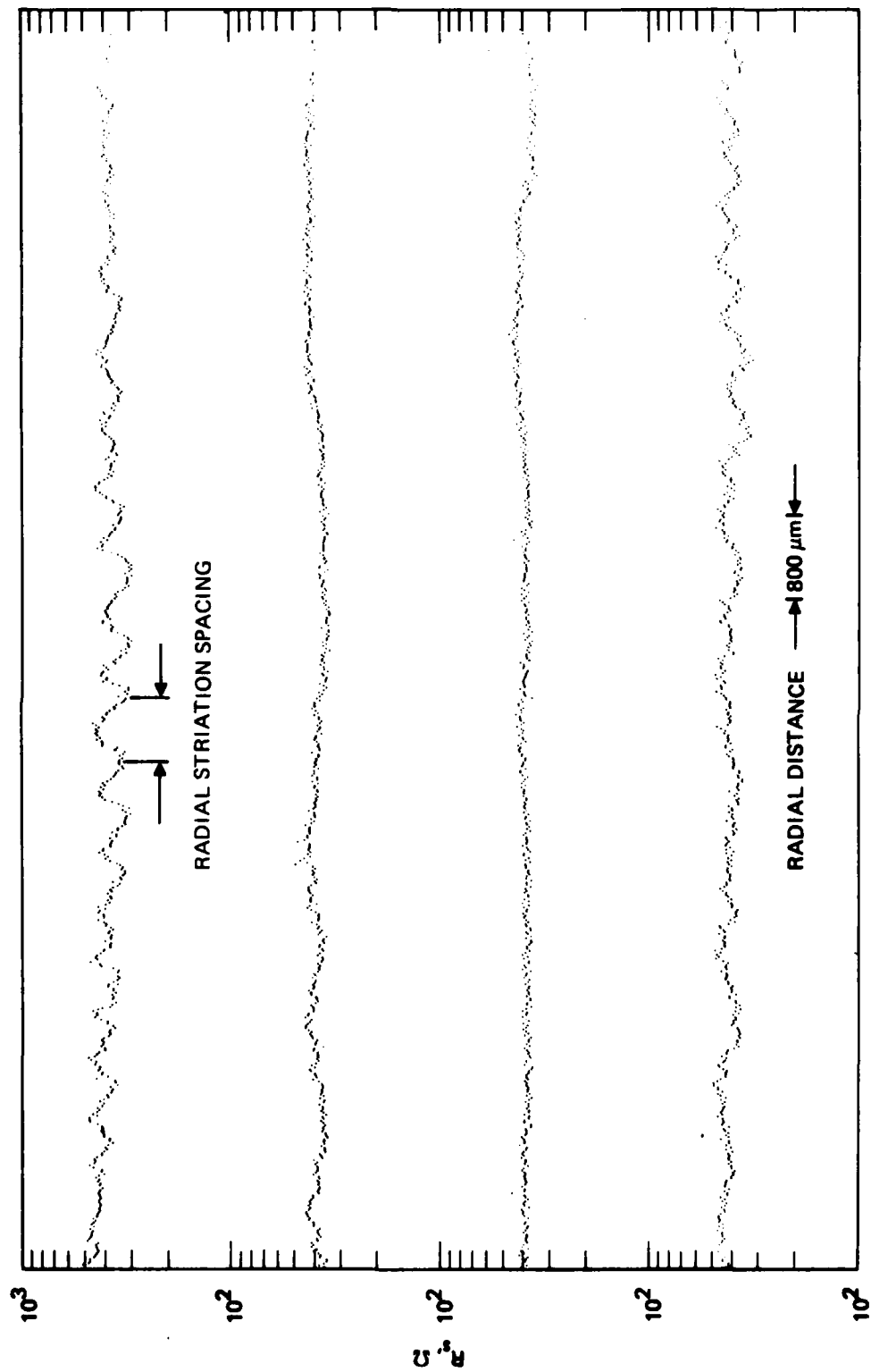
Figure 19. Rotational striation spacing as revealed by spreading resistance fluctuations.

53
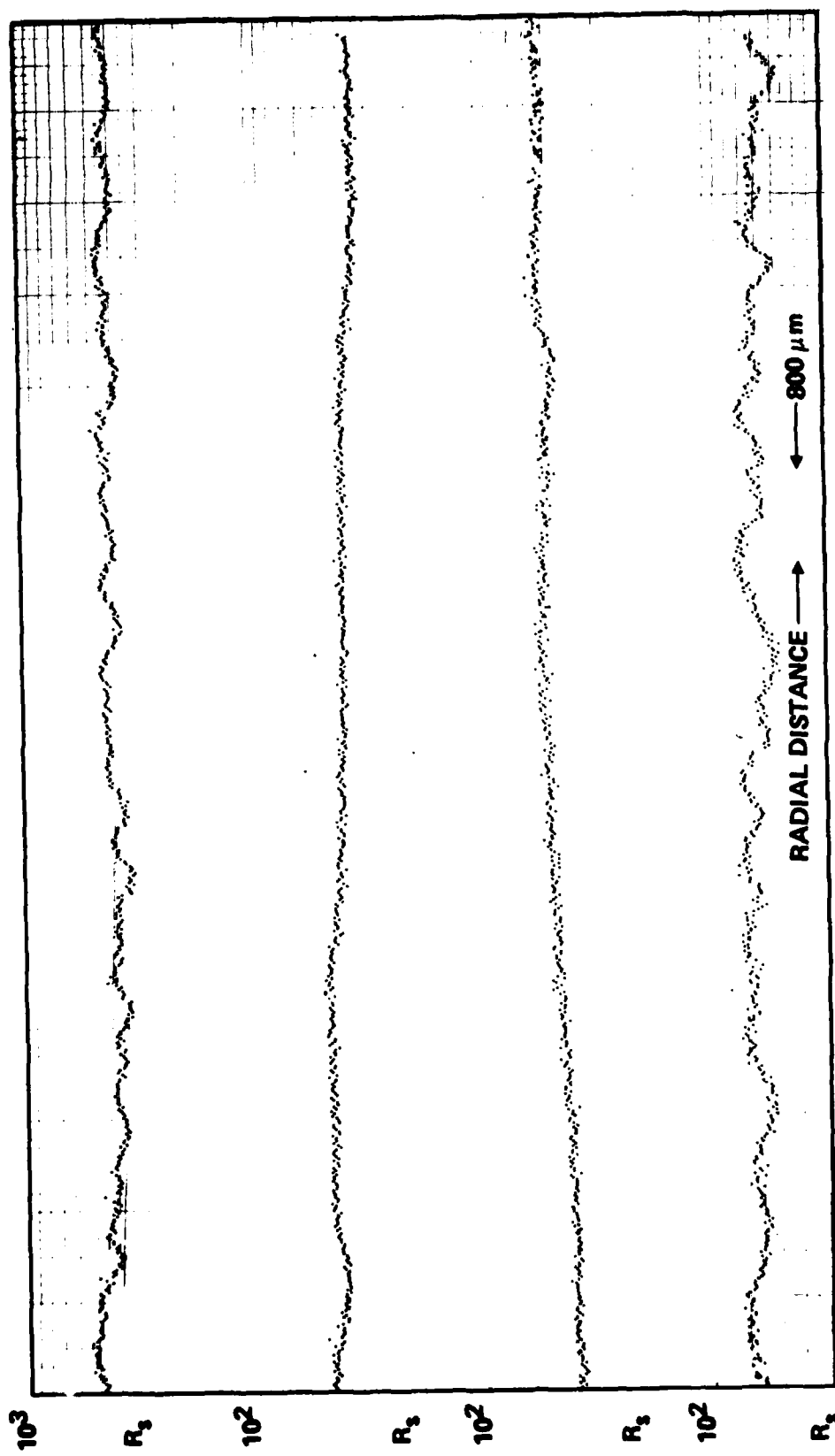
Figure 20. Spreading resistance profile of Z118Ga after 187-hr anneal at 1300°C.
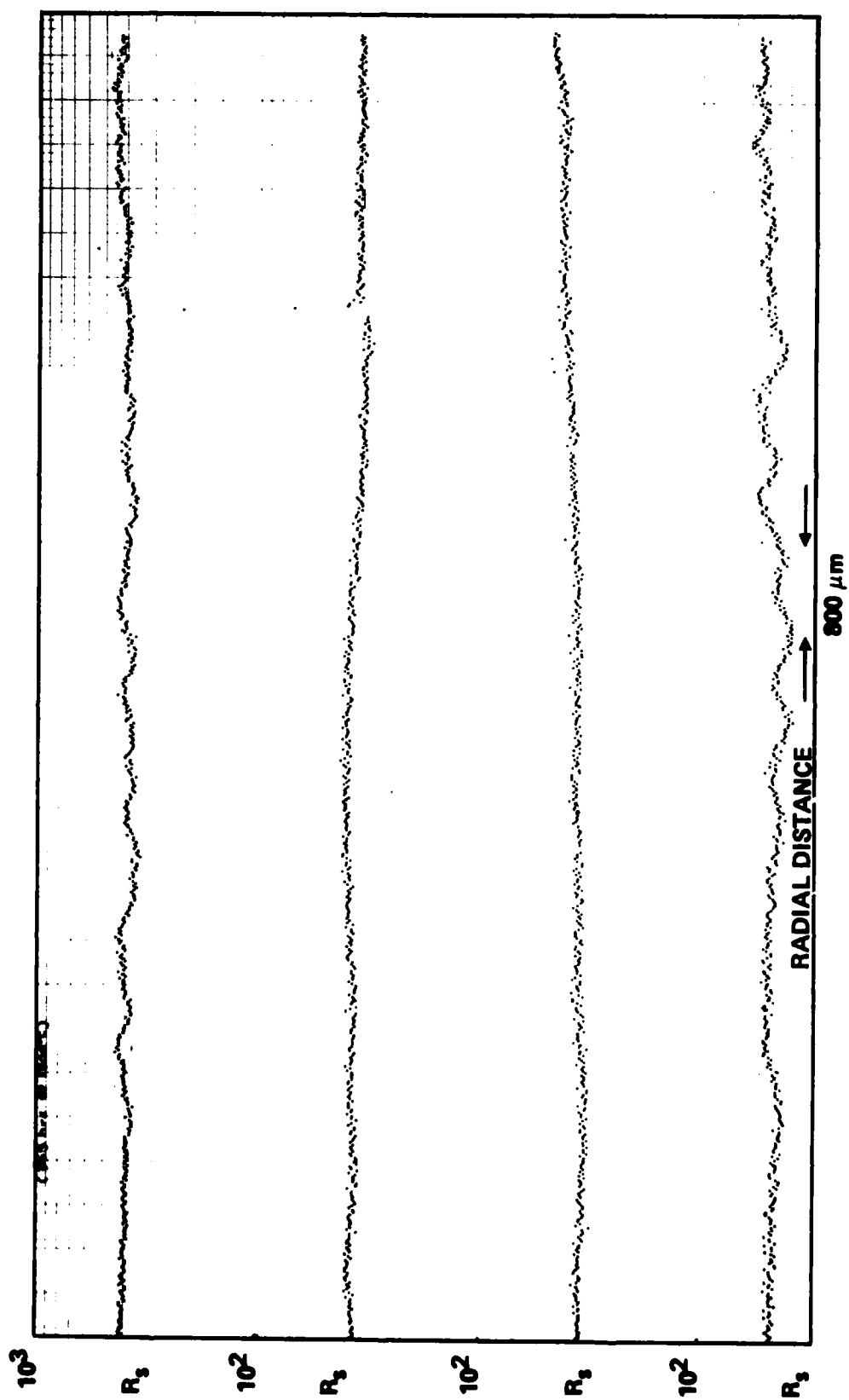
Figure 21. Spreading resistance profile of Z118Ga after 368-hr anneal at 1300°C.
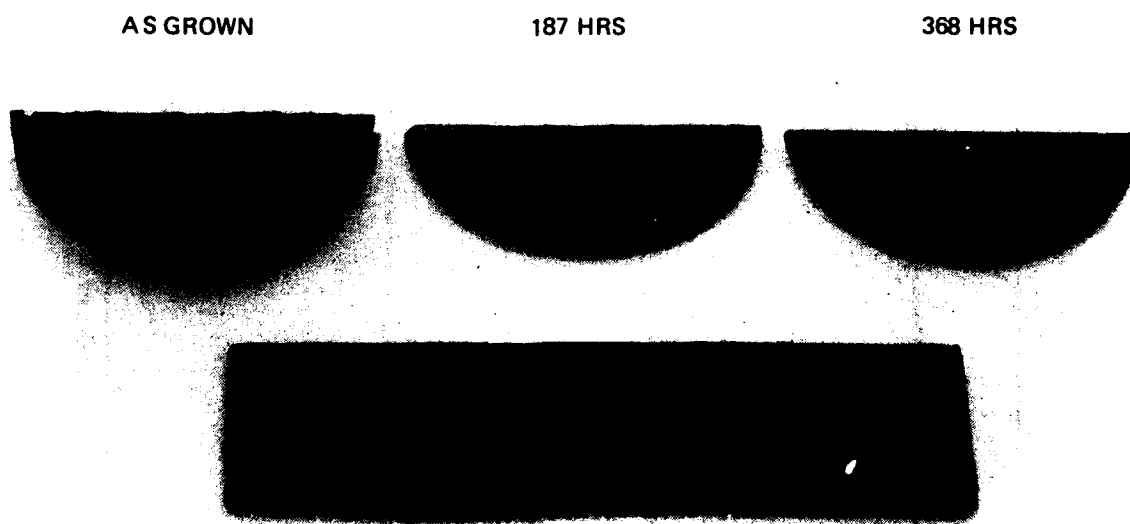
Figure 22. Effect of thermal diffusion at 1300°C on rotational striations.

The microscopic fluctuations are plotted in Figure 23 for the as-grown and diffused samples. After 187 hr, the fluctuations in the right half of the sample do not show marked improvement, which may be due to residual microscopic variations with $\lambda \simeq 800$ µm, as one can see from the spreading resistance plot. After 368 hr, however, they are diffused out to give an overall reduction in fluctuations. The arithmetic means and standard deviations of the fluctuations are tabulated below.

Z118Ga 13 rpm	$\overline{X}$	σ
As-grown	30	15
187 hr	27	14
368 hr	19	11

3. Hall Measurements

Hall and resistivity measurements were made on an as-grown sample that had undergone thermal diffusion at 1300°C for 368 hr. The measured impurity concentrations are given below.

Impurity	As-grown, cm^{-3}	Diffused, cm^{-3}
Ga	7.5×10^{16}	8×10^{16}
B	2.4×10^{13}	5×10^{14}
Donors	2.3×10^{13}	1×10^{15}

The diffused sample shows a marked increase in the boron and total donors concentrations. This is not surprising since the objective was to assess the effect of diffusion on the uniformity of Ga, and no precautions were taken to prevent contamination from the quartz ampoule.
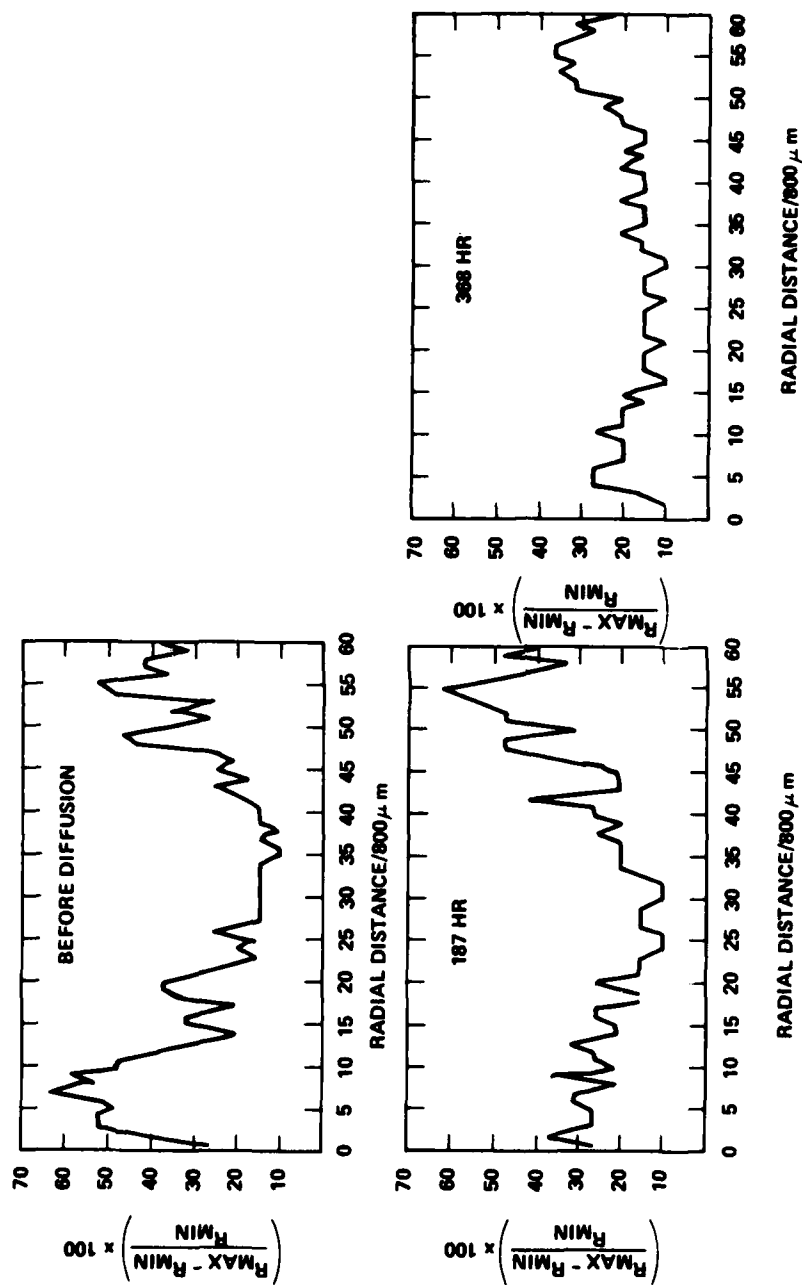
Figure 23. Effect of thermal diffusion at 1300°C as revealed by spreading resistance fluctuation.

58

The contamination may be reduced by placing a high-purity Si cylinder between the sample and ampoule and by also using an ampoule made of high-purity synthetic silica.

The uniformity of the diffused sample was assessed qualitatively by the plot of resistance ratio (R-ratio) versus 1000/T as shown in Figure 24. The measured area was approximately 1800 × 1800 μm. Since the distance between rotational striations for the undiffused part of the crystal was ∿300 μm, the above measurement would give a qualitative assessment of microscopic uniformity.

In a perfectly symmetric and uniform sample, the R-ratio would be 1.0. Geometric asymmetry gives a nonunity, temperature-independent R-ratio. However, nonuniform doping of the Hall sample causes variations in the rate of carrier freeze-out spatially over the sample and leads to a temperature dependent R-ratio. In Figure 24, full scale on the vertical axis represents only a 10% variation in R-ratio. In both the high-temperature regions, where N_{Ga} determines the carrier concentration, and the low-temperature region, where the measured carrier concentration is determined by $N_{Ga}/(N_{donor} - N_B)$, the R-ratio is relatively temperature independent, indicating uniform doping. An example of the resistance ratio for a nonuniform dopant concentration is shown in Curve 1 of Figure B-5 in Appendix B.

I.   OPTICAL ABSORPTION CROSS SECTION OF Ga IN Si

The spectral response of photoconductive detectors depends on the absorption cross section ($\sigma_A (\lambda)$). Therefore, accurate knowledge of the spectral shape of $\sigma_A (\lambda)$ and of its precise values in important spectral regions is essential for meaningful detector modeling. Peak absorption cross section values for Si:Ga reported in the literature differ considerably. The early, widely accepted work of Burstein, Picus, Henvis, and Wallis[8] put the peak value of σ_A for Ga in Si at 5.0×10^{-16} cm^2, but

---

[8]E. Burstein, G. Picus, B. Henvis, and R. Wallis, Phys. Chem. Solids 1, 65 (1956)
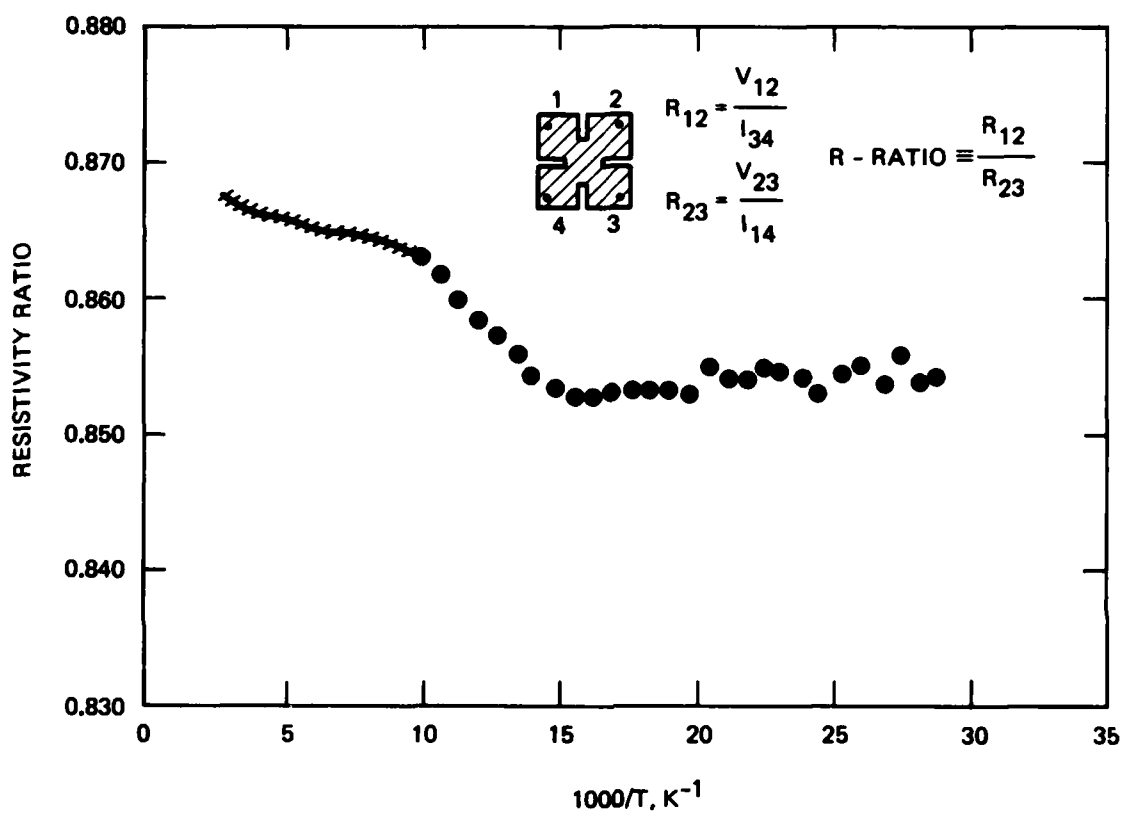
Figure 24. Resistance ratio of annealed sample showing good spatial uniformity.

recently reported results[9,10] indicate a peak absorption cross section of 2.5 to 2.6 $\times$ 10^{-16} cm^2. Such a large uncertainty in peak σ_A would make it impossible to design Si:Ga extrinsic photodetectors with any degree of confidence. Therefore, we independently measured this very important parameter.

Our measurement of optical absorption cross section was made using three samples of Si:Ga from ingots grown for various IR detector programs. The doping in the samples was determined from analysis of Hall-effect versus temperature measurements on samples from positions adjacent to the IR samples. The Hall-effect data obtained for this experimental work are shown in Figures 25, 26, and 27. Si:Ga samples doped with 2.5 $\times$ 10^{16} Ga/cm^3, 5.8 $\times$ 10^{16} Ga/cm^3, and a neutron transmutation counterdoped sample with 6.0 $\times$ 10^{16} Ga/cm^3 were included in our study. We chose these samples to cover a wide range in Ga concentrations within the realm of interest for IR detector applications. Dependences of σ_A on Ga doping, compensation, and method of compensation (including neutron transmutation doping) had been reported in Ref. 10, and we wished to test these unexpected findings in our own experiment. The work in Reference 10 did not include a study of samples doped in the 10^{16} Ga/cm^3 range needed for extrinsic Si:Ga IR detectors.

Differential IR transmission measurements were made using, as a reference sample, an undoped, high-resistivity silicon wafer of the same thickness. By measuring the difference in transmission between the double-side-polished sample wafers and the identically prepared reference wafers, the effects of lattice absorptions were accurately removed, and the absorption coefficient

[9] N. Sclar, Infrared Physics 16, 435 (1976)

[10] W. Hill, R. Helbig, and M.J. Shultz, IEEE Trans. on Electron Devices, ED-27, 10 (1980)
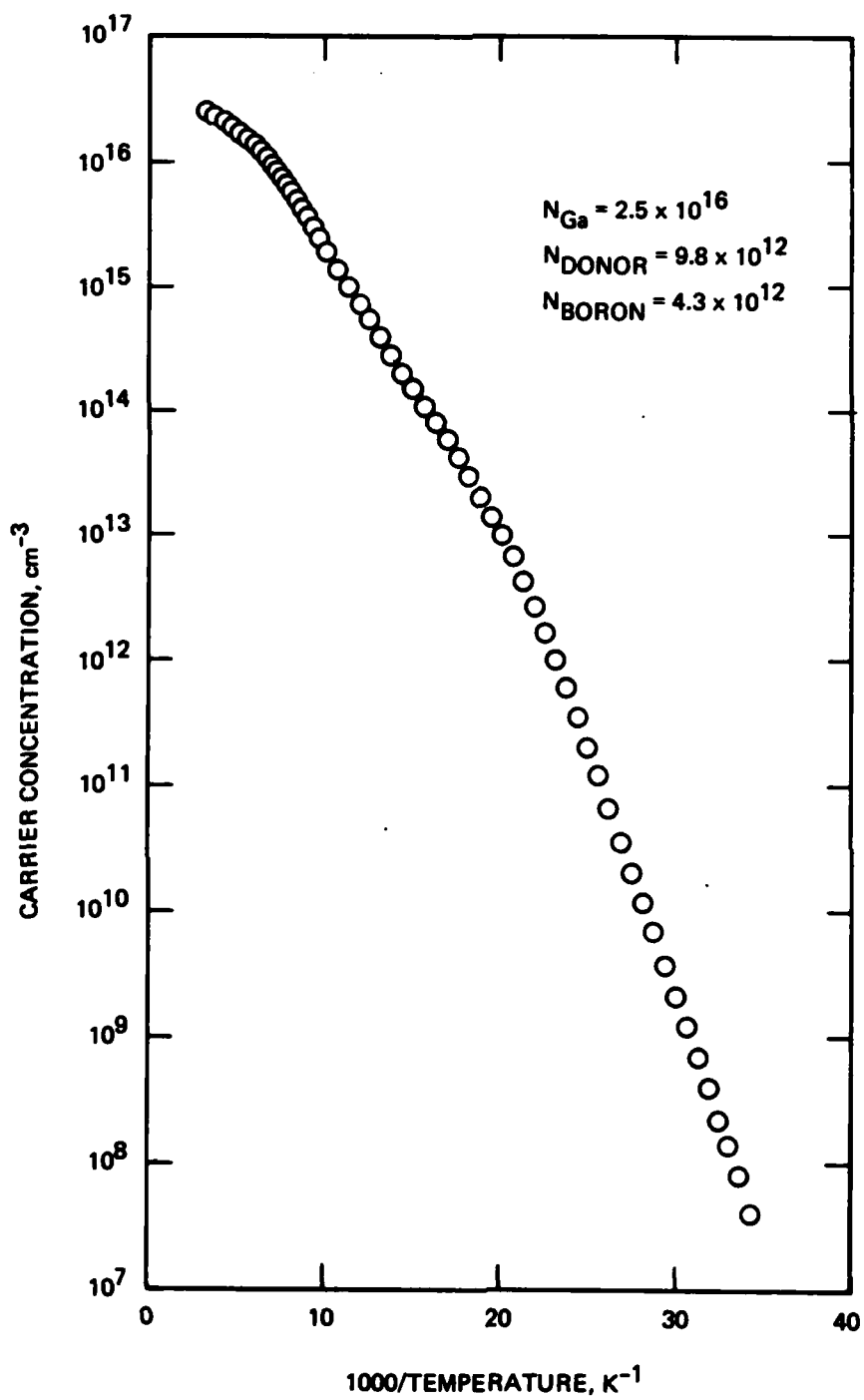
Figure 25. Hole concentration versus 1000/T for Z096Ga.

The plot shows carrier concentration (cm^{-3}) on the y-axis (logarithmic, from 10^7 to 10^{17}) versus $1000/$TEMPERATURE, K^{-1} on the x-axis (from 0 to 40).

$N_{Ga} = 5.8 \times 10^{16}$

$N_{DONOR} = 8.2 \times 10^{12}$

$N_{BORON} = 5.5 \times 10^{12}$
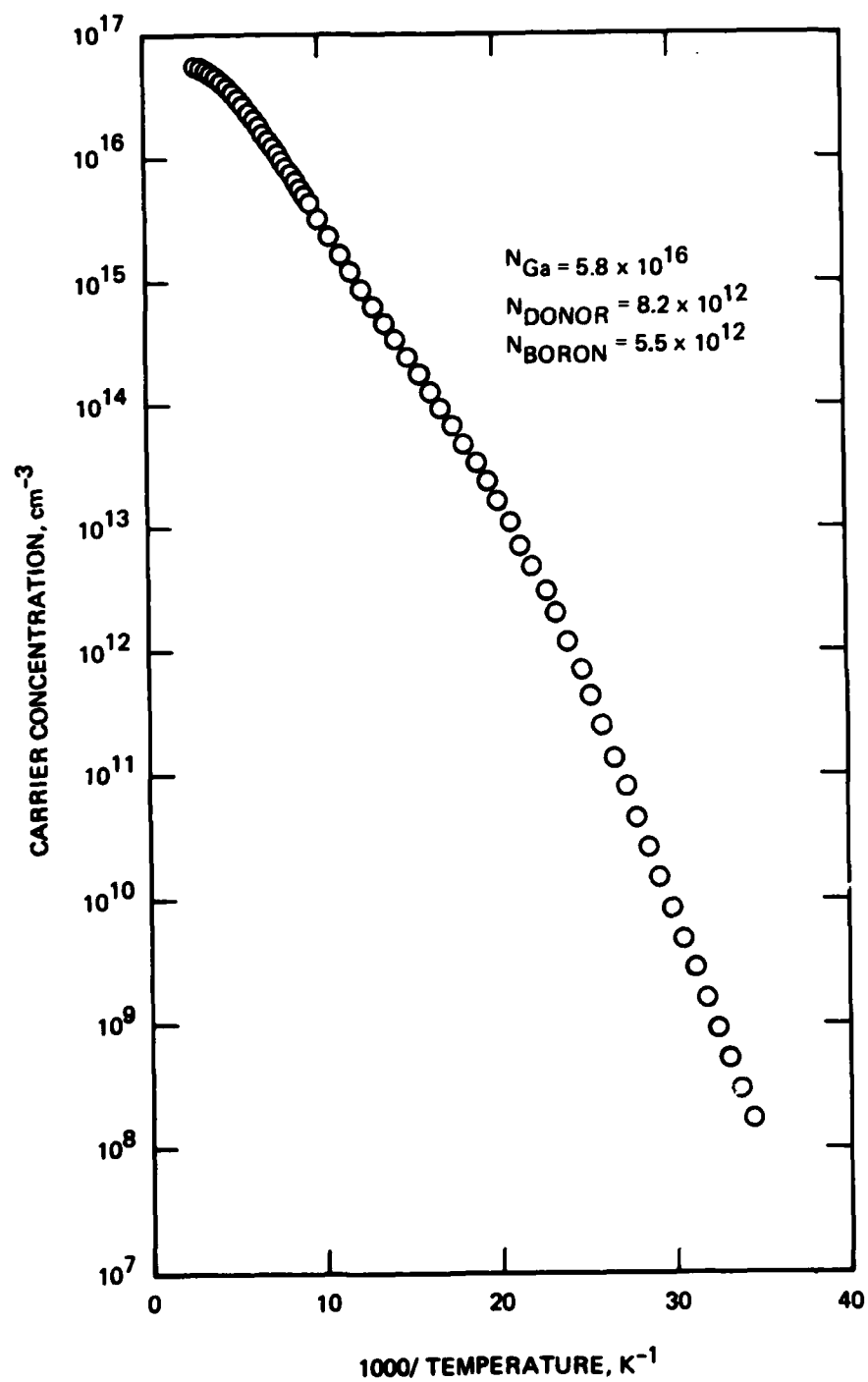
Figure 26.   Hole concentrations versus 1000/T for Z092Ga.
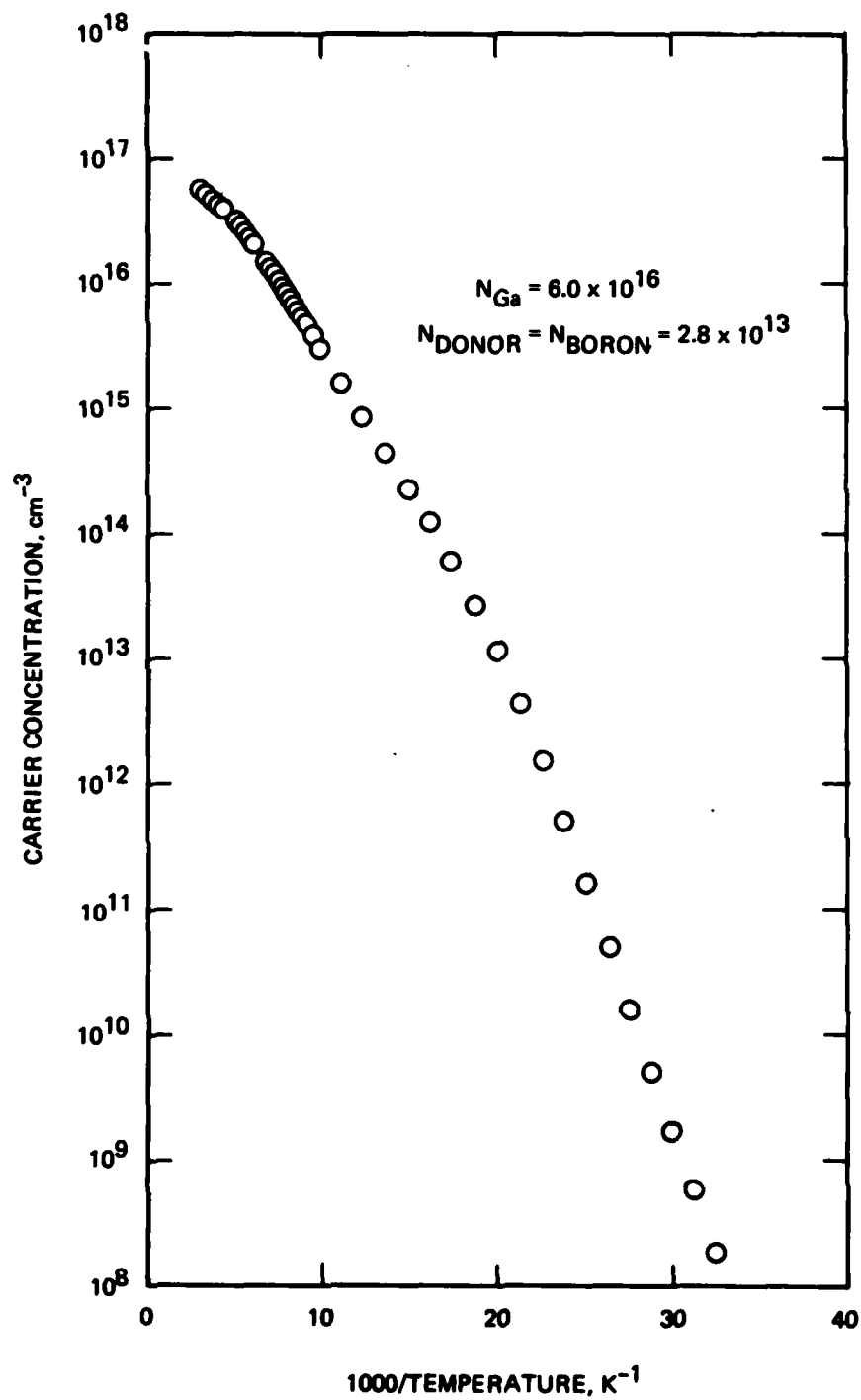
Figure 27. Hole concentration versus 1000/T for Z092Ga.
This sample was neutron transmutation counterdoped.
Material from this transmuted ingot was used in
fabrication of chips for the FTD-ATAC programs.

$$\alpha(\lambda) \;=\; N_{Ga}^{o} \; \sigma_A(\lambda) \tag{7}$$

$$N_{Ga}^{o} \;\equiv\; \text{neutral Ga concentration}$$

was determined for the Si:Ga sample. The transmission measurements were made at 77K. Hall-effect measurements showed that 98 to 99% of the Ga impurity atoms were "frozen out" (neutral) at this temperature. Using these Hall-effect versus temperature measurement results, the neutral Ga concentration at 77K was determined for each sample.

The absorption coefficient $\alpha(\lambda)$ was determined using the relations

$$T_S \;=\; \frac{(1-R)^2 \, e^{-\alpha d_s \, - \, \alpha_{ref} \, d_{ref}}}{1 \, - \, R^2 e^{-2\alpha d_s \, - \, 2\alpha_{ref} \, d_{ref}}} \tag{8}$$

$$T_{ref} \;=\; \frac{(1-R)^2 \, e^{-\alpha_{ref} \, d_{ref}}}{1 \, - \, R^2 \, e^{-2\alpha_{ref} \, d_{ref}}} \;, \tag{9}$$

where Eq. 8 gives the transmission of the sample. Eq. 9 gives the transmission of the reference, which is approximately equal to the maximum transmission (for $\alpha_{ref} = 0$), except in spectral regions with large lattice absorptions. R is the reflectivity and is equal to 0.3008 for silicon, and d_s and d_{ref} are the measured thicknesses of the sample and reference, respectively. The measured differential transmission is T_S/T_{ref}. Absorption cross section is calculated using Eq. 7. A plot of our determination of $\sigma_A(\lambda)$ for Ga in Si is shown in Figure 28 for the three samples studied. Our measurements indicate a peak absorption cross section value of ~ 4.4 to 5.0×10^{-16} cm^2. Estimates of experimental uncertainties expected to give rise to systematic error are indicated by error bars for representative points in each of the three sets

65
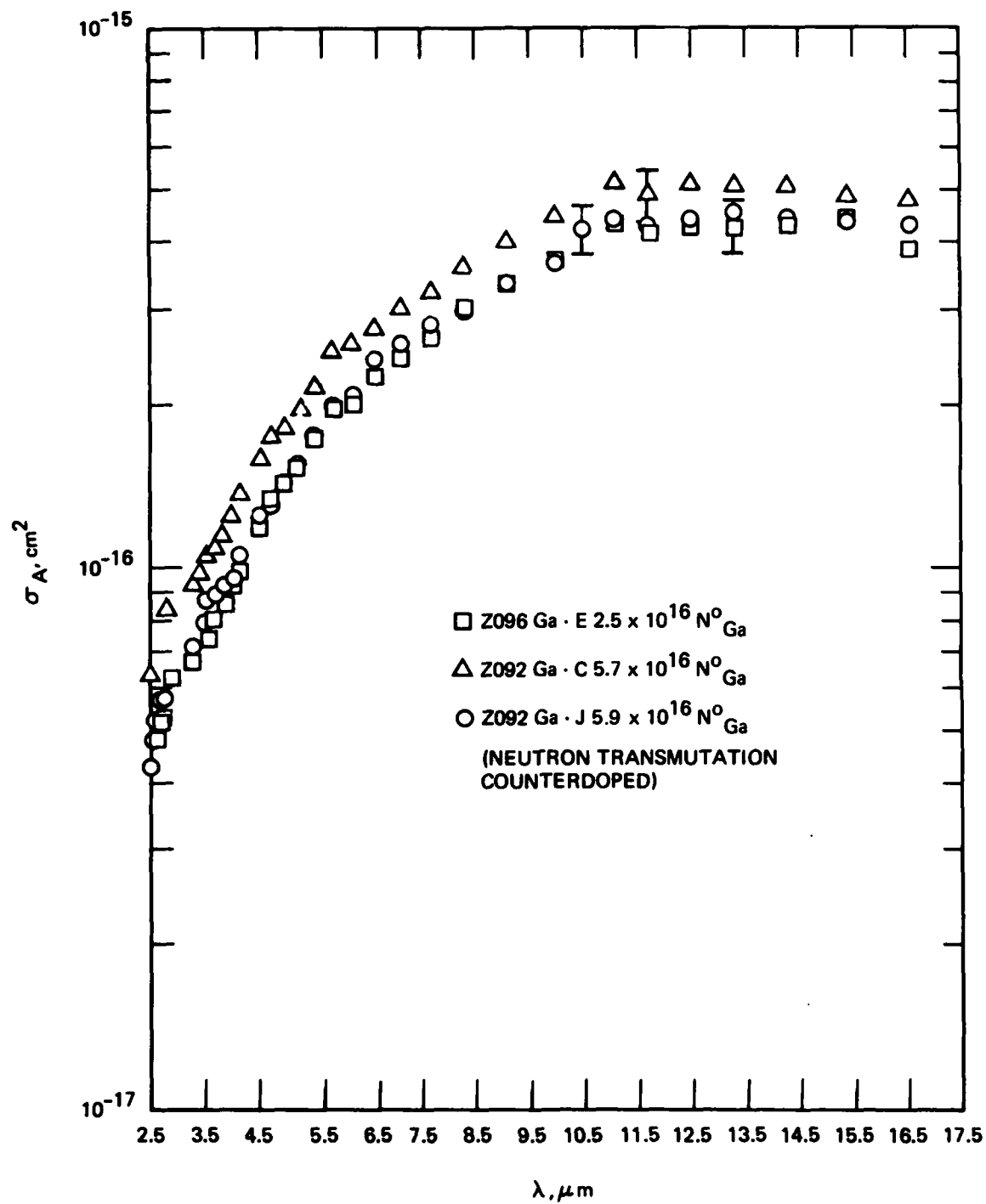
Figure 28. Optical cross section versus wavelength for three Si:Ga
samples. Neutral Ga concentration at the measurement
temperature of 77K is indicated for each sample.

66

of data. Within estimated uncertainties, the three measurements are in reasonable agreement. These results are much closer to those of Burstein et al. than to those reported in Refs. 9 and 10. We do not see a dependence of σ_A on N_{Ga} or on either the concentration or compensating impurities or the method of introducing them. Ga excited state absorptions would appear at λ longer than the 16.7 μm wavelength displayed in Figure 28. These excited state lines are considerably broadened at 77K in comparison to these same lines near detector operating temperatures (~25K) and are not included in the figure.

This determination of the fundamental parameter $\sigma_A(\lambda)$ for Si:Ga allows us to confidently predict the maximum quantum efficiency, $\eta(N_{Ga}\sigma_A(\lambda)d)$, that can be expected from the Si:Ga material from which extrinsic photodetectors are fabricated.

J. CRYSTAL FOR FOCAL PLANE ARRAY FABRICATION

Near the close of the program, a crystal of detector quality was to be grown to embody the most promising features found during this investigation. As discussed above and in Section 3, fluctuations in the concentration of Ga are minimized as the growth rate is reduced and the rotation rate is increased. As also noted, crystal growth becomes progressively more difficult as the growth rate is reduced below a rate of 4 mm/min. Therefore we decided, in view of the limited time and resources remaining in the program, to attempt a crystal growth run with detector-grade polycrystalline Si at a growth rate of 2.5 mm/min and a rotation rate of 10 rpm.

Several attempts at growth under these conditions were initiated but were unsuccessful because of twinning very early in the crystal growth. However, we finally succeeded in obtaining a section of single crystal about 3.5 in. long before twinning set in. This piece of crystal (designated Z206Ga) was ground to 2 in. in diameter, flatted, and given a spiral groove for identifying wafer location. Several wafers were then sliced from the seed and tang ends of this crystal piece and

double-side polished to provide evaluation wafers for Hall measurements, neutron transmutation doping, and eventual detector fabrication.

An outside vendor performed the grinding, slicing, and polishing operations. From these polished wafers, we prepared Hall samples and also performed dislocation etching. The seed end of the crystal was free of defects, as is typical for a zero-dislocation single crystal. However, the slices from the tang end showed severe dislocation and were probably not suitable for detector use. Also, the tang end of this crystal contained a crack that resulted in a loss of about 10 to 15% of the area of each wafer. It is not known whether this crack was caused by mishandling during the grinding operation, by residual strain remaining in the crystal because of the slow growth rate, or by a combination of the two. Until more of the crystal has been sliced and evaluated, we will not know how far the crack and the highly dislocated region extend toward the seed end.

The Hall evaluation of wafers taken from both ends of Z206Ga show a very uniform Ga concentration and low concentrations of both B and donors. The van der Pauw samples measured were cut from the central region of the slices and gave the following concentrations in atoms/cm^3.

	N_{Ga}	N_B	N_D
Tang end	7.7×10^{16}	2.9×10^{12}	3.4×10^{12}
Seed end	7.7×10^{16}	5.12×10^{12}	2.7×10^{12}

The data obtained for carrier concentration, carrier mobility, and resistivity as functions of temperature for the seed end of crystal Z206Ga are given in Figures 29 through 31. The corresponding data for the tang end specimen are essentially identical to those for the seed end.

68
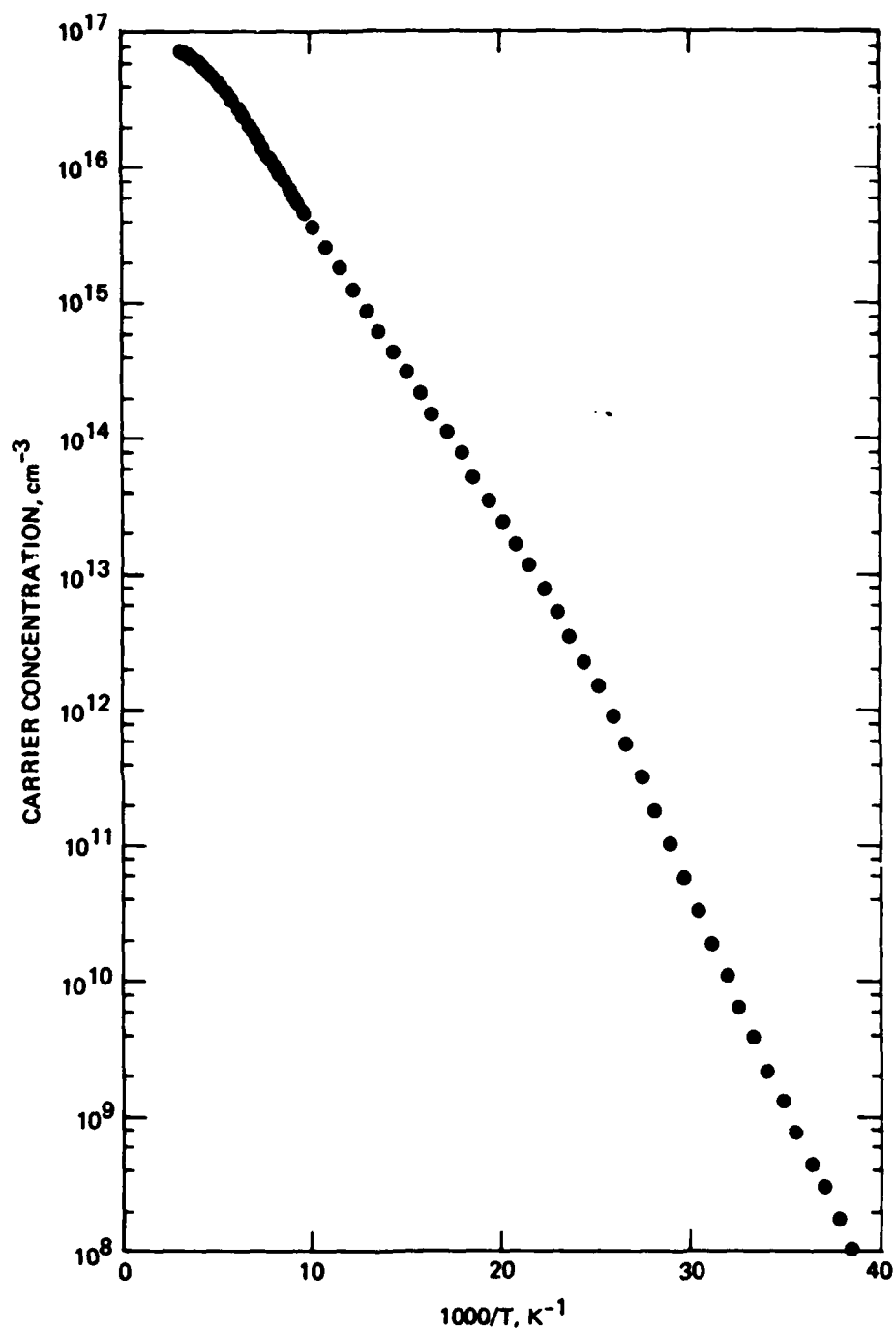
Figure 29. Carrier concentration for the seed end of cyrstal Z206Ga. N_{Ga} is 7.7×10^{16} Ga atoms/cm^3.
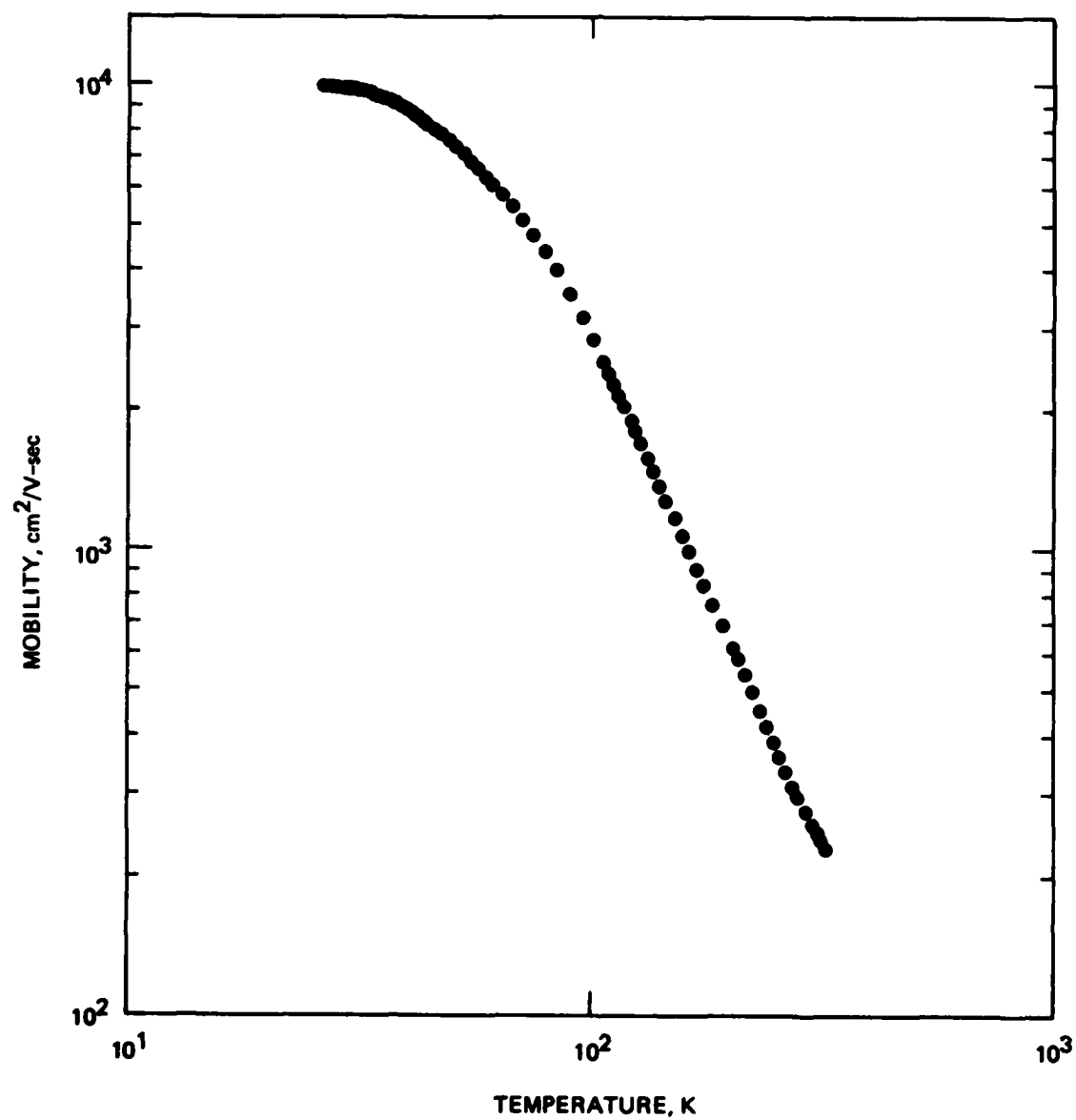
Figure 30. Carrier mobility for the seed end of crystal Z206Ga.
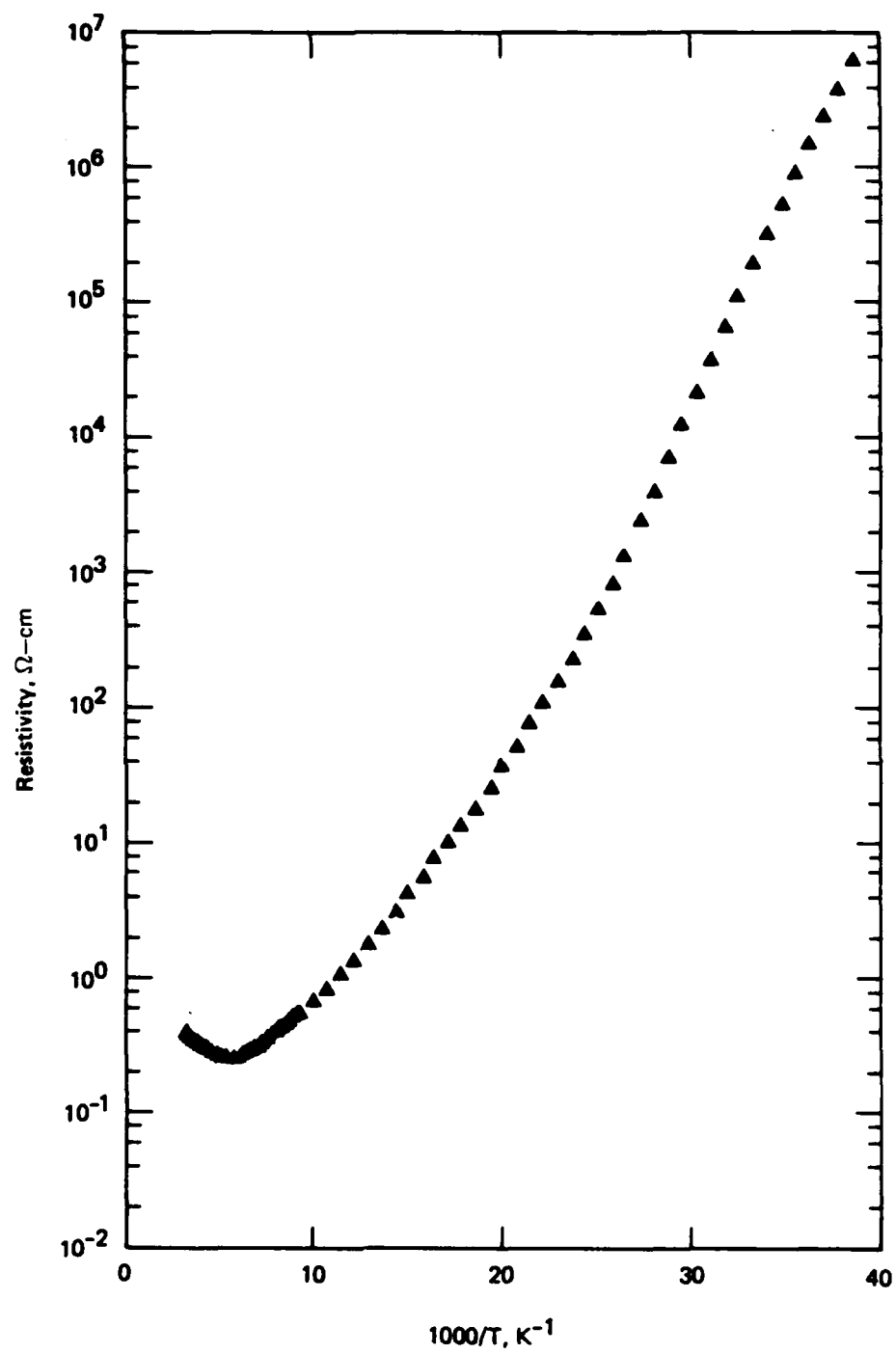
Figure 31. Resistivity for the seed end of crystal Z206Ga.

Wafers from the seed end have been given to the Carlsbad Research Center, where they will be sent to Texas A & M University for neutron transmutation doping to ensure adequate and uniform compensation. Detectors will then be fabricated in the production line normally used for LADIR, FTD, and other FLIR detectors. We expect to report results from these samples in an addendum to this report as soon as the data become available.

This final crystal growth run suggests that attempts to grow crystals at rates below 3.0 mm/min involve a very high risk of twinning and consequently promise a very low yield of dislocation-free single crystal. However, at 3 mm/min we have not experienced any unusual difficulty at a variety of rotation rates up to 10 rpm. On other programs, we have occasionally encountered crystal oscillations during growth at 10 rpm when the grown crystal was longer than 10 in. This behavior is apparently the result of the excitation of a natural resonant vibrational frequency for the large crystal mass, which is supported at the lower end by only an ∿0.12-in.-diameter seed rod. By slowing the rotation to 6 rpm, the resonant frequency is no longer excited and the oscillation quickly damps out. Therefore, our recommendations at this time for the growth of 2-in. (100) Si:Ga crystals with minimal concentration fluctuations is a growth rate of 3 mm/min and a rotation rate of about 10 rpm.

SECTION 3

DISCUSSION AND CONCLUSIONS

We have examined the segregation behaviors of Ga and B mainly as a function of growth rate and rotation rate for the float-zone growth of Si and have assessed the effects of these growth parameters on the interface shape and the radial microscopic distribution of dopants. We found that a combination of slow growth rate and fast rotation rate contributes to the optimum interface shape and dopant uniformity. Experience gained in this program has shown that growth at rates as low as 2 mm/min is possible but that below 3 mm/min the yield of single crystal is very low. Therefore, our current recommendation is that crystals be grown at a rate of 3 mm/min at rotation rates up to 10 rpm. Post-growth annealing of a crystal, though time consuming, was shown to be an effective way to further improve on the distribution of dopants in the crystal.

Toward the close of the program, we grew a crystal Z206Ga at 2.5 mm/min and 10 rpm. Wafers were prepared from the seed and tang ends and Hall evaluations have been made. Wafers have also been supplied to our FPA fabrication activity, where they will be submitted for neutron transmutation and fabrication into detector arrays. Performance results from these samples, as well as from two subsequent Si:Ga crystals, are reported later in Section 4, Addendum, which was prepared several months after the writing of the rest of this report.

A. SHAPE OF GROWTH INTERFACE

There are many papers[11,12,13,14] related to the study of the interface shape, the factors influencing the shape, and also the structural

---

[11] E. Billig, Proc. of Roy. Soc. A, 235, 37-55 plate 5 (1956)

[12] J.H. Braun and R.A. Pellin, J. Electrochem Soc. 108 969-974 (1961)

[13] N. Kobayashi, J. of Crystal Growth 43, 417-424 (1978)

[14] W. Keller, J. of Crystal Growth 36, 215-231 (1976)

defects caused by the various shapes of the interface. When the shape of the interface is either convex or concave, the growing crystal suffers, depending on the curvature, either a compressive or tensile stress. The stresses can be very severe in a crystal having the cubic diamond or zinc blende structure (A4 or B5) with an open lattice such as Si which expands by a considerable amount on solidification. High etch pit density is found to be concentrated along the curved portion of the growth surface, while the flat portion is relatively free of defects. According to the theory introduced by Billig,[11] the radial temperature gradient can be expressed as

$$\frac{dT}{dr} = \frac{dT}{da} \cdot \frac{da}{dr} ,\qquad (10)$$

where dT/da is the axial temperature gradient and da/dr is the curvature of the interface. According to the theory,[11] the curved interface is a proof of the existence of a radial temperature gradient, which is essential to the generation of dislocations. In float-zoned growth, the axial temperature gradient and the curvature are sensitively influenced by the rate at which the crystal is lowered because of the very limited paths through which the heat of crystallization must be dissipated.

The crystal rotation, which had no influence on small-diameter crystals ($\leqslant$22 mm) when varied from 0 to 60 rpm by Braun and Pellin,[12] was found to be very effective in reducing the concavity of the interface toward the crystal in the central region for 50-mm-diameter crystals. The probable melt flow pattern proposed by Keller[14] in Figure 32, although oversimplified and not explaining the complex "feathering" pattern observable in striation-etched crystals, does serve to illustrate the bulging of the central region of the interface. When the crystal is rotated fast, thermal convection flow is enhanced, and the cool downward flow through the center of the melt cools the central part of the crystal
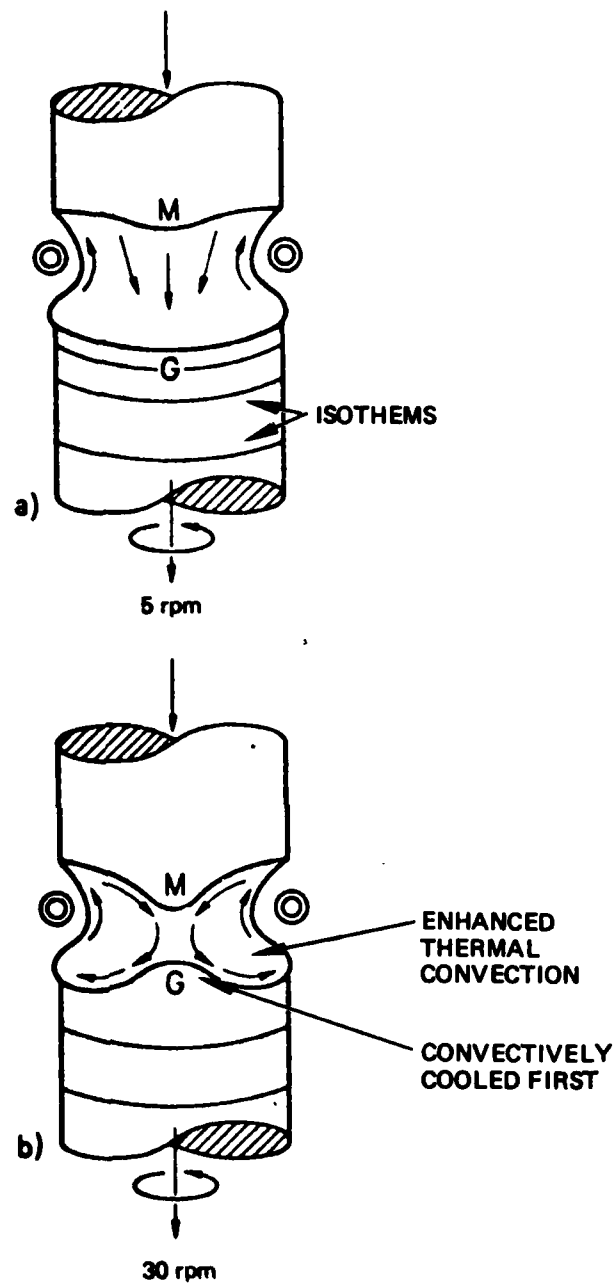
Figure 32.
Effect of rotation of the seed
(growing interface): (a) low
seed rotation rate, (b) fast seed
rotation rate (M = melting interface,
G = growing interface).(From Keller[14])

75

bulge growing upward into the melt. In the case of $\langle 111 \rangle$ growth, the above flow pattern and the resulting temperature distribution induce facet growth.[15]

In the first three sections of crystal of Z108Ga, the growth rate was kept constant while the rotation rate was varied from 6 to 8 to 3 rpm. Figure 2 clearly shows the response of the growth interface to the rotation rate in the three sections from the seed. A slight bulging is visible in the latter half of section 2. When the rotation is reduced to 3 rpm, the center part caves in to render the interface severely concave towards the melt. The interface flattens in the last three sections as the growth rate is reduced.

Figure 6 shows striations (light lines) in a segment of Z118Ga where the growth rate was kept constant at 4 mm/min and the rotation rate was increased from 8 to 13 rpm. The transition from 8 to 13 rpm is clearly visible from the spacings between striations, which decrease from 500 to 300 μm.

When the striations are examined more closely, the lines are not continuous at the center of the crystal but show a complex "feathering" pattern (white lines) as shown in Figure 33, which is the magnified view (50x) of the central part of crystal Z118Ga shown in Figure 6. This complex morphological feature, which causes compositional variation, was studied extensively by Murgai et al.[16] on an Sb-doped Czochralski-grown Si crystal, and crucible rotation was found to be the prime cause. The feathering pattern shown in Figure 34, which is the magnified view (185x) of the central section of Figure 33, resembles

---

[15]A. Muhlbauer, "Semiconductor Silicon 1973" edited by H.R. Huff and R.R. Burgess, p. 107-118, The Electrochemical Society, Softbound Proceedings Series, Princeton, N.J. (1973)

[16]A. Murgai and W.A. Westdorp, "Semiconductor Silicon 1977" edited by H.R. Huff and E. Sirtl, p. 83, The Electrochemical Society, Softbound Proceedings Series, Princeton, N.J. (1977)

Figure 33. Enlarged section (50x) of Z118Ga
showing "feathering".

Figure 34. Enlarged section (185x) of 0118Ga showing "feathering".

very closely that studied by Murgai in which striations fade gradually and branch off into several striations.

The general convective flow pattern for Czochralski growth may be applicable to float-zoned growth in which the growing crystal acts as a crucible bottom. The prime role of crystal rotation is to make the momentum boundary layer more uniform by shielding it from the temporal (transient) and spatial variations in the thermal convection flows. The Taylor-Proudman[17] cells appear to stabilize the boundary layer, as evidenced by the decrease in the microscopic compositional fluctuations when crystal rotation is increased. Nevertheless, the complex feathering pattern is observable even at a high rotation rate of 13 rpm. As pointed out by Murgai,[16] the sudden deceleration in crucible rotation gives rise to forced transient convective flows such as the Ekman flow. The possibility that such transients in crystal rotation cause the feathering cannot be ruled out at this stage without further examinations. More correlations of the morphological feature of feathering with compositional variation must be established to better our understanding of the mechanism of feathering formation.

B.   COMPOSITIONAL UNIFORMITY

In crystal Z108Ga, the growth rate (pull rate) was kept constant at 4 mm/min while the rotation rate was varied from 6 to 8 to 3 rpm in the first three sections to assess the effect of rotation rate on compositional uniformity. Figure 3 shows the microscopic spreading resistance variations on each 800-µm segment across the diameter of the crystal. In the last two sections, the growth rate was reduced to 2 mm/min and then increased to 3 mm/min while the rotation rate was kept constant at 3 rpm. Figure 4 shows their microscopic variations.

---

[17] S. Chandrasekhar, Hydrodynamic and Hydromagnetic Stability, p. 83, Oxford Press (1961)

Comparing the three sections in Figure 3, it is difficult to understand the increase in microscopic fluctuations at a crystal rotation rate of 6 rpm. The boundary layer should, according to the Cochran analysis, become thinner as the rotation rate of the crystal is increased. It should also be more uniform because the forced fluid flow normal to the interface should shield the boundary layer from thermal convection currents. Further analysis of the 6 rpm data in comparison with the other sections of Z108Ga and with other crystals is discussed below. Comparison of 3 and 8 rpm shows a more uniform microsopic fluctuation for the faster rotation rate. The plot of average concentration in each 800-μm segment in Figure 5(a) shows more convincingly that faster rotation leads to higher uniformity.

Reduction in the growth rate from 4 to 3 mm/min leads to higher uniformity as seen from the comparison of Figures 3 and 4 for the same rotation rate of 3 rpm. Also, a better microscopic compositional uniformity as measured by the four-point probe is realized with the reduction in the growth rate.

The arithmetic means together with the associated standard deviations were tabulated for the microscopic spreading resistance and concentration fluctuations. There are no definite correlations between the values of $\overline{X}$ and the rotation rate or growth rate, although there are apparent improvements in the actual spreading resistance plots.

To better assess compositional uniformity, the amplitudes in an arbitrary unit from the plot of log R_s versus distance across the diameter in the single-probe mode were measured and plotted in Figure 35. The amplitudes of variations in the core were determined by measuring the distance between two straight lines connecting the crests and valleys of spreading resistance fluctuations located on both sides of the central region as shown in Figure 36. Ten in the arbitrary unit scale of Figure 35 corresponds to a variation in N_{Ga} of 2×10^{16} cm^{-3}. In the plot of log R_s versus distance in the radial direction, the central nonfluctuating quiescent region is flanked by more vigorously fluctuating
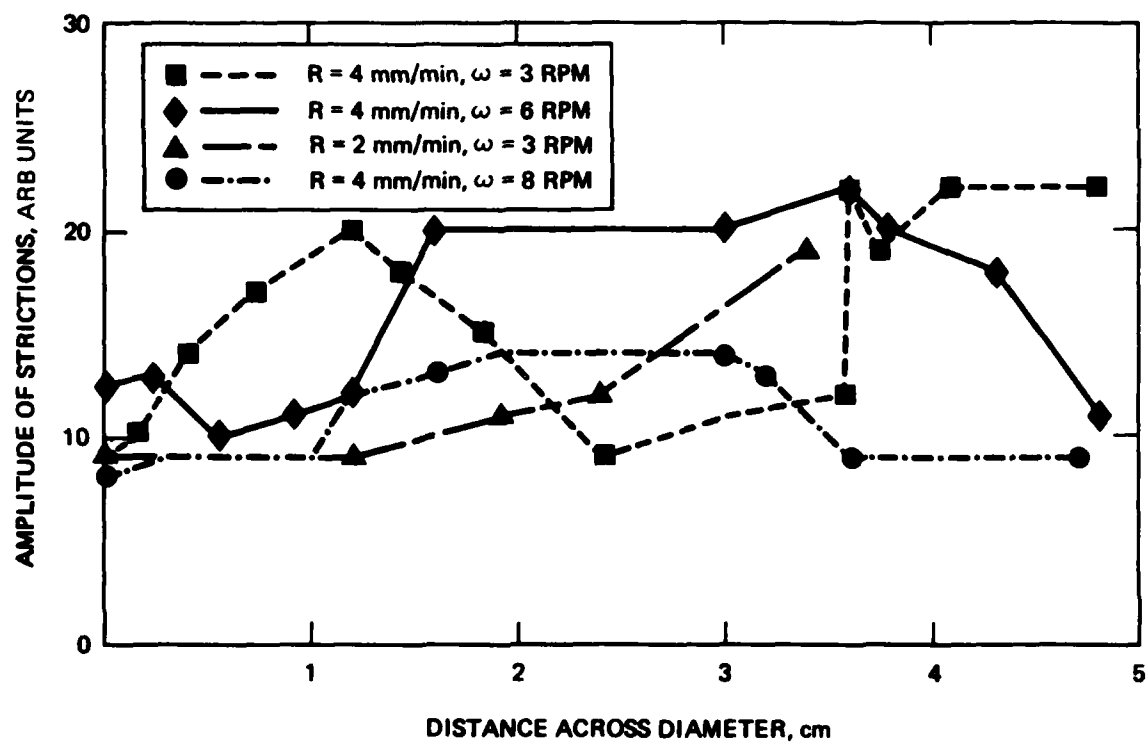
Figure 35.   Variations in amplitude of striations across a diameter
in Z108Ga.
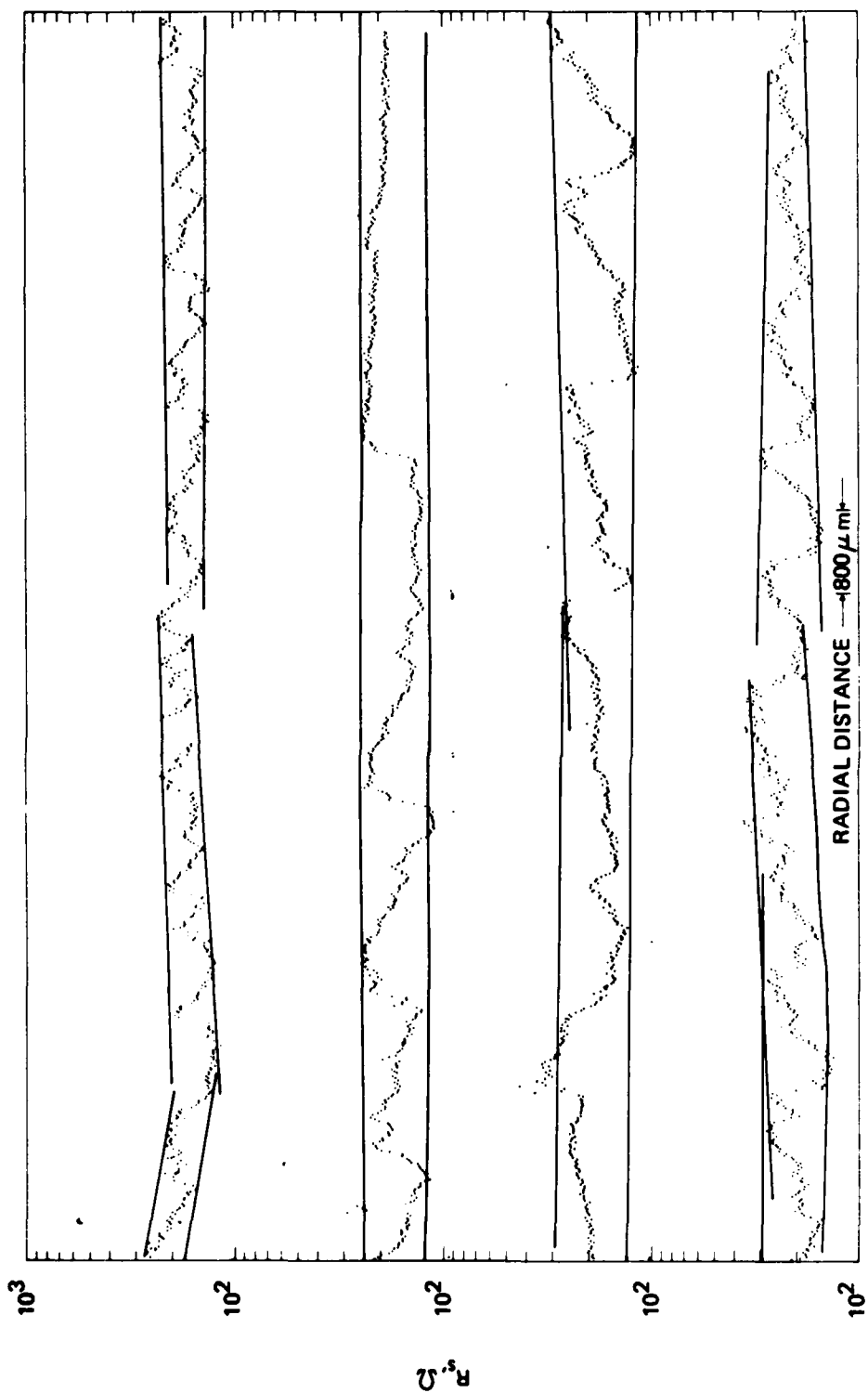
Figure 36. Method for determining striation amplitudes for Z108Ga; growth rate = 4 mm/min, rotation rate = 8 rpm.

peripheral regions unless the interface is also sharply curved in the central region. The hemispherical volume measured by the probe is on the order of 10^{-9} cm^3. Hence, at the core of the crystal, where striations run more parallel to the measuring surface, fewer fluctuations are observed, whereas more vigorous variations in spreading resistance are seen toward the periphery, where the probe transverses many striations.

For the three sections in Figure 35 where the rotation rate was varied from 6 to 8 to 3 rpm at a constant growth rate of 4 mm/min, the best symmetry and the lowest overall amplitude of fluctuations are seen in the section with the highest rotation rate. It is surprising that the amplitudes are higher in the center than at the periphery for the 8-rpm section. According to the steady-state segregation theory of Burton, Prim, and Slichter,[1] the variation in the effective distribution coefficient is caused by the fluctuations in the microscopic growth rate R and the boundary layer thickness δ. According to the relationship by Morizane et al.,[18] the instantaneous growth rate R is a function of the growth rate (pull rate), R_o; the temperature variation during one revolution of crystal, ΔT; the rotation rate of crystal, ω; and the axial temperature gradient, G:

$$R = R_o - \frac{\Delta T \omega}{G} \cos \omega t .$$ (11)

At the rotation axis, ΔT is zero and the microscopic growth rate corresponds to the pull rate. The amplitude of microscopic growth rate increases with radial distance and rotation rate if the rate of rotation is slow enough that the interface responds to the variations in temperature. The average microscopic growth rate increases in the presence of backmelting since the growth rate must accelerate correspondingly to maintain the constant pull rate.

---

[18] K. Morizane, A.F. Witt and H.C. Gatos, J. Electrochem Soc. 114, 738 (1967)

The increase in the amplitude of spreading resistance variations at the core, therefore, is not due to the increase in the microscopic growth fluctuation but to the thicker diffusion boundary layer. According to the Cochran analysis, the thickness δ is related to the kinematic viscosity of the liquid ν and the diffusion coefficient of the solute D in the melt by the relationship

$$\delta = 1.6D^{1/3}\nu^{1/6}\omega^{-1/2} . \tag{12}$$

This relationship applies to an infinite disk rotating in a quiescent isothermal liquid without thermal convections or edge effects. In the actual melt growth of Si, whether it be Czochralski or float-zone growth, the thickness of the boundary layer varies by a considerable amount spatially (see, for example, Ref. 16). The expression by Burton, Prim, and Slichter[1] for the steady state segregation of solute may be differentiated with respect to the microscopic growth rate to assess the differential change in the effective distribution coefficient with the microscopic growth rate. Figure 37 shows the plot of $\partial k_e/\partial R$ versus δ and ω for various microscopic growth rates; it indicates that the differential change rises rapidly as δ increases. On the other hand, as δ decreases, the variations in microscopic growth rate have little effect on the compositional variations. A similar analysis using Eq. 3 leads to the same conclusion (cf Figure 1).

In the presence of spatially nonuniform transient thermal convection flows, especially at low rotation rates, the interface shape is severely concave towards the crystal and is believed to be microscopically rough with a nonuniform boundary layer. Also, the boundary layer will be thinner at the periphery because of the greater tangential velocity and the increased radial velocity of the thermal convection flows.[19]

---

[19] J.R. Carruthers, J. of Electrochem Soc. 114, 959-962 (1967)
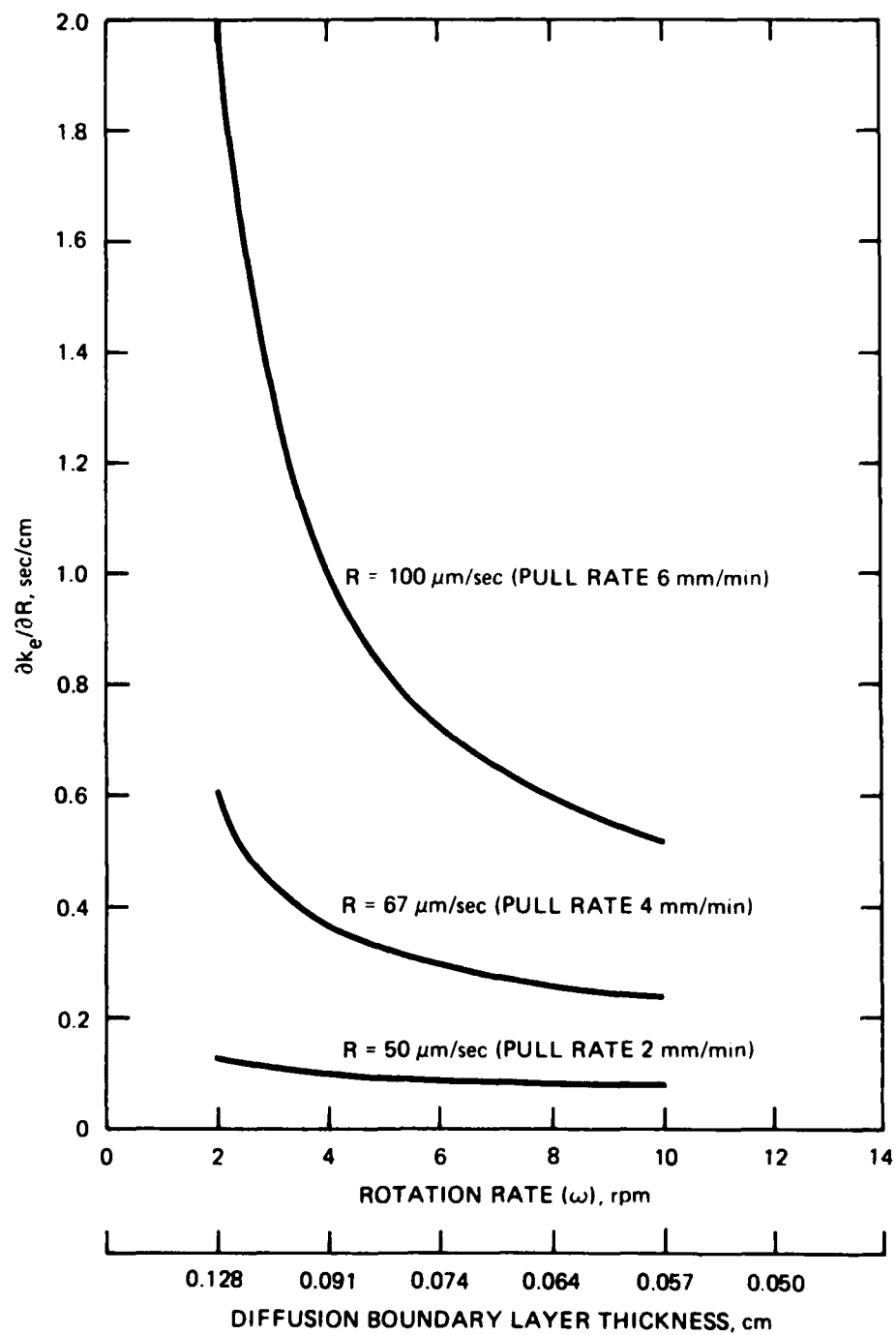
Figure 37.   Differential change in effective distribution
coefficient with microscopic growth rate versus
microscopic growth rate and diffusion boundary
layer thickness.

85

The various radial distributions of amplitudes shown in Figure 35 may, then, be reasonably explained from the above discussion. At a low rotation rate of 3 rpm at a 4 mm/min growth rate, the interface is curved sharply, and δ is thick and nonuniform. As shown for this condition in Figure 35, the increasing growth rate fluctuations towards the periphery on the right side are not diminished by the thick boundary layer. When the rotation rate is increased to 6 rpm, the amplitudes are diminished at the periphery but a wide stagnant region above the core gives rise to a thick boundary layer and a large variation in composition. When the rotation rate is increased further to 8 rpm, the boundary layer becomes more uniform and thinner, as evidenced by a generally smaller and more uniform amplitude distribution.

In crystal Z180Ga, the growth rate was reduced to the lower limit beyond which dislocation-free growth is difficult. The growth rate was lowered from 3.2 mm/min to 3.0 mm/min while the rotation rate was increased from 4 to 10 rpm. In the final section, the growth rate was lowered to 2.5 mm/min while the rotation rate was maintained at 10 rpm.

Figure 38 shows plots of amplitude distribution as determined from the semilogarithmic plot of spreading resistance R_s versus distance along a diameter in the single-probe mode. Comparing the results of Z108Ga and Z180Ga shows that the amplitudes are generally lower for Z180Ga even at low rotation rates of 4 and 6 rpm (Figure 38). The general shapes of distributions are nonuniform but show an improvement at 6 rpm. The decrease in amplitude in comparison with Figure 35 arises from the lower average microscopic growth rate corresponding to the lower growth rate.

A substantial improvement is achieved when the rotation rate was increased to 8 and 10 rpm as shown in Figure 39 and reflected in the reduced excursions of spreading resistance in Figure 40(a). At these low growth rates and high rotation rates, the interface is believed to undergo remelting on every revolution. The boundary layer, as a result, is likely to be orders of magnitude thinner than the
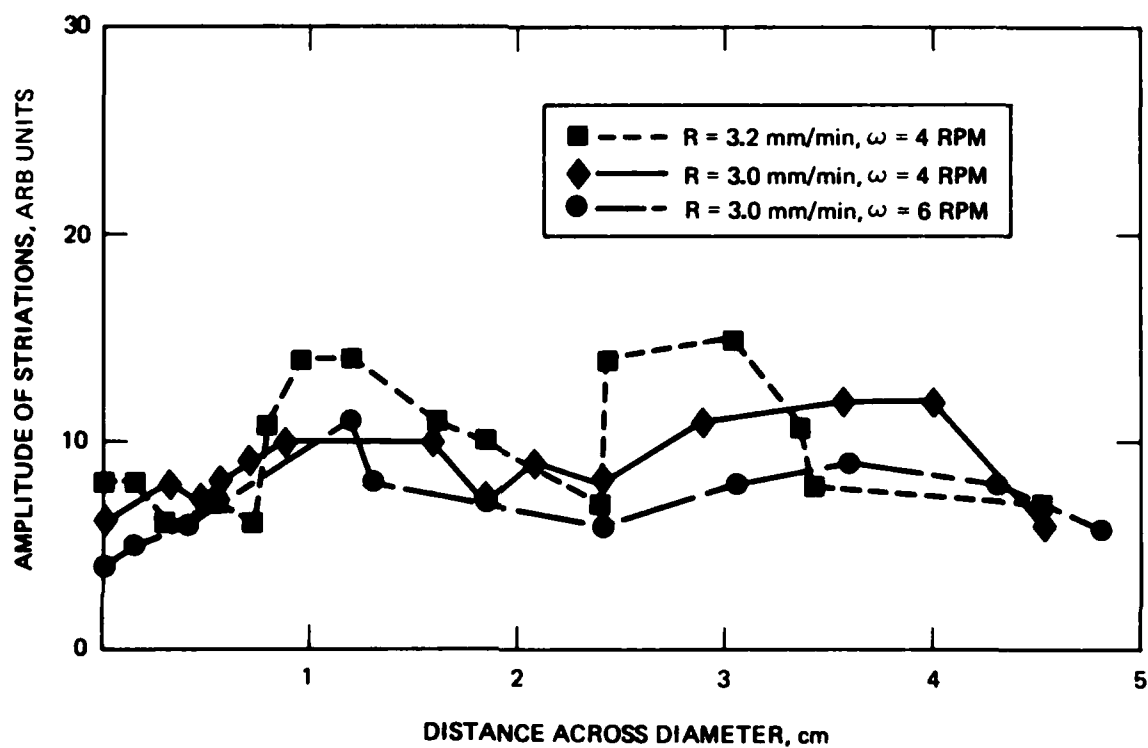
Figure 38.   Variations in amplitude of striations across a diameter in
Z180Ga.   Sections 1, 2, and 3.
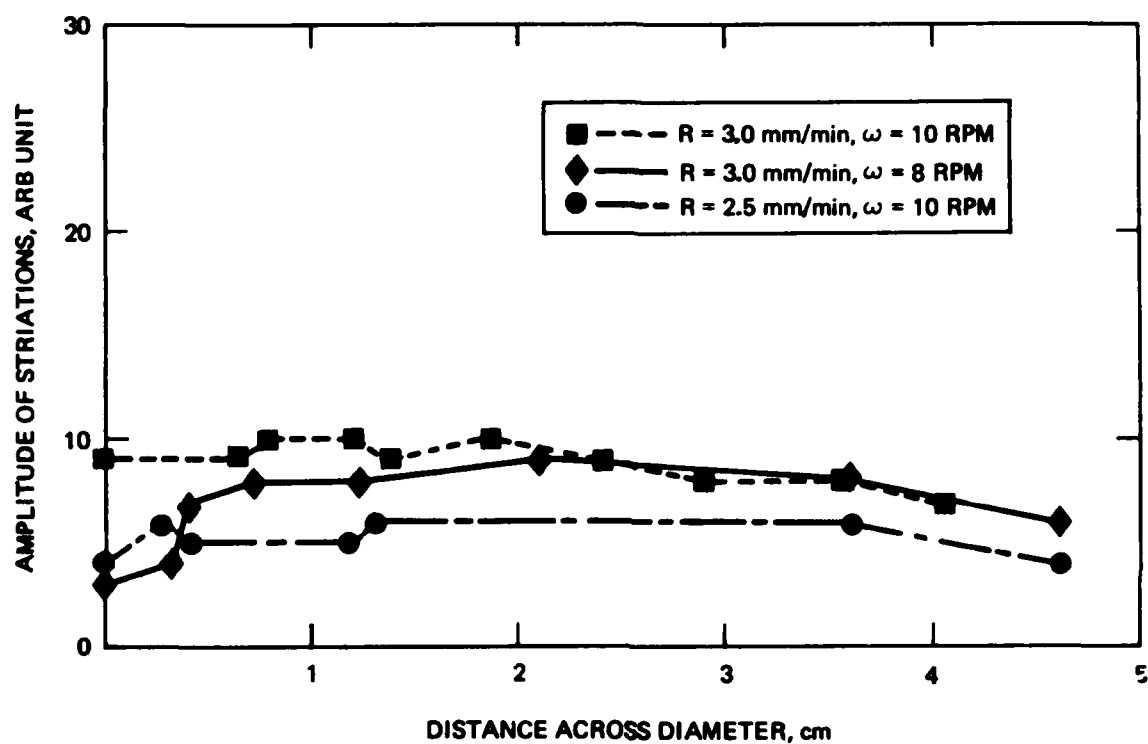
Figure 39.   Variations in amplitude of striations across a diameter
in Z180Ga.   Sections 4, 5, and 6.
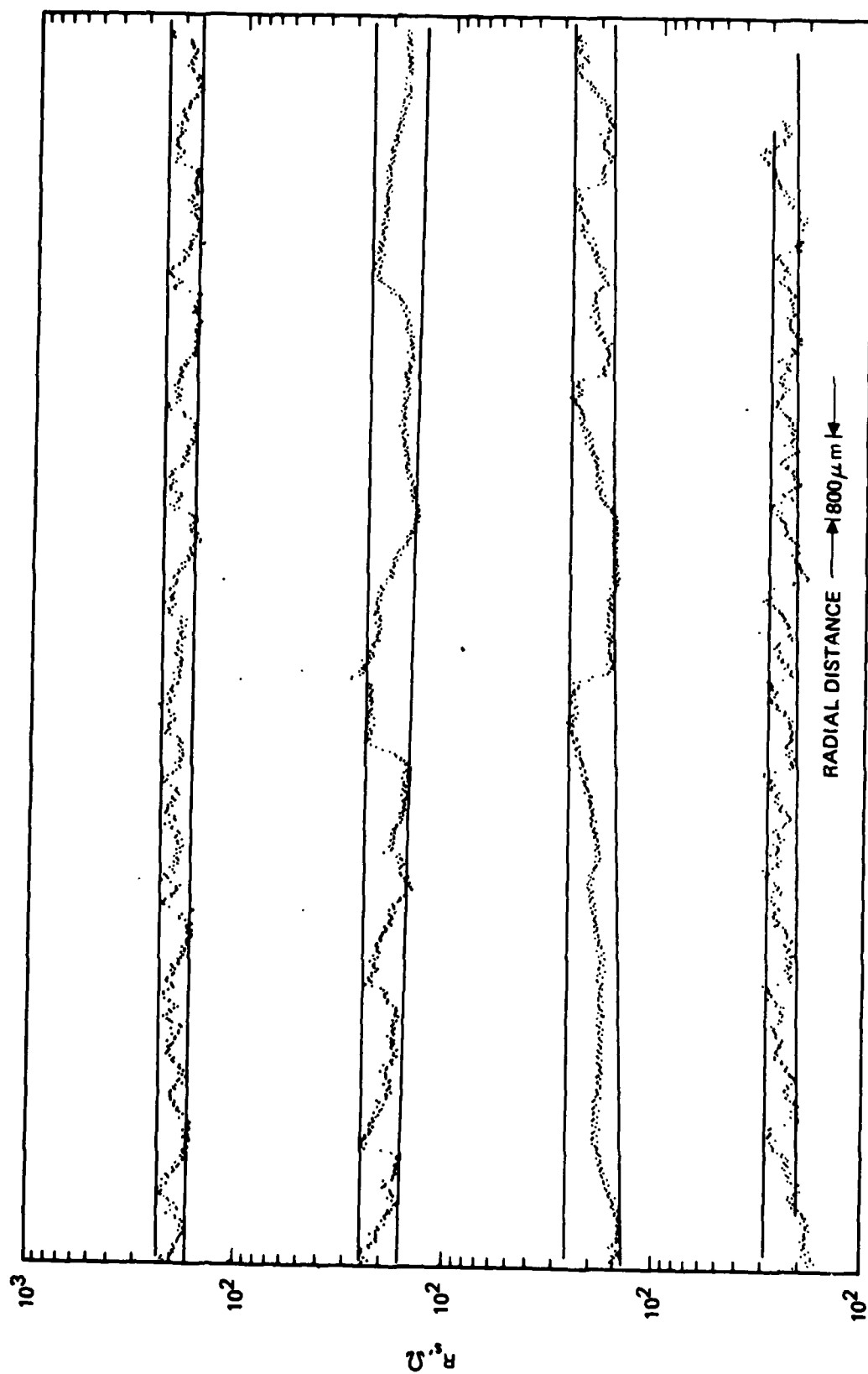
Figure 40. Spreading resistance profile for crystal Z180Ga (3mm/min, 8 rpm)

calculated value from the Cochran analysis by the constant destruction of the boundary layer. Hence, the thinner boundary layer probably more than offsets the increase in the microscopic growth rate arising from the backmelting process.

In crystal Z179Ga we examined the possibility of achieving compositional uniformity by exploring the opposite extreme. We maximized the growth rate and minimized the rotation rate.

At low frequencies of fluctuation, it can be shown from the BPS segregation theory that compositional variations due to growth rate fluctuations can be minimized by establishing growth conditions where $R\delta/D >> 1$.[20] These conditions are rarely tried because they are conducive to the undesired constitutional supercooling condition, which leads to cellular growth.

Examination of Z179Ga shows that the freezing interface is severely concave and that the striations are disrupted with the "feathering" morphological feature. The compositional fluctuations as revealed by the spreading resistance measurement are generally higher even at the extreme condition of a 6 mm/min growth rate and a 2 rpm rotation rate. It is possible, however, that higher growth rates, beyond the capability of our float-zone grower, may lead to an improvement in compositional uniformity and a lower swirl defect density.

To achieve the ultimate homogeneity, we may have to rely on a post-growth process, such as neutron transmutation doping,to maximize compensation uniformity. We have shown that compositional nonuniformity on a microscale can be homogenized by thermal diffusion at 1300°C. After 368 hr, the amplitude of rotational striations spaced by ∿300 μm were reduced by 64%. With a closer spacing between striations by growing the crystal at a faster rotation rate, a concomitant reduction in the diffusion time will be required.

---

[20] J.R. Carruthers and A.F. Witt, Transient Segregation Effects in Czochralski Growth, Bell Labs. Technical Memorandum TM 74-1522-6 (1974)

Contamination of the crystal by the impurities from the quartz ampoule during diffusion is a problem. The problem may be alleviated by providing a high-purity Si protective shield between a high-purity synthetic silica ampoule and the crystal.

C.   DISLOCATION ETCHING

Crystal Z180Ga was cut axially on a (110) plane, polished, and Wright etched[21] to reveal dislocations. The polished slab was cleaned in organic solvents using TCE, acetone, and methanol. After being dried in N_2, it was dipped in a 10:1 mixture of H_2O:HF. It was rinsed in DI H_2O and dried in N_2. The Wright etch was prepared by mixing:

> 60 ml conc. HF (49%)
>
> 30 ml conc. HNO_3
>
> 30 ml 5 molar solution of CrO_3 in H_2O
>
> 2 g $Cu(NO_3)_2 \cdot 3H_2O$ (reagent grade)
>
> 60 ml glacial acetic acid
>
> 60 ml DI H_2O .

The slab was etched for 15 min under constant agitation. There were no dislocation pits except near the tang end, where dislocations propagated from the sudden freeze-out of the melt. The remainder of the surface was sparsely populated with shallow saucer-shaped pits mostly along rotational striations. Figure 41, which was taken at 185x under Nomarski contrast, shows these pits.

The pits are due to swirl defects and are formed in a striated pattern on the seed side of rotational striations in accord with findings reported elsewhere.[22,23] Dopant striations are known to form during

---

[21] M.J. Wright, J. of Electrochem. Soc 124, 757-762 (1977)

[22] A. Murgai, H.C. Gatos, and W.A. Westdorp, J. Electrochem. Soc. 126, 2240-2245 (1979)

[23] T. Abe, K. Kikuchi and S. Shirai, "Semiconductor Silicon 1977" edited by H.R. Huff and E. Sirtl, p. 95, The Electrochemical Society Soft-bound Proceedings Series, Princeton, N.J. (1977).

185X

Figure 41.
Shallow swirl defect pits
along rotational striations.

deceleration of microscopic growth rate in systems where k < 1. The microscopic growth rate maxima and minima occur somewhat in advance of the corresponding concentration maxima and minima.[24] This behavior is attributed to the slow diffusion controlled redistribution of the solute at the interface.

The formation of swirl defects, however, coincides with microscopic growth rate maxima near carbon concentration maxima. It is generally accepted that the critical nuclei for swirl defect formation are related to carbon.[22]

A typical concentration of carbon in our float-zoned crystals is in the vicinity of 1×10^{16} cm^{-3}. The variation in carbon concentration may be estimated by using Eq. 3. Taking the distribution coefficient of carbon as 0.07,[25] the microscopic growth rate as 50 μm/sec, the diffusion boundary layer thickness as 650 μm, the rotation rate as 8 rpm, and diffusion coefficient as 5×10^{-5} cm^2/sec, the variation of concentration with growth rate, $(\Delta C/C)/(\Delta R/R)$, is 0.51. Assuming a 100% variation in microscopic growth rate, the variation in carbon concentration $\Delta C/C$ will be 51%. There were other areas in the slab where the defects were randomly distributed, which has been found to occur when fluctuations of carbon concentration are not pronounced.[22] More data are required before we can make a good correlation of the density and distribution of swirl defects with the growth parameters and interface shape.

---

[24] A. Murgai, H.C. Gatos, and A.F. Witt, J. of Electrochem. Soc. 123, 224 (1976)

[25] F.W. Voltmer and F.A. Padovani, "Semiconductor Silicon 1973" edited by H.R. Huff and R.R. Burgess, The Electrochemical Society Softbound Proceedings Series, Princeton, N.J. (1973)

SECTION 4

ADDENDUM

At the end of the scheduled performance period for this program, all
that remained to be completed of our original goal was to evaluate pro-
cessed wafers from crystal Z206Ga grown for this program and supplied to
our FPA fabrication facility. Wafers from this crystal have been neutron
transmutation counterdoped at three different concentration levels of
phosphorus and then processed into FLIR test chips using a mask set desig-
nated as CRC203. Delays in the transmutation and subsequent processing
procedures prevented our receiving samples of processed wafers until
September, 1981. Section 4A in this addendum reports the results of our
evaluation of the processed detector material. A no-cost extension was
requested and granted to permit the completion of this task.

We have subsequently found that certain sections of LADIR crystal
Z206Ga have atypically high dislocation densities. This crystal does not,
therefore, represent our best material. However, two later crystals,
Z207Ga grown for the FTD FLIR program, and Z236Ga grown for detector
array programs requiring lower photon backgrounds, show excellent crystal
quality. These two crystals were grown using the technology developed
in the LADIR materials program. As a matter of interest, therefore, we
have included in Section 4A a description of both of these 2 in. diameter
Si:Ga crystals grown after the end of this program. We include this data
to illustrate that the experience and knowledge obtained in this LADIR
materials program has been utilized repeatedly to produce improved Si:Ga
for detector array applications.

In addition to the no-cost extension, additional funding in the form
of an "add-on" to the LADIR contract covering the period November 15, 1980
to September 1, 1981 has allowed us to investigate in detail the material
properties of tested Si:Ga FLIR chips. Crystal evaluation samples are
generally taken only from the two ends of the crystal — seed and tang.
FLIR chips fabricated from wafers cut at a considerable distance from

95

either seed or tang end may differ in doping parameter properties from the evaluation slices. In addition, array processing procedures have sometimes been observed to alter the impurity content from the "as-grown" condition. To assure ourselves that we determine the material parameters of fabricated chips accurately, we must make Hall effect samples from those very chips. This is what we have done in the LADIR materials "add-on" program. Accurate determination of doping parameters, along with the development of a greatly improved detector model, have allowed us to correlate observed detector performance with Si:Ga material properties. This correlation is considerably better than any we have been able to achieve previously and provides a basis for further development of detector modeling to permit tailoring of Si:Ga material properties for specific operating conditions for a wide range of applications. Section 4B describes our results in this "add-on" effort.

A.   EVALUATION OF CRYSTALS FOR FOCAL PLANE ARRAYS

Slices from the crystal grown for the LADIR Materials program (Z206Ga) were delivered to Carlsbad Research Center (CRC) for use in FLIR detector array fabrication. The crystal was grown with boron and donor concentrations as low as possible with the desired phosphorus compensation to be subsequently added by transmutation. Some chips were processed from the material "as grown" even though initial Hall effect versus temperature measurements indicated that the crystal was slightly boron-dominated. Other slices of this crystal were sent to Texas A & M University Nuclear Science Center for addition of phosphorus by neutron transmutation doping at concentration levels of 1, 2, and 4×10^{13} P atoms/cm^3. FLIR chip arrays were then fabricated on these transmuted wafers at CRC. Our carrier concentration and Hall mobility data for transmuted samples of Z206Ga are shown in Figures 42-47. A line is drawn through data in the "half-slope" ($p \gg N_D - N_B$) and "full-slope" ($p \ll N_D - N_B$) regimes in two of the hole concentration versus 1000/T plots (Figures 42 and 44). The intersection of these two lines indicates,

96
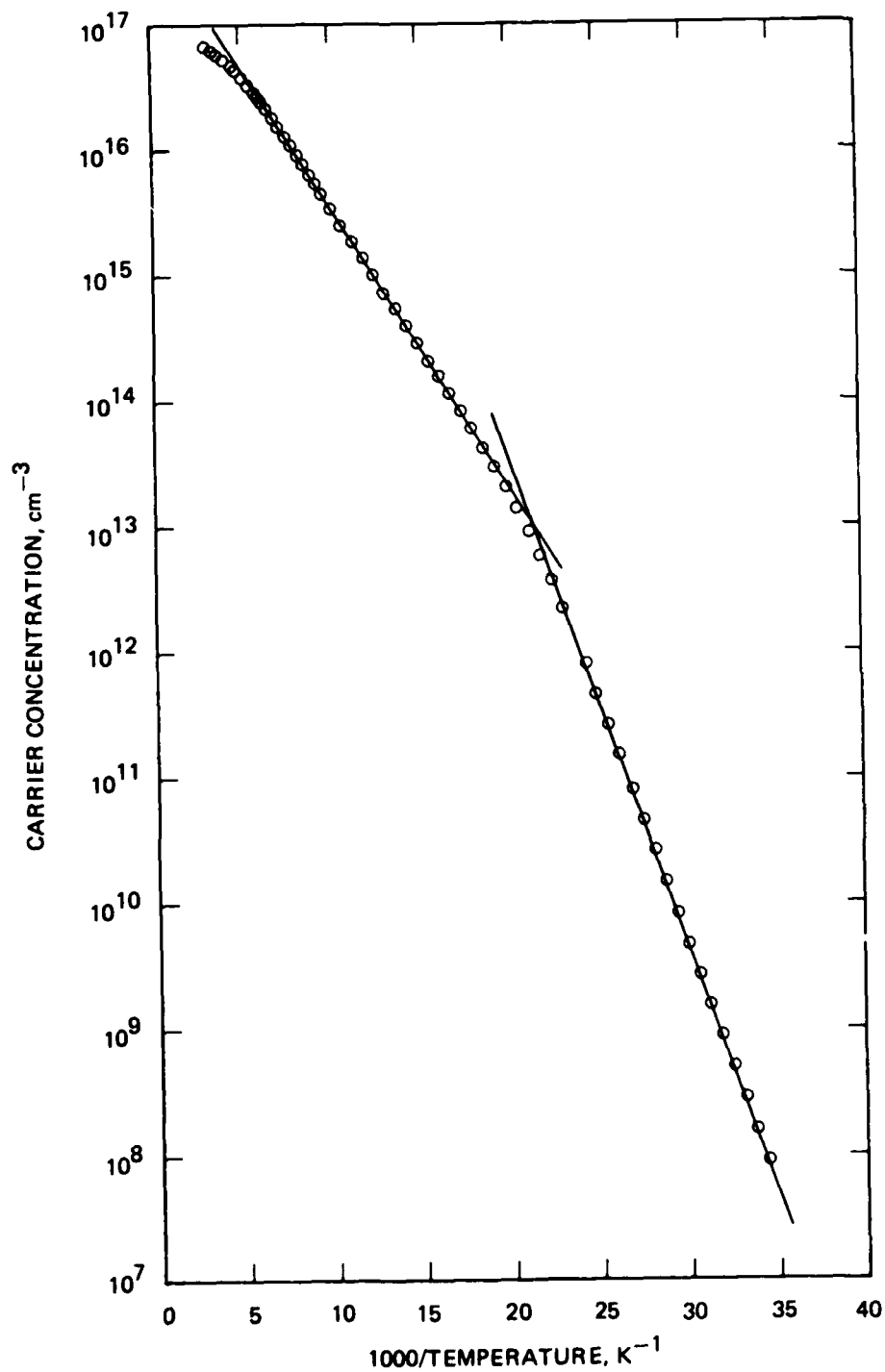
Figure 42. Hole concentration vs 1000/T for transmuted
sample Z206Ga.11. A concentration of
1×10^{13} P/cm^3 was added by neutron
transmutation doping.

Figure 43. Hall mobility vs temperature for transmuted sample Z206Ga.11. A concentration of 1×10^{13} P/cm^3 was added by neutron transmutation doping.
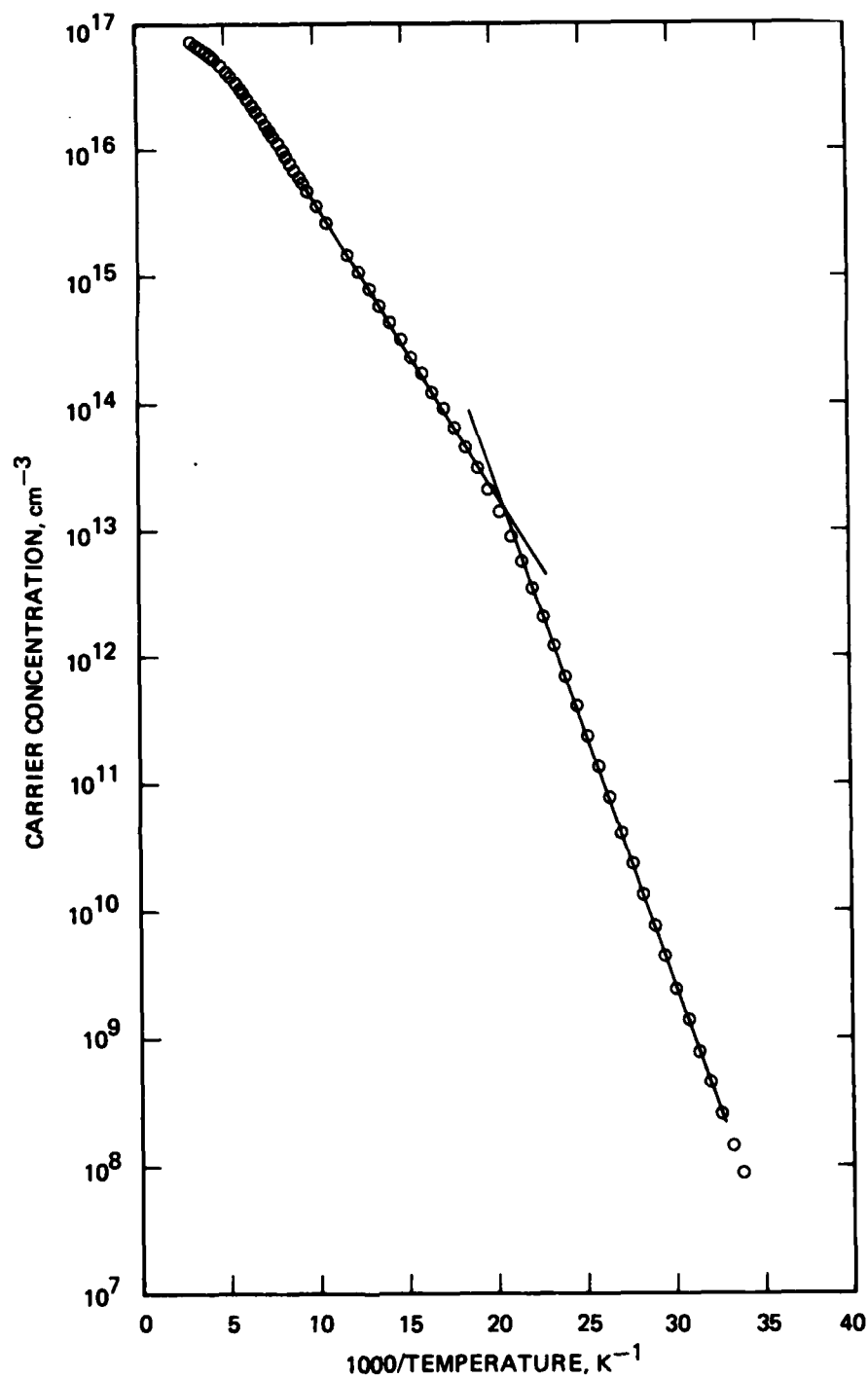
Figure 44. Hole concentration vs 1000/T for transmuted
sample 2206Ga 25. A concentration of
2×10^{13} P/cm^3 was added by neutron
transmutation doping.

99

Figure 45. Hall mobility vs temperature for transmuted sample
Z206Ga.25. A concentration of 2×10^{13} P/cm^3 was
added by neutron transmutation doping.

100
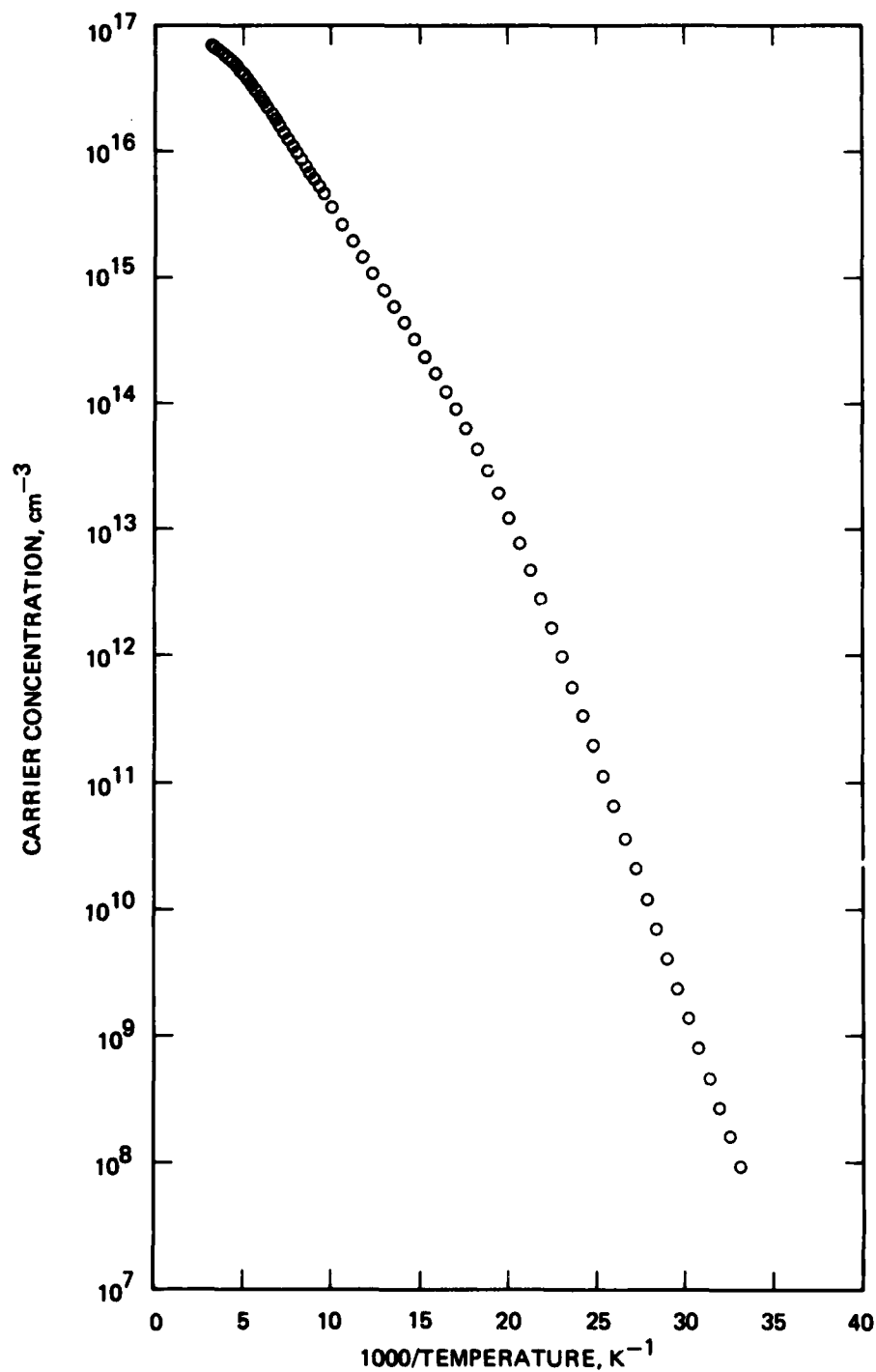
Figure 46. Hole concentration vs 1000/T for transmuted
sample 2206Ga 43. A concentration of
4×10^{13} P/cm^3 was added by neutron
transmutation doping.

101

MOBILITY, cm^2/V– sec

10^4

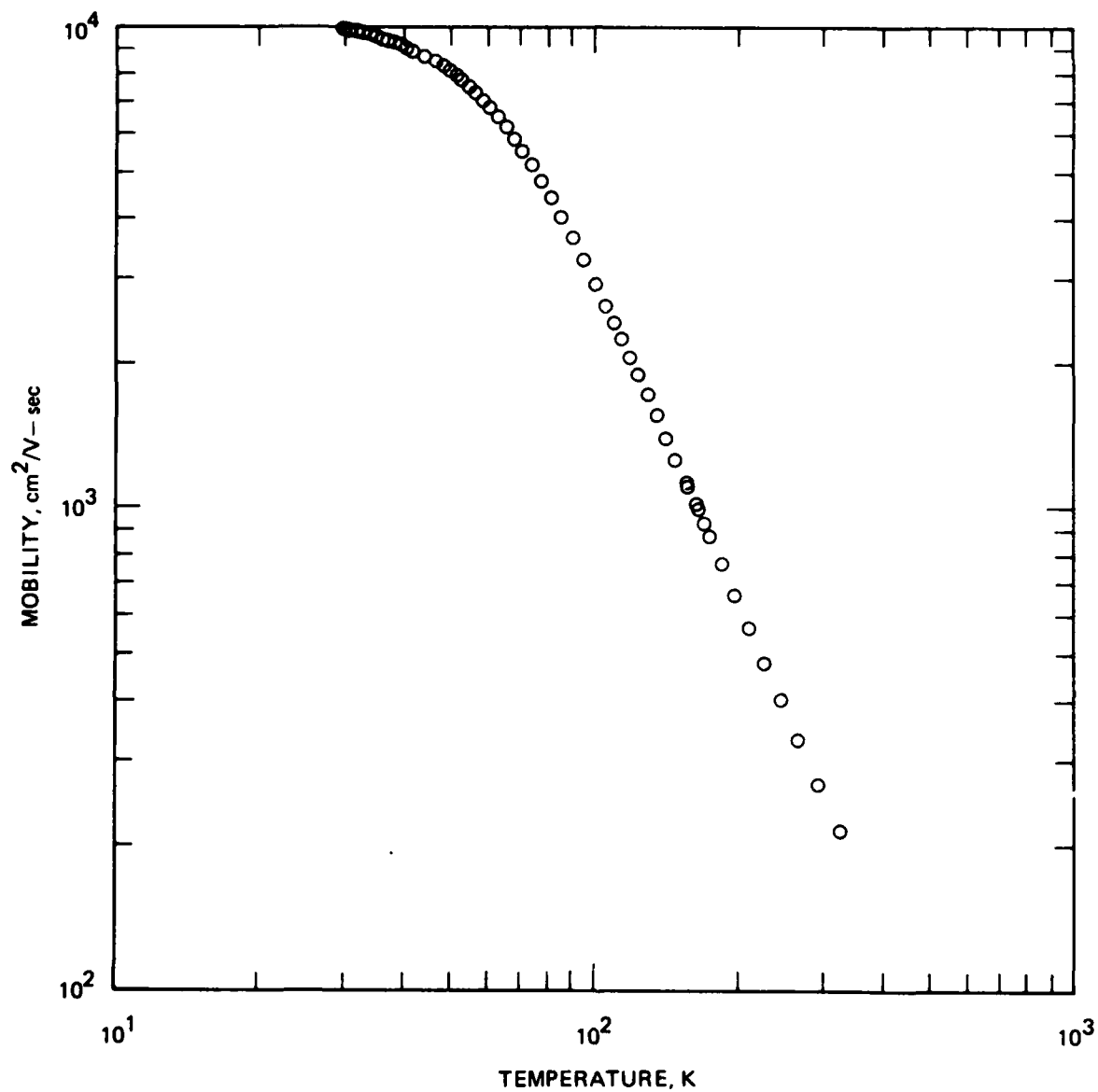10^3

10^2

10^1 10^2 10^3
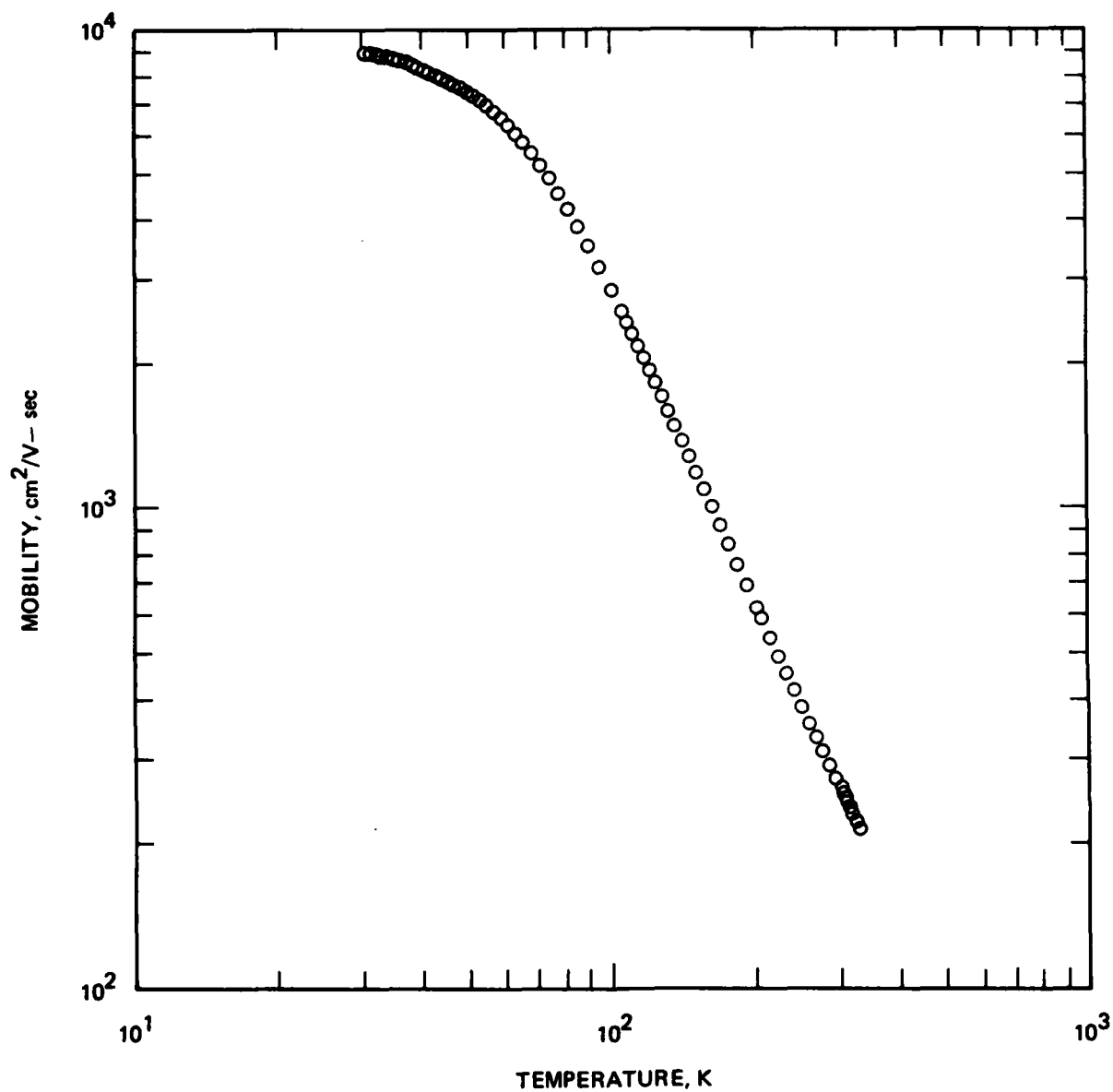
TEMPERATURE, K

Figure 47.   Hall mobility vs temperature for transmuted sample Z206Ga.43. A concentration of 4 x 10^{13} P/cm^3 was added by neutron transmutation doping.
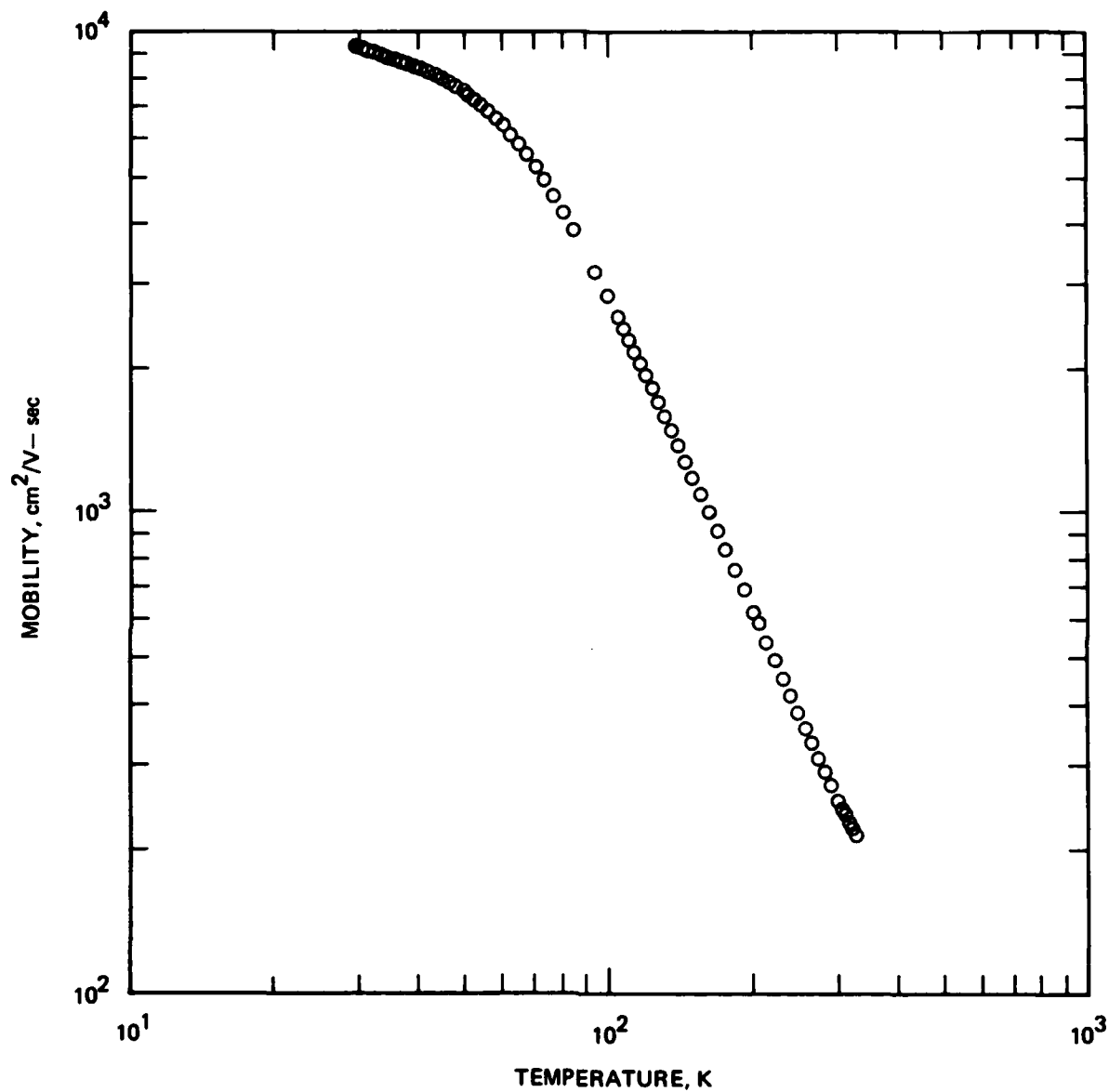
102

approximately, the net compensating donor concentration in the sample. A computer nonlinear least squares fit of the full set of data was done for each of the samples to provide the data given in Table 2, which summarizes these analysis results on Z206Ga "as grown" and on samples that had been processed into FLIR detector array chips (CRC 203) after neutron transmutation. The correlation between the expected total phosphorus concentration after transmutation and the observed donor concentration is excellent.

The Hall mobility versus temperature curves (Figures 43, 45, and 47) for the three transmuted samples also reflect the degree of compensation. The low temperature mobility is limited largely by neutral impurity scattering, which depends only upon the Ga doping concentration. However, ionized impurity scattering due to compensating donors does modify the observed mobility slightly in this doping range. A slight decrease in low temperature (30K) mobility is observable with increasing neutron transmutation-produced donor concentration. The Ga doping in the three samples is very similar, although Z206Ga.11, with the lowest donor concentration and highest mobility, also has a somewhat lower Ga concentration than the other two.

We observed a problem with the CRC 203 FLIR array chip samples in the course of this study. There was not a degenerate p^+ contact layer on the IR radiation receiving surface of the samples. We had to provide a p^+ contact in four corners of the van der Pauw Hall sample in order to make low temperature measurements. The boron-implanted p^+ layer made during device processing was evidently not sufficiently doped or was removed in subsequent processing such as during oxide removal or metalization on some wafers. Very little FPA testing of Z206Ga CRC203 chips has been done because the FTD program which was supporting the work ended before this particular lot could be fully evaluated.

Table 2. Results of Analysis of Hall Effect Measurements on Si:Ga
Crystal Z206Ga. The table includes "as grown" results
and measurements on neutron transmutation-doped samples,
with transmutation-added phosphorus at three different
concentration levels, the values of which are shown in
the "Sample Description" column.

Sample Description	N_{Ga}	N_{Donor}	N_{Boron}
Seed (as grown)	$\sim 7.7 \times 10^{16}$	3×10^{12}	5×10^{12}
Tang (as grown)	$\sim 7.7 \times 10^{16}$	$3\text{-}4 \times 10^{12}$	3×10^{12}
.11 (10^{13} P/cm^3 added)	$7\text{-}7.2 \times 10^{16}$	1.5×10^{13}	4×10^{12}
.25 (2×10^{13} P/cm^3 added)	$7.4\text{-}7.9 \times 10^{16}$	2.4×10^{13}	3.6×10^{12}
.43 (4×10^{13} P/cm^3 added)	$7.5\text{-}7.9 \times 10^{16}$	$4.0\text{-}4.6 \times 10^{13}$†	

†result represents ($N_{Donor} - N_{Boron}$) concentration: N_B cannot be
determined separately in this sample.

Using the techniques developed in our LADIR materials work, we have
subsequently grown two 2 in. diameter Si:Ga crystals. One of these (for
the FTD program–Z207Ga) was targeted to contain 5×10^{16} to 1×10^{17}
Ga/cm^3, and the desired concentration range was indeed obtained. At the
time that this crystal was grown, the optimum doping for the FTD program
had not been established, but it was expected to be something greater
than 5×10^{16} Ga/cm^3. FLIR chips using the mask set designated CRC 163
were fabricated from Z207Ga. Our results from characterization of seed
and tang slices of "as-grown" samples of Z207Ga, along with evaluation
of a processed Z207Ga CRC 163 chip are presented later in Section 4B
(see Table 3).

The CRC 163 chip was sufficiently doped with Ga to allow us to
observe impurity band conduction in Hall effect–resistivity measurements
on the processed chip material. The implication of this conduction
mechanism in modeling the detector performance is discussed further in
Section 4B.

104

Another crystal, Z236Ga, was grown for "lower photon background" applications ($Q_B < 10^{15}$ ph/cm^2-sec). The results from Hall effect evaluation of this crystal are shown below. Wafers from this crystal have been sent for neutron transmutation at levels of 1 and 2×10^{13} P/cm^3, but no detector samples have yet been fabricated.

Sample	N_{Ga}, cm^{-3}	N_{Donor}, cm^{-3}	N_{Boron}, cm^{-3}
Z236A (seed)	4×10^{16}	$4-6 \times 10^{12}$	4×10^{12}
Z236T (tang)	4×10^{16}	$6-10 \times 10^{12}$	$3-4 \times 10^{12}$

The uniformity of the Ga distribution in these two crystals is very good in the center regions, as can be seen in Figure 48 and 49 which show spreading resistance across polished wafers from each crystal. Both crystals were grown at a rotation rate of 10 rpm and a growth rate of 3-4 mm/min. The poor crystalline quality found in most of the Z206 Ga confirms our earlier observations that growth below a rate of 3 mm/min is not practical.

B. FLIR MATERIAL — DETECTOR DIAGNOSTICS

1. Detector Modeling and Experimental Verification

In the FLIR programs at HAC, there have been some outstanding successes in producing detector arrays with excellent detector properties and imaging quality. However, the underlying reasons for these successes, as well as many of the failures, are not well understood. In particular, the extent to which Si:Ga material properties (N_{Ga}, N_{Donor}, N_{Boron}) control the experimentally observed detector behavior in array chips has been unclear. In cooperation with LADIR-FTD program personnel in HAC Division 72, therefore, we have carried out a project to directly study the impact of Si:Ga material parameters on the performance of completely processed detector array-imaging chips.
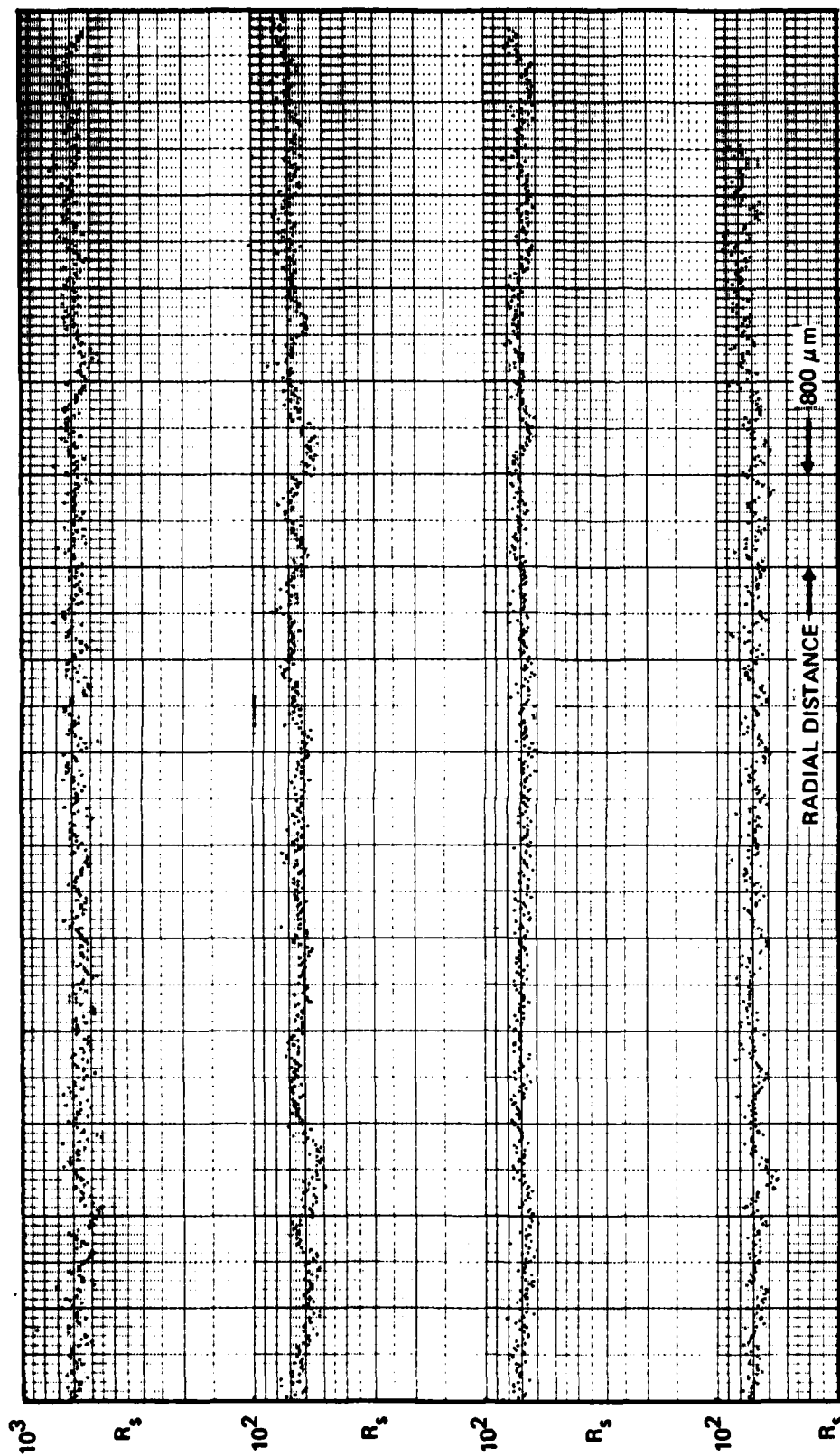
Figure 48. Spreading resistance for the seed end of Crystal Z207Ga. The Ga doping uniformity of the central region of this crystal is shown by the absence of fluctuations in the spreading resistance.

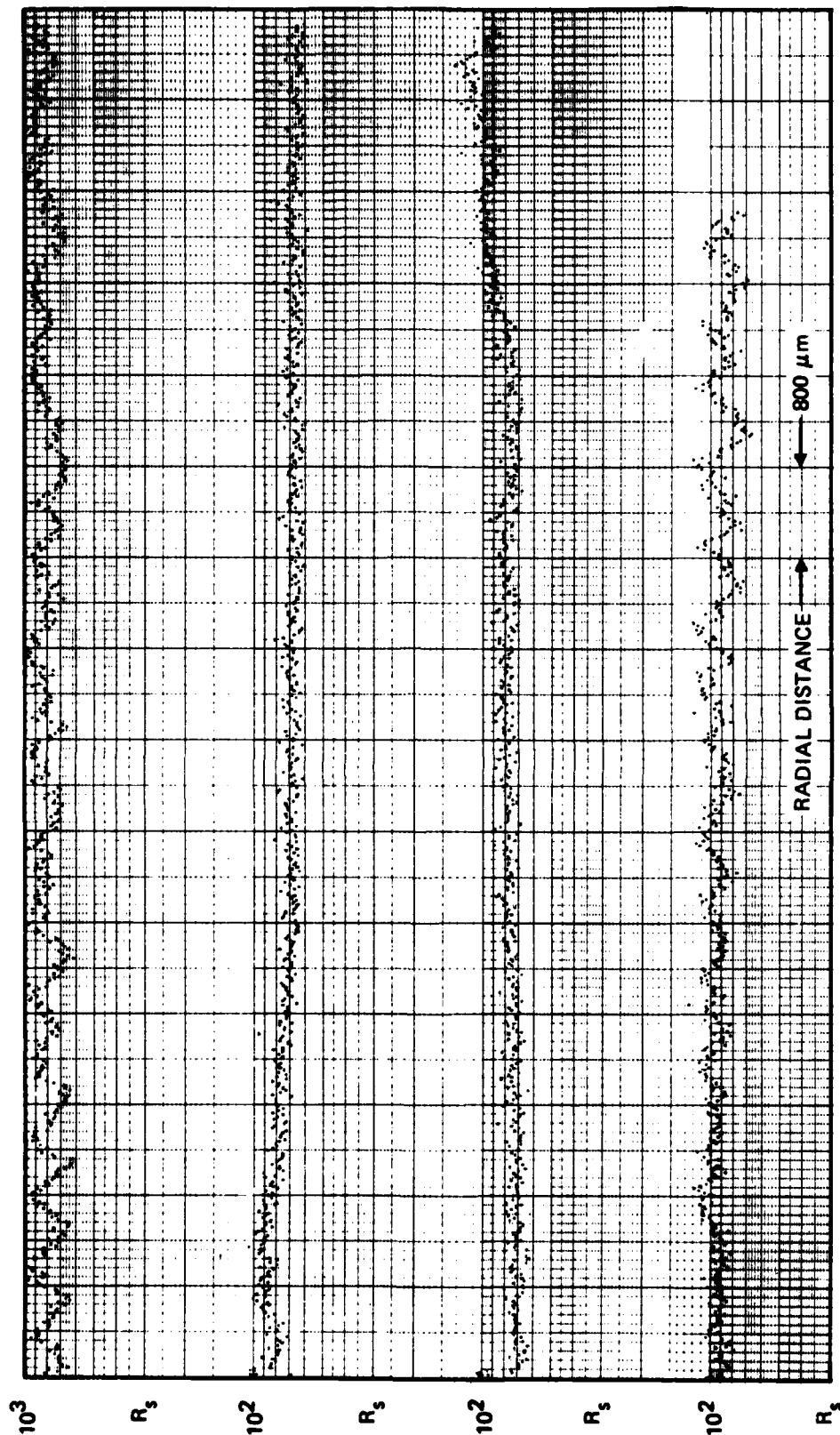Figure 49. Spreading resistance for the tang end of Crystal Z236Ga. The doping level of this crystal is 4×10^{16} Ga atoms/cm^3 and is very uniform in the central region as indicated by the absence of fluctuations in spreading resistance.

Hybrid-type chips from a number of different process lots using wafers from several different Si:Ga ingots were selected after testing at HAC Division 72 for imaging quality and detector performance. To carry out this study, the detector substrate was carefully separated from the signal processing circuitry chip and a number of discrete samples were cut from the Si:Ga substrate. In preparing discrete samples, care was taken not to do any further high temperature processing on the material that might alter the doping from that in the original array. One of the discrete samples from each chip became a Hall effect sample; one was used to evaluate the electrical properties of the p^+ layer used to contact the infrared energy receiving surface of the Si:Ga detector array; the remainder of the chip was reserved for discrete detector evaluation by Division 72. The measurements on the Hall effect sample allowed us to determine the concentration of Ga, donors, and boron in the detector material. We made contact to the van der Pauw Hall sample through four corners of the original p^+ "contact" area, with all other p^+ regions etched away. We evaluated the electrical quality of the original p^+ contacting areas on another sample by making a van der Pauw sample without etching away the p^+ region. The heavily doped contact region dominates the electrical measurements at low temperatures where the Si:Ga substrate has "frozen out." Sheet resistance measurements of the implanted contact could thus be made down to liquid helium temperature. Detector structures cut from the rest of the original chip substrate were mounted up for testing at Division 72.

Table 3 lists the results from analysis of measurements of Hall effect versus temperature to determine N_{Ga}, N_{Donor}, and N_{Boron} for samples of the seven different crystals and eleven processed chips included in this study. Analysis results from evaluation slices taken from the original (unprocessed) material are shown, along with results from the detector substrate of CRC (Carlsbad Research Center) processed FLIR chips. In three of the eleven processed chips, an appreciable concentration of donors appears to have been added during processing

108

(Z20401Ga–CRC156; Z092Ga–CRC163; C4202Ga–CRC142). However, in none of
the chips is compensating donor concentration so high as to be expected
to seriously degrade detector operation for most FLIR applications. For
some systems applications requiring lower backgrounds or higher fre-
quency response, the compensation level, which is inversely proportional
to majority carrier lifetime, may have to be reduced to provide the
desired frequency response. Samples representing a wide range of Ga
doping ($2 \times 10^{16} - 2 \times 10^{17}$ Ga/cm^3) are included in this study to fully
explore the dependence of measured detector properties (particularly
quantum efficiency) on doping. As indicated in the results presented
in Table 3, residual boron is typically mid-10^{12} to low-10^{13} B/cm^3 in
our detector-grade Si:Ga material.

Discrete detectors from the four CRC163 chips listed in Table 3
were successfully characterized in testing at HAC Division 72.
Problems with the remaining remounted discrete detectors prevented
their being fully tested. In particular, the CRC142 chips all appeared
to have an insufficiently doped p$^+$ contact on one side. Hall effect-
resistivity data taken on the four CRC163 chip samples are shown
in Figures 50-57. The hole concentration versus 1000/T and mobility
versus temperature are shown for each. The temperature-dependent hole
concentration data was analyzed by fitting the data to the charge balance
equation using a non-linear least squares computer routine in order to
obtain the impurity concentrations listed in Table 3. The FLIR chip
fabricated from Z207Ga clearly shows the effect of impurity band con-
duction at low temperature. This is observed as an apparent increase in
measured hole concentration (Figure 56) and a dramatic drop in measured
mobility (Figure 57). Observation of this phenomena in Z207Ga–CRC163
will be more fully discussed in the next sub-section.

Before testing the working discrete detectors, which included the
four CRC163 chips in Table 3, along with a CRC163 chip from Z20401Ga
with doping parameters known approximately, the theoretically predicted
quantum efficiency (η_L) and D^*_{Blip} were calculated. The results of the
theoretical modeling of longitudinal extrinsic Si photodetectors done
by Dr. R. Baron at HRL, and later published in collaboration with

109

Table 3

Hall effect analysis of original material and processed chips. The CRC number indicates the mask design designation assigned by Carlsbad Research Center. The location of the original evaluation slices is indicated in parentheses under "Sample."

Sample	N_{Ga}, x 10^{16}	N_{Donor}, x 10^{13}	N_{Boron}, x 10^{12}
Z20104Ga (seed)*	10	7.2	6
(tang)*	7	7.2	$\sim$2
CRC 147*	10	7	$\sim$6
CRC 142*	9	6.9	14
CRC 163+	8	1.5	3
Z20401Ga (seed)	2.6	0.64	4.5
(tang)	3.0	0.90	6.0
CRC 156	2.9	2.6	$\sim$4
Z092Ga (transmuted section)	6.0	2.8	$\sim$5
CRC 156	6.5	2.2	$\sim$2
CRC 142	5.8	2 (a)	–
CRC 163	$\sim$7.2	$\sim$5.5 (a)	–
Z096Ga (seed)	2.0	2 (a)	–
(middle)	2.1	1.8	5.1
(tang)	2.7	1.1	3.4
CRC 163	2.0	1.4	16
Z097Ga (seed)	3.9	0.93	6.2
(middle)	4.3	2.3	12
CRC 142	3.6	1.6	4.6
Z207Ga (seed)	5.4	0.82	10
(tang)	16	4.1	18
CRC 163	$\sim$20	3	20
C4202Ga(b) (seed)	3	1.5 (a)	–
(middle)	4	1.3	4.6
CRC 142	4	5.1	11

* from neutron transmuted section with 5 x 10^{13} P/cm^3 added

+ from section not neutron transmuted

(a) number represents $N_D - N_B$; N_B could not be determined separately in this sample

(b) Czochralski grown crystal; all others are grown by the float-zone method

110

Figure 50.   Hole concentration vs 1000/T for
Z096Ga-CRC163 chip.

Figure 51. Hall mobility vs temperature for Z096Ga–CRC163 chip.

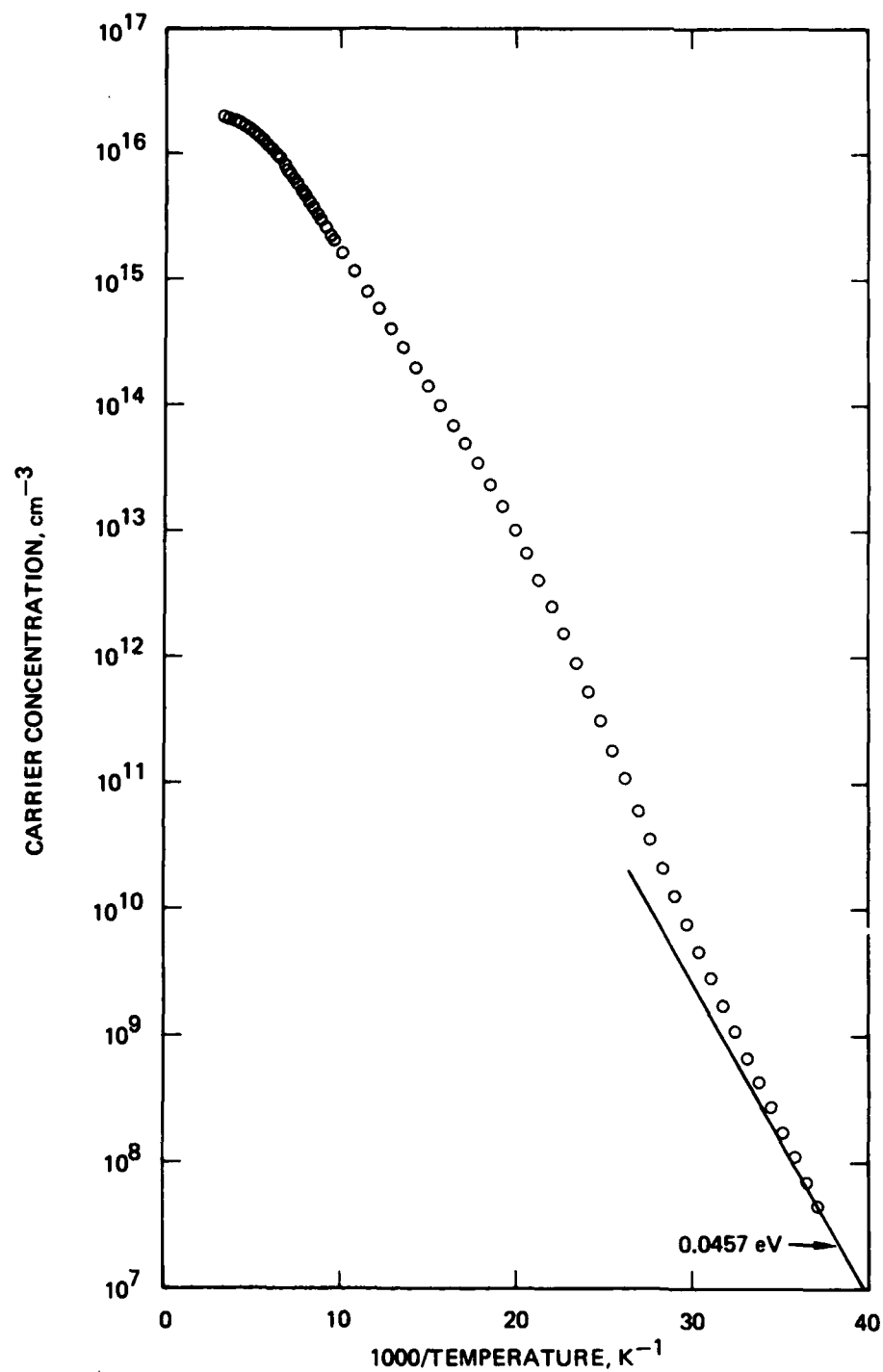Figure 52. Hole concentration vs 1000/T for
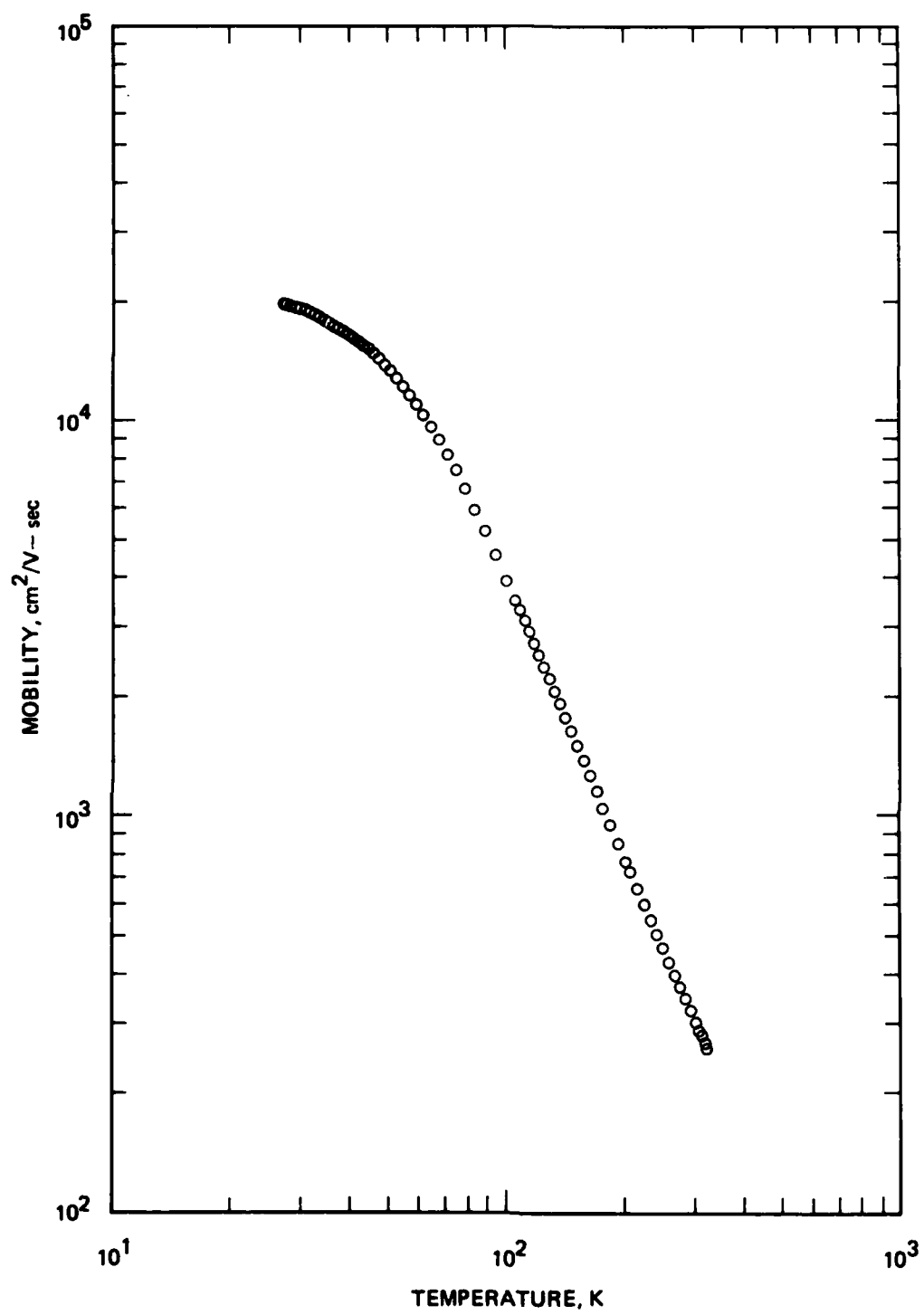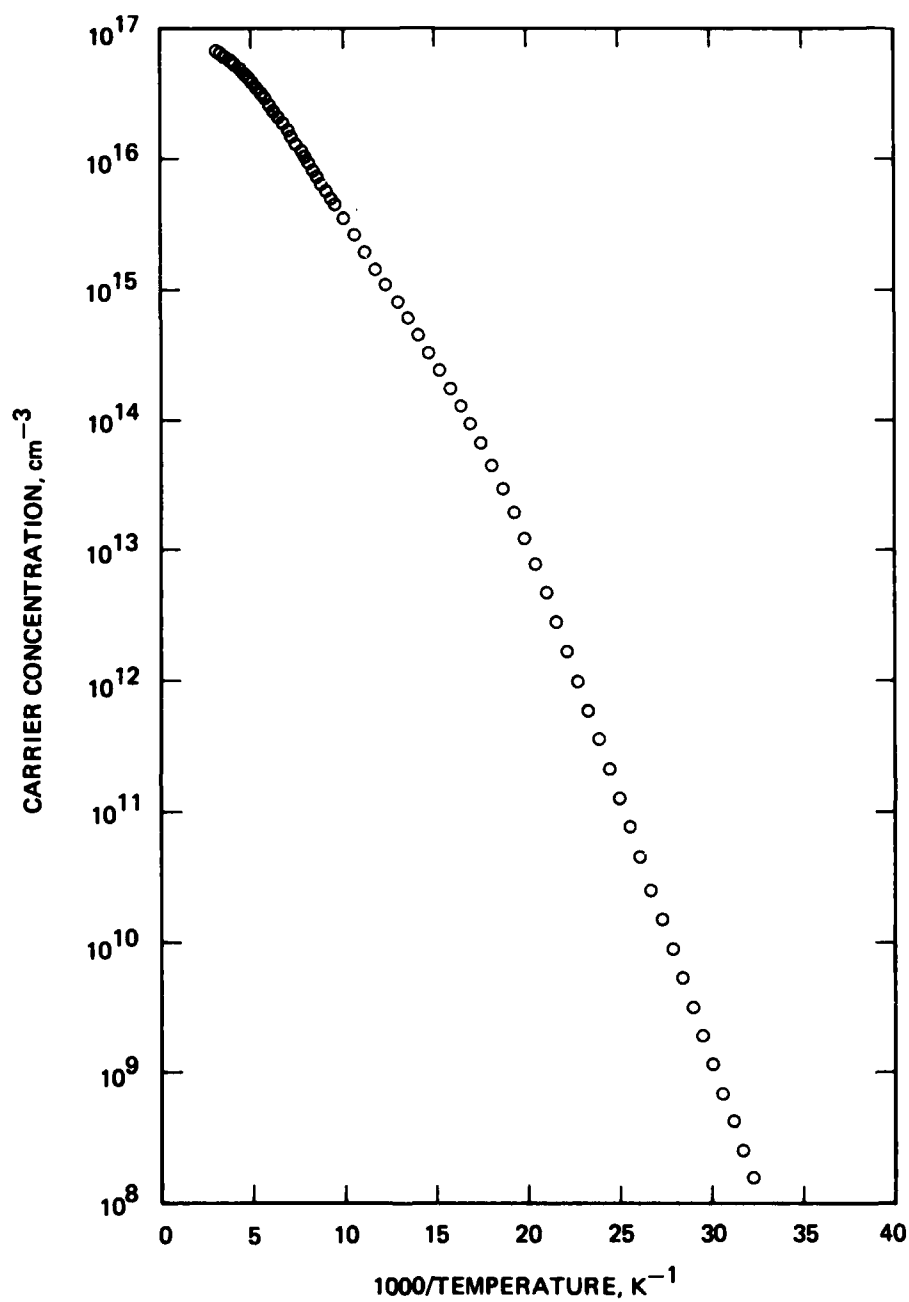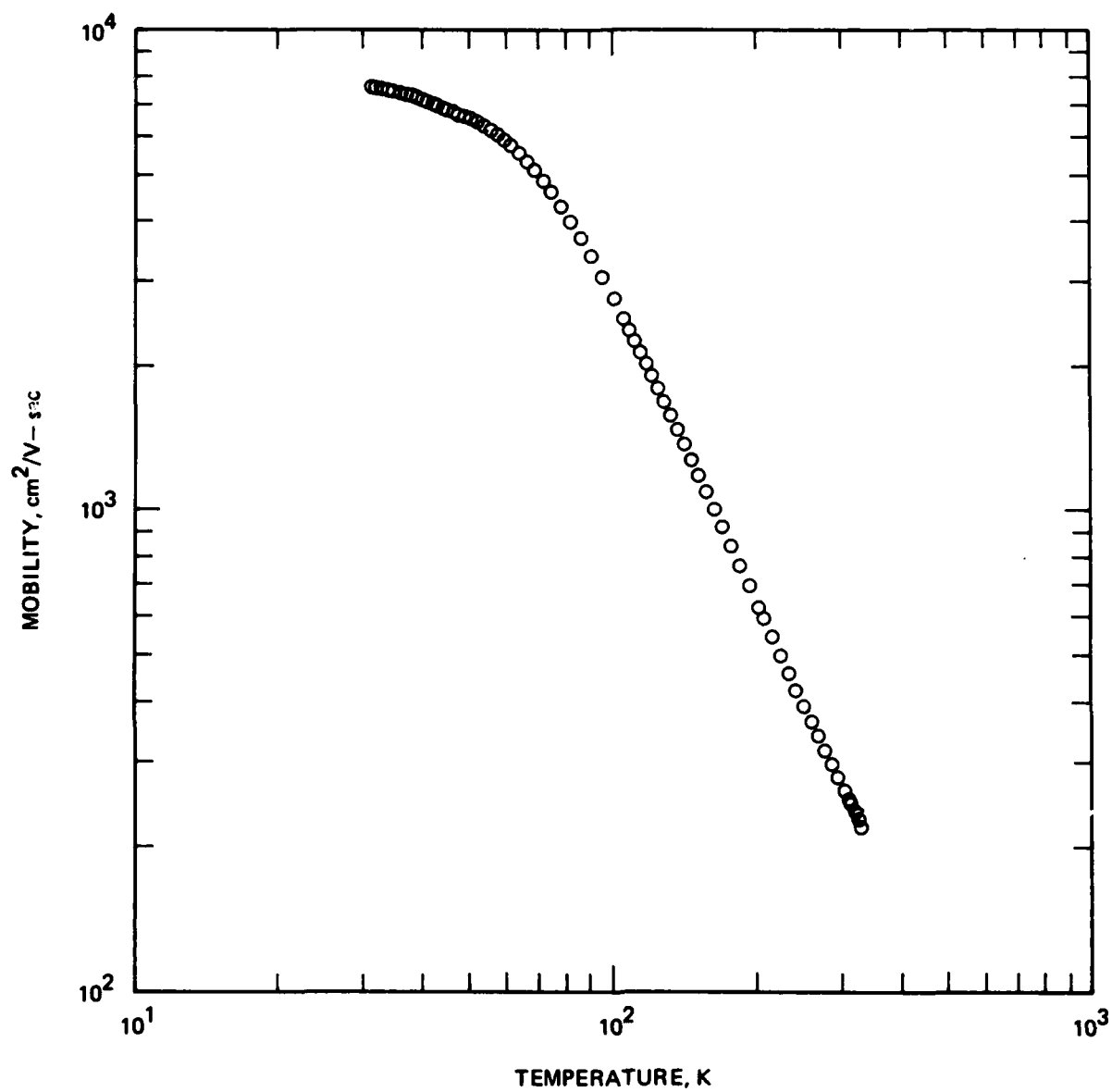Z092Ga-CRC163 chip.

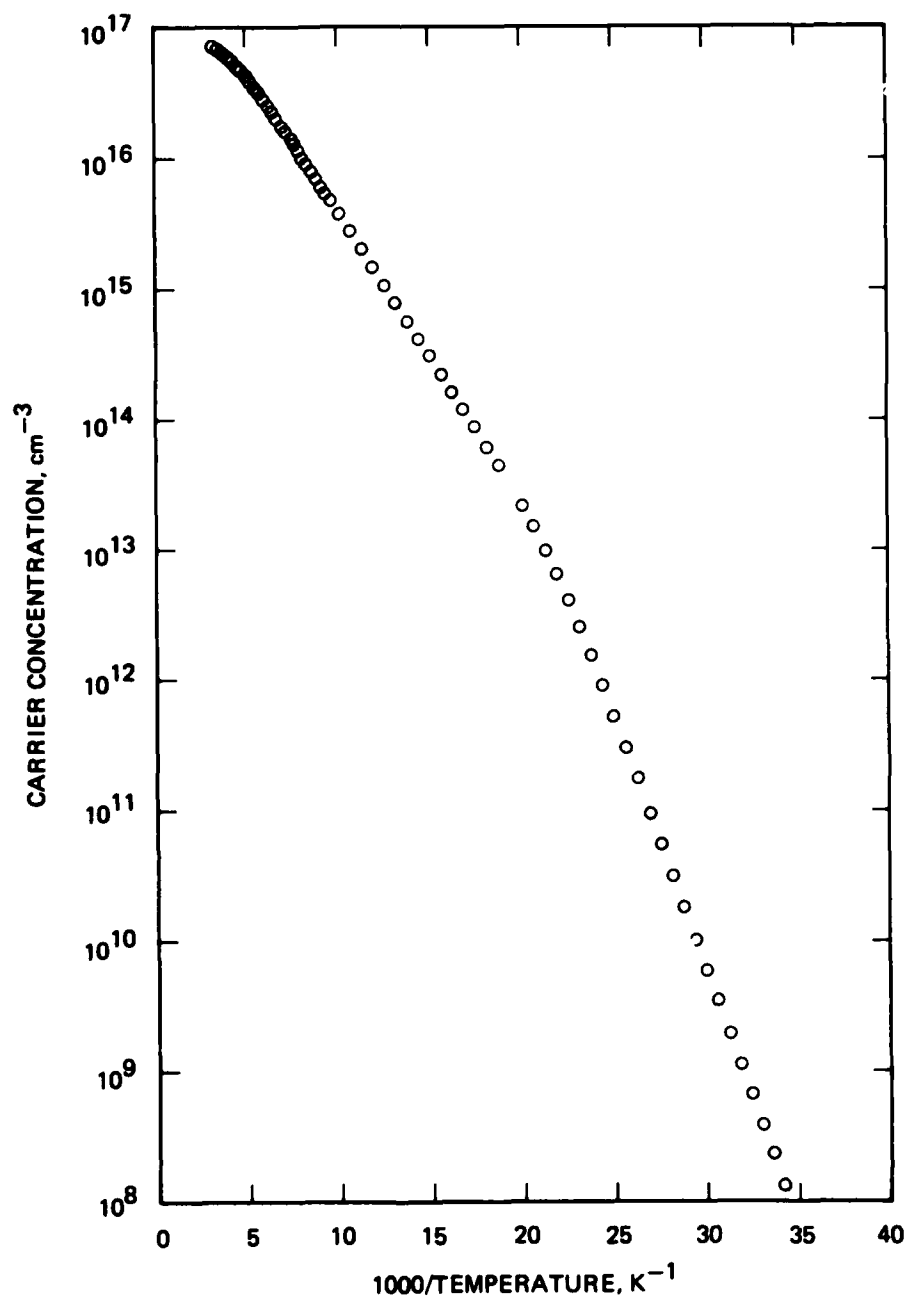Figure 53. Hall mobility vs temperature for Z092Ga-CRC163 chip.

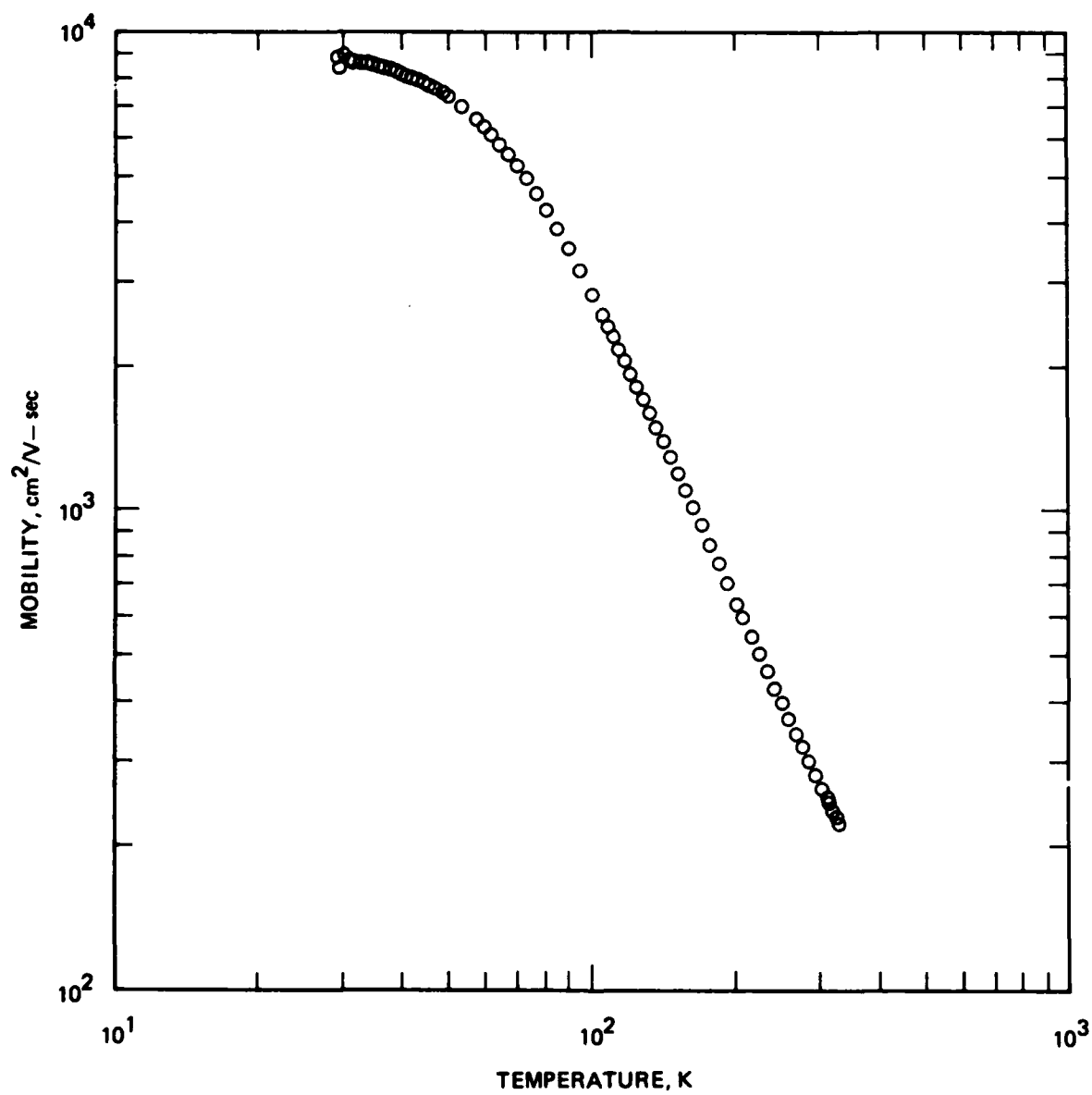Figure 54. Hole concentration vs 1000/T for
Z20104Ga-CRC163 chip.

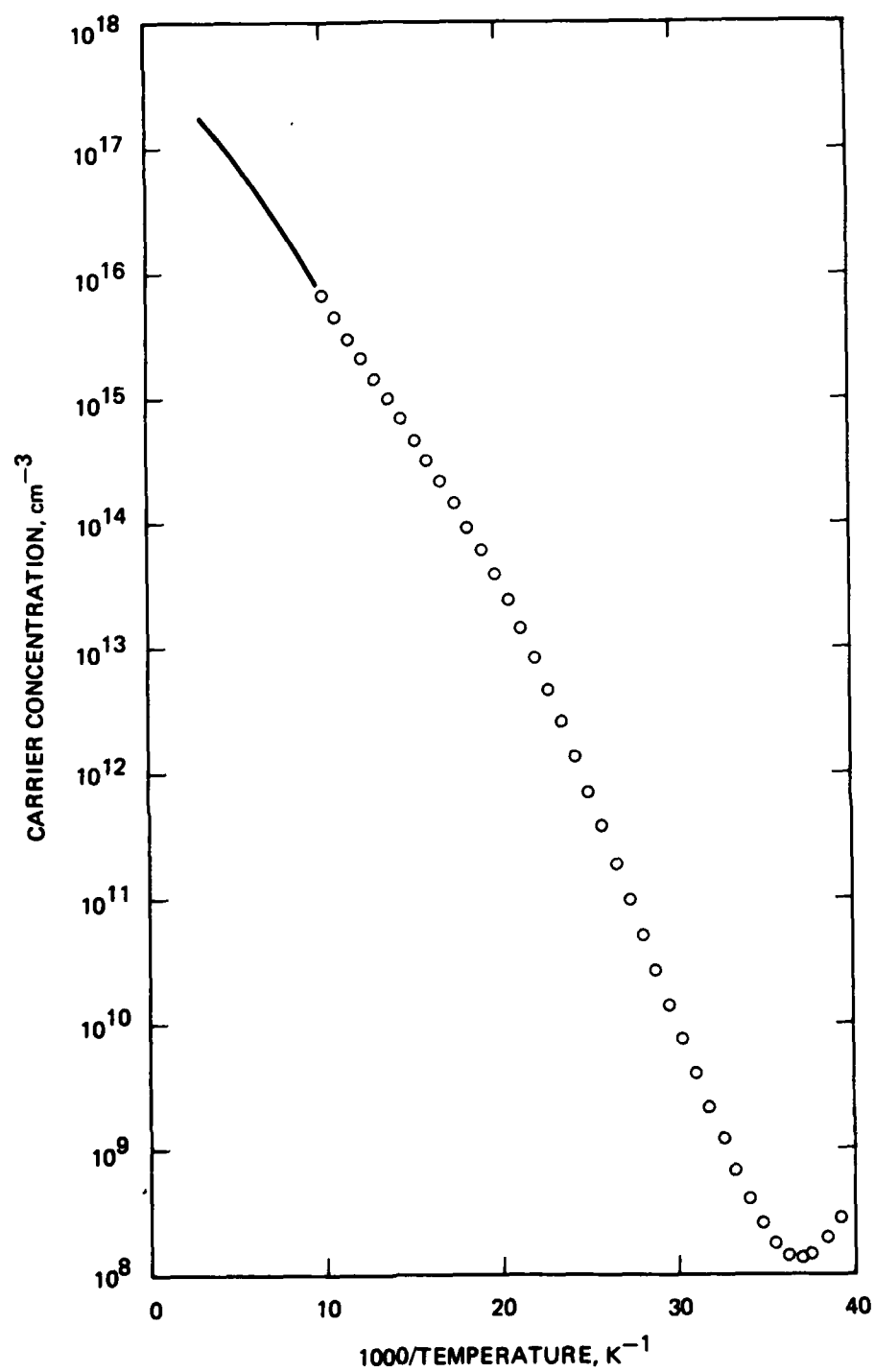Figure 55.   Hall mobility vs temperature for Z20104Ga-CRC163 chip.

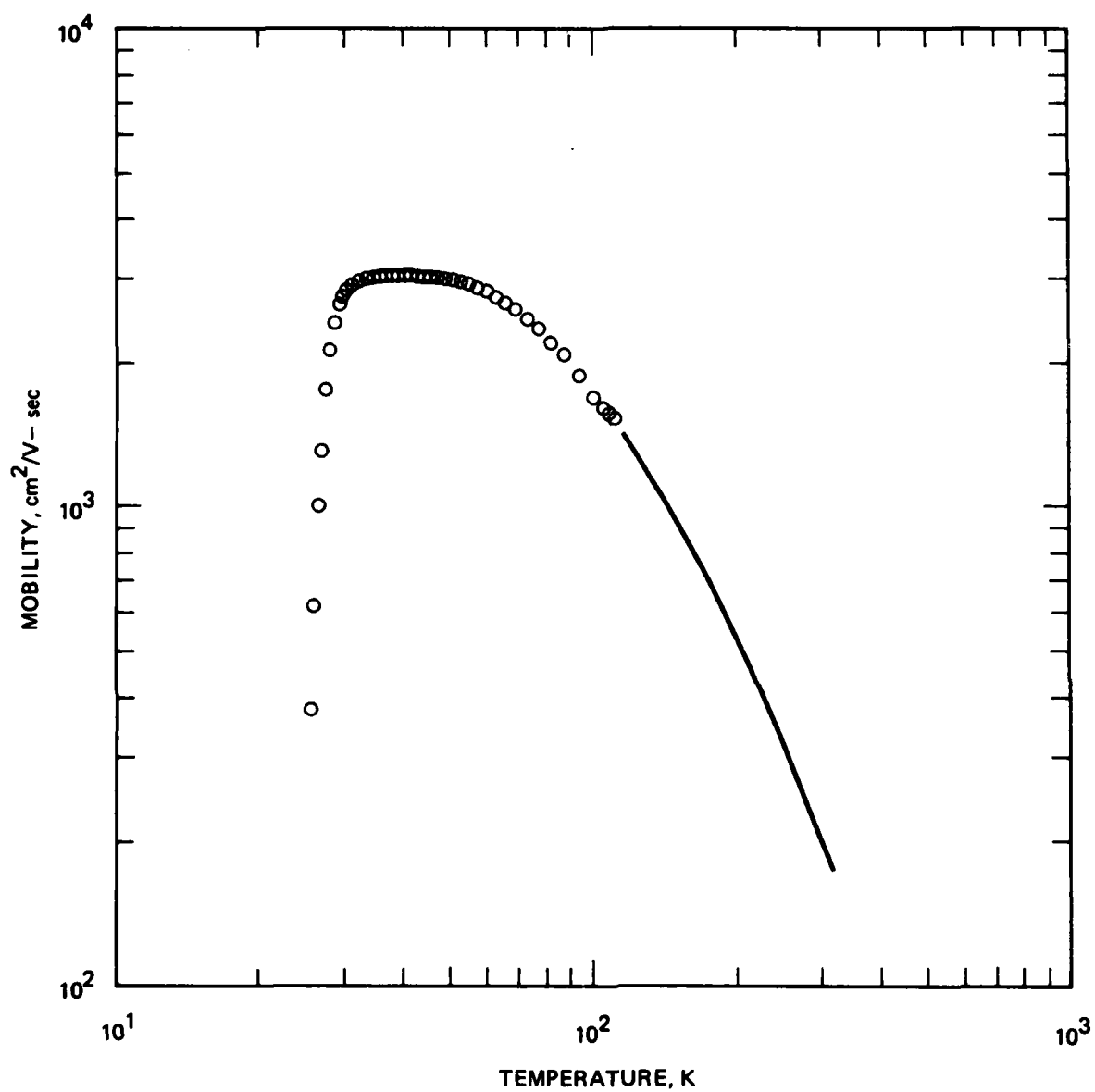Figure 56.   Hole concentration vs 1000/T for
Z207Ga-CRC163

117

Figure 57.   Hall mobility vs temperature for Z207Ga-CRC163 chip.

F. Szmulowicz[26], were used. The expressions derived from Baron for the quantum efficiency appropriate for calculation of responsivity (η_L) and the quantum efficiency appropriate for the calculation of D* (η_{D*}) were used to calculate theoretical values for D* and η_L. The theoretical quantum efficiency is a function of $\alpha\ell$, which is equal to $N_{Ga} \cdot \sigma_{Ga} \cdot \ell$ where $\sigma_{Ga}(\lambda)$ is the optical abrosption cross-section and ℓ is the length along the optical axis. The Ga concentration, determined from Hall effect measurements, was used to calculate theoretical values for η_L for each Si:Ga material tested. In testing the detectors, filters were used to limit incident radiation to the 8 to 12 μm range. A weighted average value for $\sigma_{Ga}(\lambda)$ in this wavelength range was used in the calculation of α. The results of our measurement of σ_{Ga} as a function of λ done during this LADIR materials program and reported in Section 2-I were used in this calculation. Reflection of radiation from the back contact pad was taken into account in this theoretical model, since the CRC163 chips were designed to be "double pass" structures to increase the maximum expected quantum efficiency. The effect of absorption of radiation due to free carrier absorption in the "transparent" p^+ contact regions of the longitudinal detector structure was also taken into account in the model. The expressions for η_L and η_{D*} used to calculate theoretical values for η and D* are

$$\eta_L = \frac{(\alpha\ell)^2 \, (1 - R_1)R_2^{1/2} \, e^{-\alpha\ell}}{(1 - R_1 R_2 e^{-2\alpha\ell}) \, (\tan^{-1}(e^{\alpha\ell}/R_2^{1/2}) - \tan^{-1}(1/R_2^{1/2}))} \quad , \qquad (13)$$

and

$$\eta_{D*} = \left[\frac{8\eta_L \left[\cot^{-1} R_2^{1/2} \, e^{-\alpha\ell} - \cot^{-1} R_2^{1/2} \right]^3}{(\alpha\ell)^2 \left[\frac{\sinh(\alpha\ell - \ln R_2^{1/2})}{2\cosh^2(\alpha\ell - \ln R_2^{1/2})} + \frac{\sinh(\ln R_2^{1/2})}{2\cosh^2(\ln R_2^{1/2})} + \cot^{-1}(R_2^{1/2} e^{-\alpha\ell}) - \cot^{-1}(R_2^{1/2}) \right]} \right] \qquad (14)$$

---

[26] F.Szmulowicz and R. Baron, IR Physics (1980) <u>20</u>, 385

119

The quantities R_1 and R_2 are the effective top and back surface reflectivities for the detector surface, determined by taking into account the "double pass" structure and the expected free carrier absorption in the p^+ contact layers ($\sim 7\%$), as well as the known reflectivity of Si. The theoretical value for D^*_{Blip} is then

$$D^*_{Blip} = \frac{\lambda_p}{2hc} \sqrt{\eta_{D^*}/Q_B} \quad , \tag{15}$$

where Q_B = background flux, λ_p = peak wavelength, h = Planck's constant, and c = speed of light.

The discrete detectors were experimentally tested at Division 72 by measuring signal and noise photocurrents as a function of applied bias and temperature. A background flux of 8.4×10^{15} photons/cm^2-sec was arbitrarily chosen for all testing because it yielded signals of sufficient amplitude for convenient data collection. The experimentally observed quantum efficiency (η_{exp}) was determined from the measured signal-to-noise ratio $\left[(S/N)_{Blip} \right]$ using

$$(S/N)_{Blip} = \frac{(Q_S - Q_B)}{2} \left(\frac{A_d\, \eta_{exp}}{Q_B} \right)^{1/2} \quad , \tag{16}$$

where A_d = area of detector, and Q_S, Q_B = signal, background flux.

The experimental D* is then

$$D^*_{exp} = \frac{\lambda_p}{2hc} \sqrt{\eta_{exp}/Q_B} \quad . \tag{17}$$

The results of this study, plotted in Figure 58, show excellent correlation between theoretical and experimental performance of detector chips over the whole range of Ga doping represented ($2 \times 10^{16} - 2 \times 10^{17}$ Ga/cm^3), and over a wide range of quantum efficiency (η_L) values ($\sim .1$ to .5). The values of η_{exp} and theoretical quantum

120
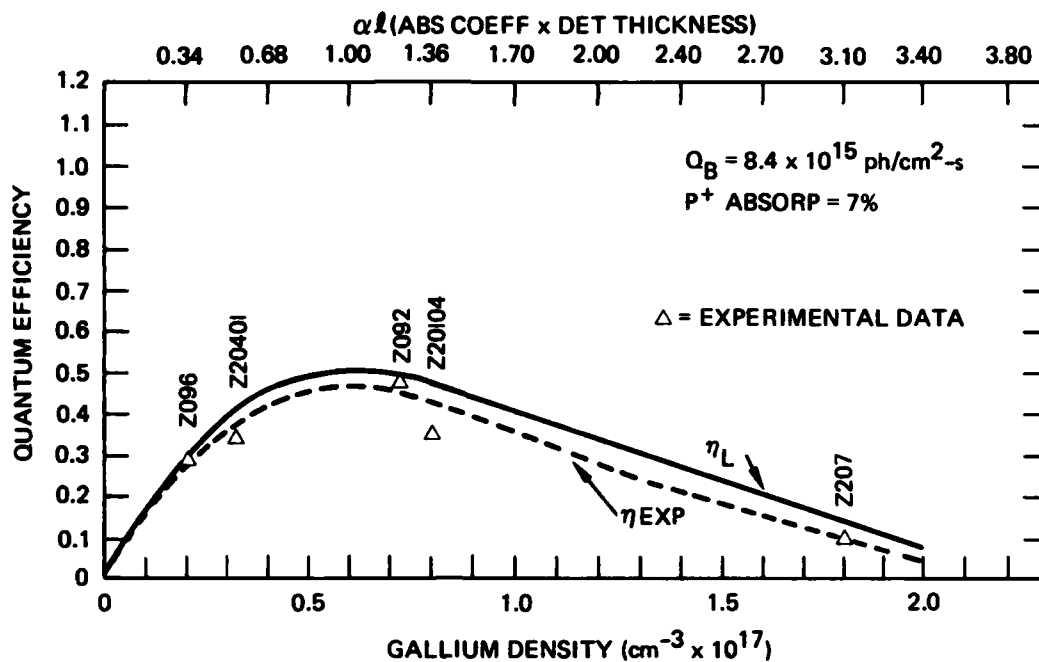
a. THEORETICAL AND EXPERIMENTAL QUANTUM EFFICIENCY vs N_{Ga}
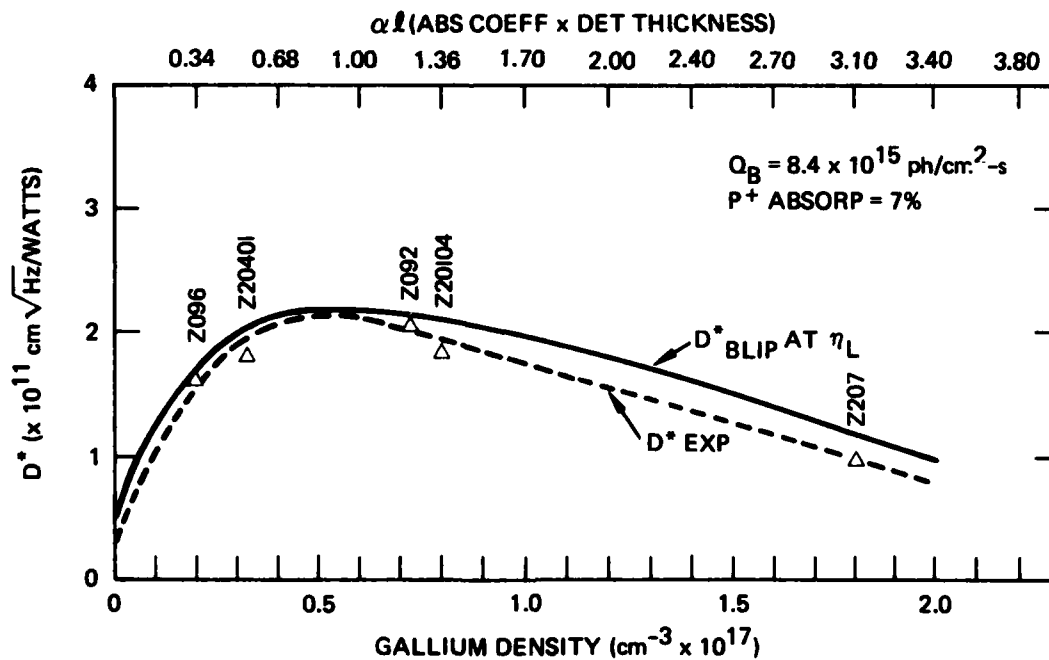
b. THEORETICAL AND EXPERIMENTAL D^* vs N_{Ga}

Figure 58. Theoretical and experimental detector performance at different Ga concentrations.

121

efficiency (n_L) agree within the estimated experimental uncertainty of
~20%. The result of this work, although very limited in scope since it
represents measurements at a temperature of 20K in a very narrow range
of electric field conditions, and at one particular rather high back-
ground of 8.4 x 10^{15} ph/cm^2-sec, clearly demonstrates that the detector
performance of Si:Ga detectors, as reflected in experimentally observed
signal-to-noise ratios, can be accurately predicted using improved
detector modeling and measured material doping parameters. It is
important to point out, however, that many physical mechanisms such as
impurity band conductions, impact ionization breakdown, hot carrier
effects, and Poole-Frenkel effects, that can drastically affect detector
behavior are sensitively dependent on electric field, temperature, and
background conditions. To be able to understand and accurately predict
actual detector operation over a wide range of conditions, we must con-
sider the effect of all of these mechanisms. The scope of the work
reported here did not allow such a full investigation.

2. Impurity Band Conduction Effects

As noted in the previous section, our Hall effect-resistivity
measurements on a Z207Ga-CRC163 FLIR chip doped with ~2 x 10^{17} Ga/cm^3
show the effects of impurity band conduction at low temperatures. In
Figure 59 we have plotted our measurements of resistivity versus 1000/T
for this FLIR chip sample in the "dark" under relatively low electric
field conditions (<40 V/cm). A break in the resistivity slope from the
Ga activation energy slope to the much shallower impurity band conduc-
tion slope at a temperature of about 27K pinpoints the onset of
impurity band conductivity. From the measurements at Division 72 of
photocurrent versus detector bias on the "detector evaluation" half of
this chip, we extracted the resistivity of the material at 20K in
8.4 x 10^{15} ph/cm^2-sec background at the minimum and maximum bias
voltages tested. These values of resistivity are plotted in Figure 59
in order to compare to the measurements on the "Hall effect-resistivity"
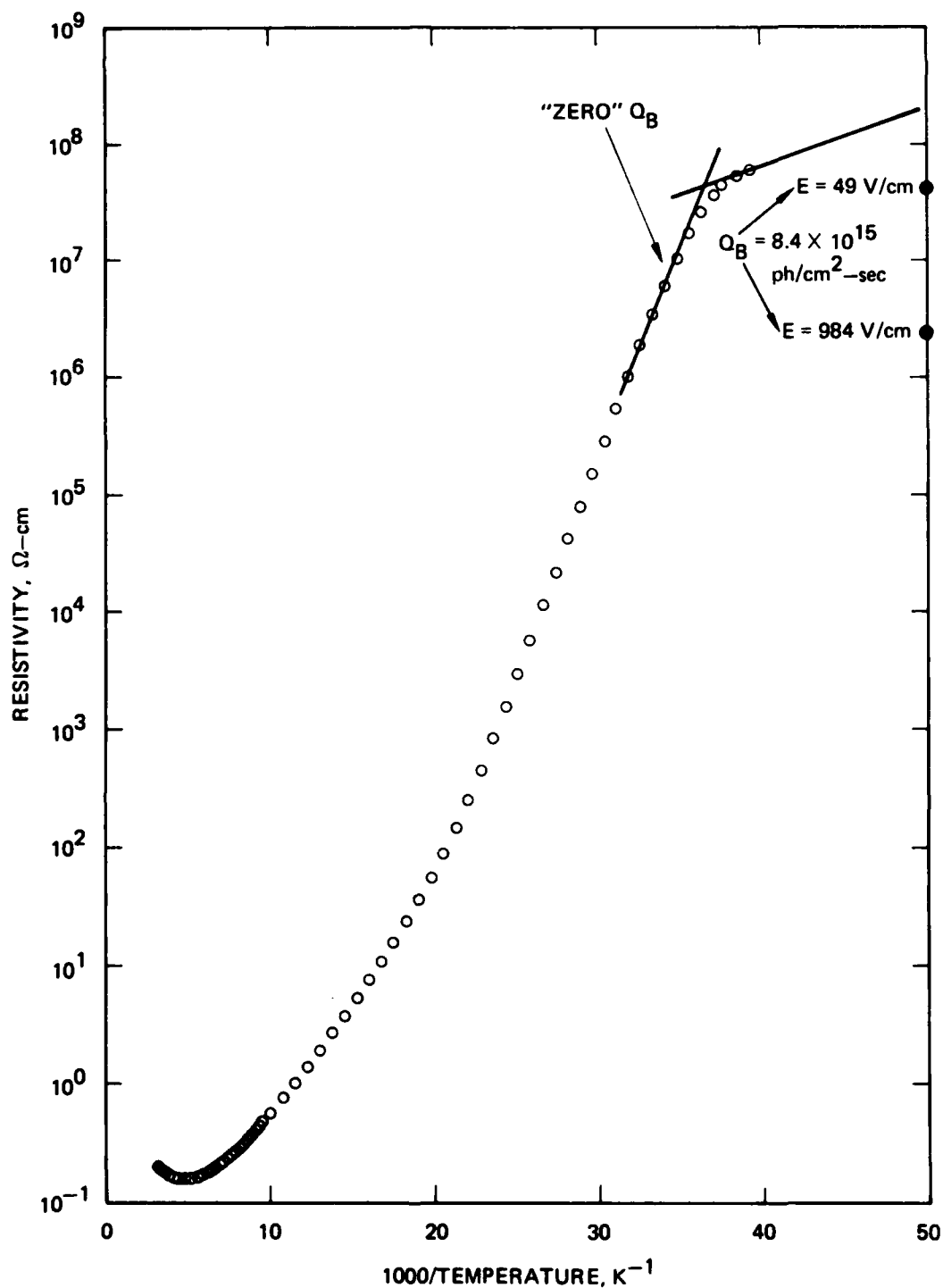half of the chip. The applied bias voltages for these points correspond

122

Figure 59. Resistivity of processed FLIR chip Z207Ga-CRC163 as a function of 1000/T. The sample is measured in the dark under low electric field ($\gtrsim$ 40V/cm) conditions. Also plotted is the measured resistivity of this same detector chip in a background of 8.4 x 10^{15} ph/cm^2-sec at two different electric fields.

123

to electric fields of 49 V/cm and 984 V/cm. In Figure 59 the "dark" resistivity measurements extrapolated out to 20K would indicate that the impurity band resistivity of the material is no greater than 2×10^8 Ω-cm. The observed resistivity in the presence of a photon background (8.4×10^{15}) under low field conditions is $\sim 4.5 \times 10^7$ Ω-cm for the same chip. Thus, the photoconduction process dominates over the impurity band conduction process. Under these conditions, the experimentally observed properties of Z207Ga-CRC163 agree well (within $\sim 20\%$) with the theoretical values, as shown in Figure 58. However, at a background of $\sim 2 \times 10^{15}$, impurity band conductivity would be expected to approximately equal the photoconductivity since photocurrent should scale with the background. Therefore, this Si:Ga material might not be expected to be a useful detector material for applications requiring backgrounds much lower than the Q_B used in this study (8.4×10^{15} ph/cm^2 -sec).

The shift of measured resistivity to lower values at the higher electric field for the photodetector sample in Figure 59 illustrates the sharp dependence of detector operating characteristics on applied bias. Typically, a detector is not in an "ohmic regime" of operation for bias voltages above a few tenths of a volt. Our continuing studies of impurity band conduction under a separate contract (F33615-81-C-5067, Improved LADIR Si:Ga) show that impurity band resistivity also decreases sharply with an increasing electric field. In that contract effort, we are observing impurity band conductivity as a function of doping (Ga, boron, donors). We are also studying the temperature and electric field dependence of the impurity band conduction mechanism, and the relative importance to detector behavior of this mechanism under various background conditions. The results of the on-going program are essential to be able to fully understand and predict the behavior of a chip such as the Z207Ga-163 for specific applications and operating conditions.

3. Detector Contact Evaluation

We evaluated the low temperature sheet resistance of the p^+ boron-implanted layer used to contact the radiation receiving surface of several representative detector arrays. This was done to check that the layers were indeed degenerate and of a suitably low resistance value for proper detector operation at cryogenic temperatures. Table 4 lists the results. None of the measured layers "froze out" at low temperatures, although there is some variation in the measured resistance values. Variability in the early contact fabrication process is shown by the abnormally high resistance for the CRC147 sample; but the fluctuations are greatly reduced in the later samples.

However, from the operation of discrete detectors fabricated from some of the chips, there is evidence that the other p^+ contact layer (on the In-bumped back surface) was not doped as heavily as the front surface, or was partially removed in subsequent processing. This is indicated in asymmetric, non-ohmic behavior of discrete detectors from some chip lots, including the CRC142 chips and CRC156 chips listed in Table 3. There was no evidence of problems with either contact for the CRC163 chips tested in this study.

Table 4

Sheet resistance at 4.2K of p^+ contact layers
for representative FLIR array chips.

Chip	Sheet resistance at 4.2K, $\Omega/\square$
Z20104 (CRC 147)	7007.0
Z20401 (CRC 156)	883.8
Z092 (CRC 156)	772.00
Z20104 (CRC 142)	808.2
Z092Ga (CRC 142)	767.0
Z096Ga (CRC 163)	660.3

APPENDIX A

FLOAT-ZONE CRYSTAL GROWTH

The float-zone (FZ) process for making crystals starts with a high-purity rod of polycrystal silicon and involves several process steps; these steps are modified according to the desired crystal properties. The quality of the polycrystal rod is the ultimate limitation on the final purity of the crystal. The polycrystal material used in growing Si:Ga material is a "specialty grade" silicon polycrystal zone-rod that is selected for its high purity and has a boron concentration of less than $5 \times 10^{12}/cm^3$.

The FZ processing steps are described in Table A-1. Figure A-1 shows the geometry of the molten zone which is passed through the poly-crystal rod to remove impurities. On the final crystal doping pass, a small predetermined mass of Ga is incorporated into the molten zone to provide a concentration in the melt of about 125 times that desired in the doped crystal. As the crystal grows, a small portion (0.8%) of the dissolved Ga is incorporated into the silicon crystal to give the desired doping level. For IR detector applications, the Ga concentration in the final crystal is about 1 part per million.

The FZ technique for growing 2-in.-diameter $\langle 100 \rangle$-oriented Si:Ga, which we have successfully applied to LADIR material preparation in the past, is being used in the present program. Our emphasis is on the choice of growth parameters for the highest possible uniformity. As explained in the body of this report, the uniformity of the boron distribution sets the scale of the ultimately achievable uniformity of responsivity. The lower the average boron content, the more uniform we expect the final gallium-doped phosphorus-counterdoped silicon to be (without requiring so much phosphorus counter-doping that the magnitude of the responsivity is reduced excessively).

127

Table A-1. FZ Processing Steps

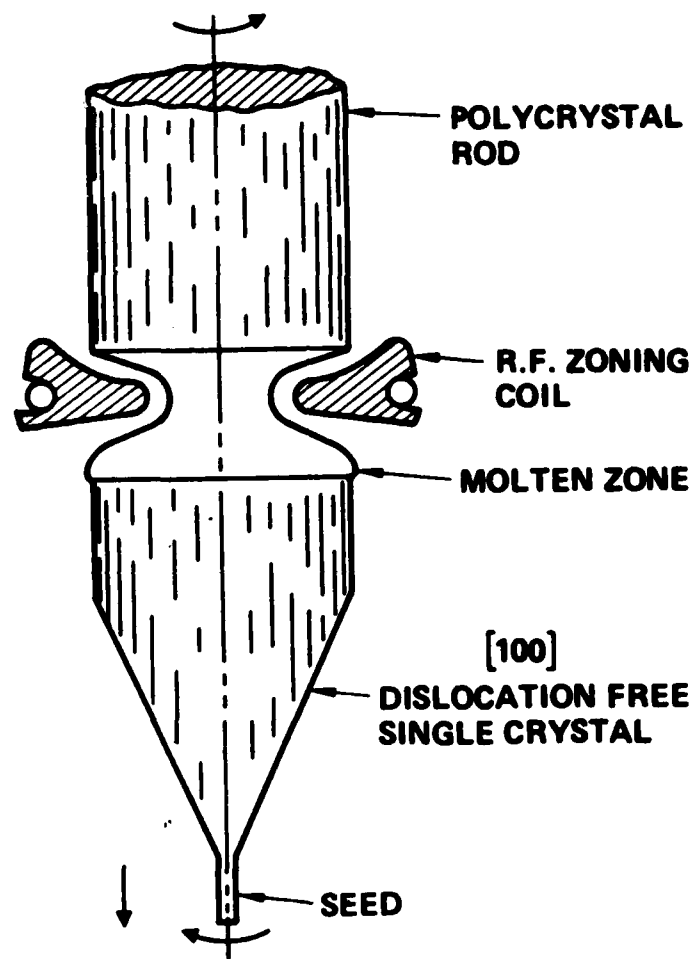| Step No.	Step	Comments
1	Procure high-purity polycrystal rod	N_B and N_p characterized by supplier. These and other properties characterized by HAC from previous growth runs on rods of the same reactor load (of eight-half-rods).
2	Prepurification of polycrystal rod by zoning	Homogenize the polycrystal rod grain structure, remove deep level impurities, and partially remove P by two or more passes in gas or vacuum.
3	Control P counter-doping by partial removal	With polycrystal lots selected for exact initial N_B and N_p, two or or three passes in argon can provide the desired N_p/N_B ratio.
4	Ga seed doping	This is a reproducible, reliable method if the molten zone volume is kept constant and the same zoning conditions are used on each doped crystal.
5	Dislocation-free single-crystal growth, <100> orientation	Must be done in one pass.
6	Evaluate	
7	Fabricate the polished wafer	

Figure A-1. Geometry of the float-zone crystal growth process.

The key factors in reducing the nonuniformity of dopant distribution
are the planarity of the growth interface and the thermal symmetry of
the growth system. We are adjusting the growth parameters to optimize
these factors, working first with the gallium distribution to monitor
the success of the adjustments. Gallium, with a distribution coeffi-
cient much less than unity, is much more sensitive to the factors caus-
ing nonuniformity than phosphorus or boron. We use spreading resis-
tance measurements, striation etching, and Hall-effect measurements
to assess the uniformity.

Various growth parameters affecting the shape of the freezing inter-
face, the boundary-layer thickness, the thermal convection flows, and
therefore the long- and short-range uniformity in FZ growth have been
extensively examined by Keller.* We are following his classification
in investigating the effects of the following growth parameters:

- External zone length
- Seed rotation
- Feed rod rotation
- Eccentric rotation of freezing interface
- Eccentric rotation of melting interface
- RF coil design
- Growth rate.

A. EXTERNAL ZONE LENGTH

The external zone length can be varied by stretching or squeezing
the molten zone, although the range of variation is limited by melt
stability requirements for a 2-in.-diameter crystal. A long external
zone length leads to poor electrical coupling between the coil and the

---

*W. Keller, J. of Crystal Growth 36, 215-231 (1976).

130

melt and, consequently, to small rf field and temperature gradients at
the melt surface. As a result, the external zone length is large
compared to the small internal zone length with a bulging crystal inter-
face toward the melt. Consequently, the radial uniformity is poor,
giving a concentration profile that is high at the center of the crys-
tal. With the proper combination of growth and rotation rates, a
short melt zone having equal internal and external lengths has been
found to give the best uniformity.

B. SEED ROTATION

Rotation of the growing crystal plays an important role in determin-
ing the thickness of the interface boundary layers adjacent to the
crystal and the shape of the interface. Although rapid seed rotation
is advantageous in that it leads to a thinner boundary layer where the
depletion of the accumulated solute atoms depends only on diffusion,
the combination of centrifugal force and the thermal convection pattern
causes the central portion of the freezing interface to bulge. The
optimum rotation rate is dependent on the crystal orientation, the melt
zone length, and the growth rate.

C. FEED-ROD ROTATION

The effect of increasing feed-rod rotation on the growing interface
is similar to that of the seed rotation; increasing rotation rate
decreases the internal zone length and causes the growing interface to
bulge. Counter-rotation of the crystal and feed rod generally gives a
smoother profile with better reproducibility, which may be due to better
stirring action.

D. ECCENTRIC ROTATION OF FREEZING INTERFACE

Eccentric rotation of the crystal can be obtained by moving the
crystal several millimeters to the side from where it would be for con-
centric rotation. With eccentric rotation, the convection flows are no
longer symmetric, which prevents the colder currents from flowing toward

the center and prevents the center of the crystal from bulging. Eccentric
rotation leads to nonstationary convection flows because of the rotation
in an exaggerated asymmetric thermal field, which promotes better mixing
but causes increased microscopic fluctuations.

Asymmetric thermal fields cause all crystals to have rotational
striations, which results in large macroscopic concentration variations
of the dopant and other impurities. Eccentric rotation may find its
rotational axis coinciding with the thermal center, thereby eliminating
the melt-back and the major growth rate fluctuations caused by rotation.
The degree of eccentricity that yields the best uniformity must be
sought for the particular rf coil used.

E. ECCENTRIC ROTATION OF MELTING INTERFACE

Eccentric rotation of the feed-rod must certainly play a role in
determining the flow pattern, and therefore, the shape of the freezing
interface. Variations of the eccentricity may offset the thermal
asymmetry and improve the uniformity.

F. RF COIL DESIGN

The inner coil diameter and the contours (height, inner tapering,
stepping) are important in determining the melt shape, (i.e., the
external and internal zone lengths). A small internal diameter leads to
good rf coupling and a stable molten zone with little tendency toward
spill-over and freeze-out in the center.

Although it is not directly related to coil design, the installa-
tion of an after-cooling ring or a heater below the coil should offer
additional flexibility in shaping the freezing interface. It may
enable us to control the cooling rate of the crystal while it is in
the plastic state; this is an important parameter in reducing the
crystal strain. However, initial experiments with a cooling ring
have not been encouraging.

132

G. GROWTH RATE

Essentially, two growth rates are operating simultaneously during growth: one is the lowering rate of the growing crystal or the feed rod, and the other is the microscopic growth rate. Since the latter arises from transients in the melt, it is more difficult to control. The lowering rate, however, is set by the crystal grower and is dependent on the nature of the dopant and other impurities. In conjunction with other growth parameters, the following factors are affected by the lowering rate:

- Interface shape

- Dopant segregation

- Dopant density.

The interface shape is sensitively affected by the lowering rate because of its effect on the steady-state heat balance. When the heat of crystallization is not efficiently dissipated by radiation and conduction, the center of the crystal becomes hot with respect to the periphery of the melt, and the freezing interface becomes concave. The ideal interface shape (from the standpoint of radial dopant uniformity) is a flat interface. The optimum combination of lowering rate with the rotation rate must be determined experimentally.

Dopant segregation is another factor that is affected by the lowering rate because of the dependence of growth rate on the effective distribution coefficient. The effective distribution coefficient increases with growth rate because of the pile-up of dopant atoms in the boundary layer. The depletion of the dopant from the melt will be faster, the faster the growth rate, which will enhance axial nonuniformity.

The convection flows also are affected by the growth rate. A high growth rate increases the temperature differential between the surface and the center of the melt, thereby increasing the driving force for the thermocapillary flow. The flow can become oscillatory and produce striations.

133

APPENDIX B

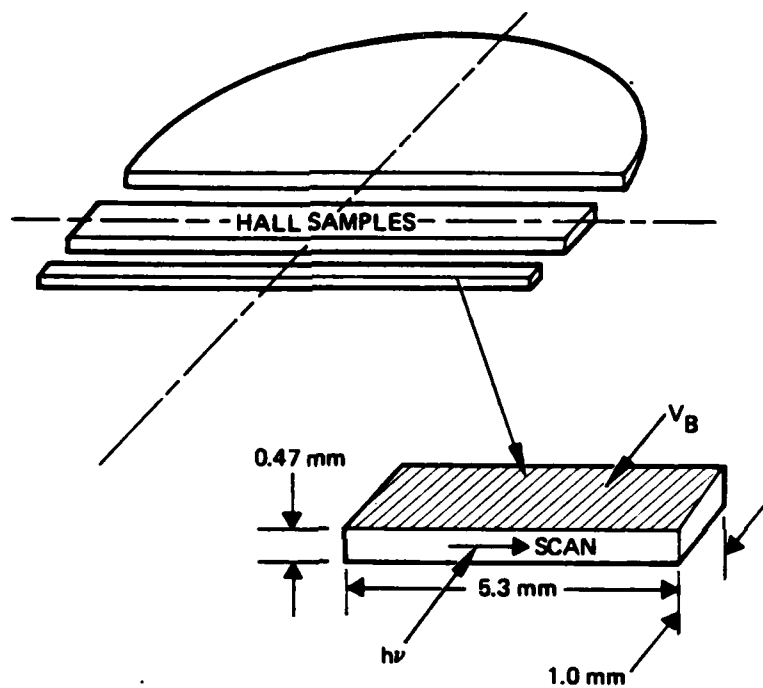## USE OF NEUTRON TRANSMUTATION DOPING TO IMPROVE UNIFORMITY

A. UNIFORMITY OF RESPONSIVITY

An important materials property that has received little previous attention is the uniformity of the distribution of the three major dopants: Ga, B, and donors (P). Their spatial variations in concentration relative to each other directly affect the local detector responsivity and, if the variations are sufficiently large, also the achievable dynamic range of a monolithic focal plane array (MFPA).

Variations in the Ga concentration from detector to detector in the MFPA directly affect IR absorption and therefore the response from detector to detector. Equally important is the uniformity of the net compensation, $N_D - N_B$. A spatial variation in net compensation causes a nonuniformity in carrier lifetime and thus in responsivity. When a detector is operated near the peak of the η versus αd curve, the effect of N_{Ga} variations is minimized, and the $N_D - N_B$ variations become the dominant nonuniformity effect.

Spot scans of detector responsivity can be made to reveal nonuniformity. This technique can be used on Si:Ga material to study the uniformity without waiting for processed MPFAs. Figure B-1 shows the concept of this technique.

The scan system consists of a chopped 500K blackbody source with a movable focusing lens and the detector sample mounted in a variable temperature dewar. The focused spot is scanned across the face of the detector; position information obtained from piezoelectric transducers and the signal output from a lock-in amplifier are plotted on an X-Y recorder, as shown in Figure B-2. Nonuniformities are clearly evident. The bottom trace indicates that the spot was below the sample. The next traces slant upward, indicating that the edge of the sample was not parallel to the horizontal scan line. The variations in the upper left and lower right appear to be due to growth striations.
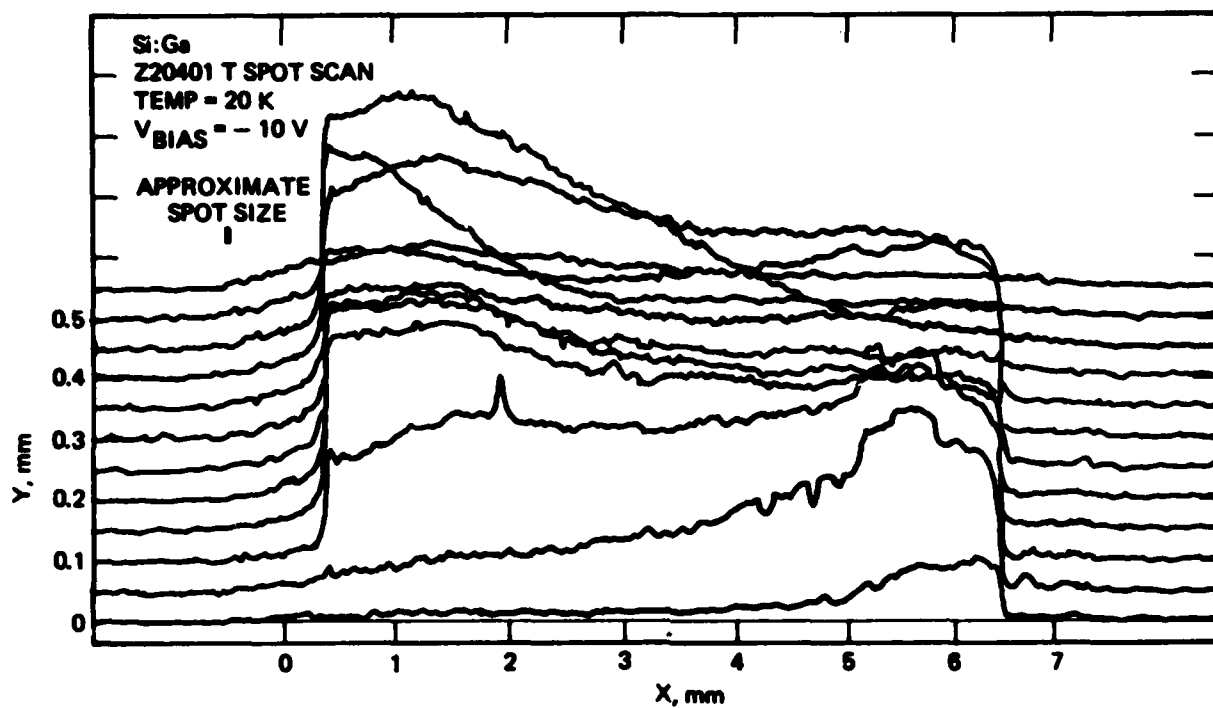
134

Figure B-1. Si:Ga uniformity test sample.

Figure B-2. Spot scans of detector uniformity.

B.   PHOSPHORUS COUNTER-DOPING BY NEUTRON TRANSMUTATION IN Si:Ga

An attractive alternative to the conventional method of preparing Si:Ga for MFPA use is to provide the necessary P counter-doping by neutron transmutation of Si-30 after crystal growth. In a thermal neutron flux, each of the 3 natural isotopes of Si (mass number 28, 29, and 30) can capture a neutron and thus increase its mass number by one unit. Only the Si-31 from the Si-30 (natural abundance = 3.12%) is unstable and decays with a half life of 2.62 hr to the stable isotope P-31. Because the capture cross sections for all the Si isotopes are small (<0.3 barns), the thermal neutron flux is not appreciably altered and the capture probability is uniform throughout even a large crystal. Thus the production of P-31 atoms occurs uniformly within the crystal. A subsequent thermal annealing process is used to remove structural damage to the crystal caused by neutron bombardment and silicon recoils. In principle, a crystal is grown "free" of P, its boron content is evaluated by Hall measurements, and neutron irradiation is applied to produce the desired amount of P. The resulting uniformity of the "phosphorus minus boron" distribution should be determined primarily by the uniformity of the boron distribution. Our experience suggests that this simple picture is essentially correct. Detector structures have been fabricated from neutron transmutation counter-doped Si:Ga and tested with excellent results. Figure B-3 shows the improvement in uniformity of responsivity obtained by neutron transmutation doping.

The neutron irradiations are performed under the direction of Dr. Ron Hart at the Nuclear Science Center at Texas A&M. HRL has set up an IR&D program there to study transmutation in silicon. Studies are being made of the spatial distribution and energy distribution of the neutron flux in that part of the Nuclear Science Center's reactor used for Si transmutation. A comparison has been made of electrically active P obtained versus Si-31 activity observed in irradiated samples. These studies have allowed reliable control of the added P concentration and uniformity for application to extrinsic Si IR detector programs. The nature of the damage produced by irradiation is being investigated and
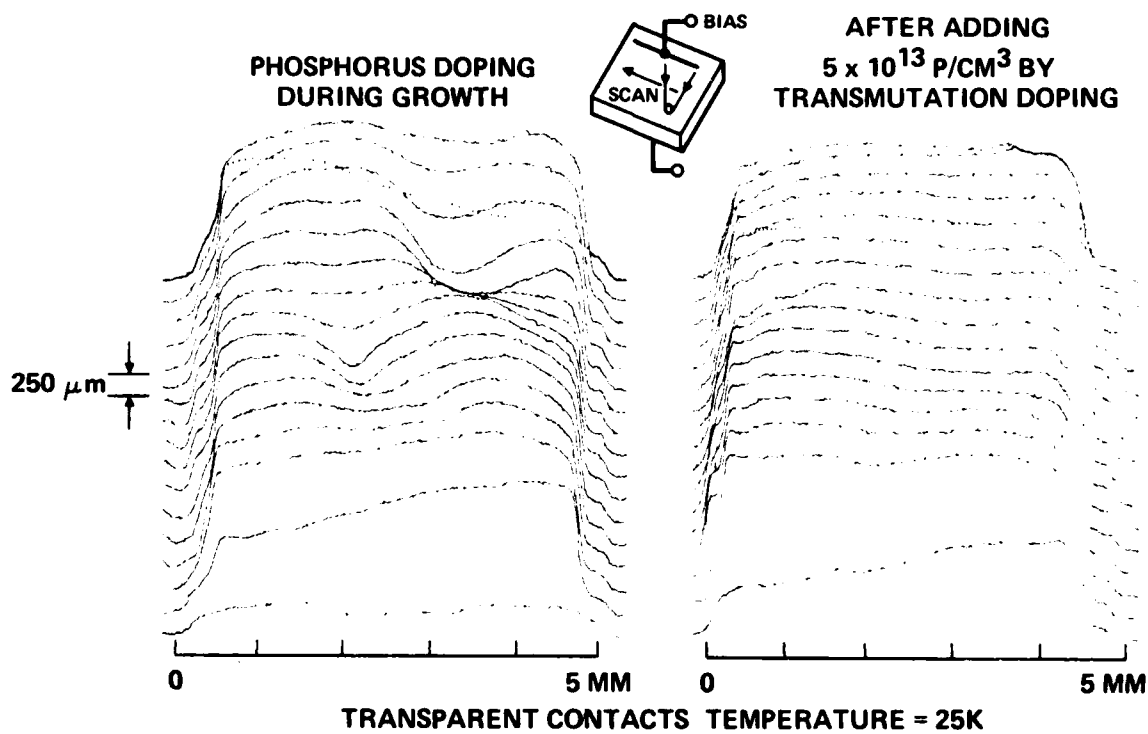
137

Figure B-3. Comparison of responsivity for P-doped Si for conventional growth doping and for neutron transmutation doping.

138

anneal studies are continuing at HRL to determine optimum annealing procedures.

The data presented in Figure B-4 illustrate the effect of neutron transmutation doping on the low-temperature electrical properties of a Si:Ga sample. Before irradiation, the sample was slightly undercompensated ($N_{boron} \gtrsim N_{donor}$). Irradiation conditions were set to overcompensate the boron by approximately a factor of six. After irradiation and annealing, the full slope of Ga (~ 0.072 eV) appears at the lowest temperatures rather than the shallower slope of the incompletely compensated sample.

Qualitative evidence that the low-temperature electrical uniformity of the Si:Ga is improved by transmutation counter-doping is presented in Figure B-5. The resistance ratio illustrated in the figure is plotted versus 1000/T. Non-uniform doping of the Hall sample causes variations in the rate of carrier freeze-out spatially over the sample. At the lowest temperatures, nonuniformity in the "donor minus boron" concentration dominates the behavior. The result is a temperature-dependent resistance ratio for the two geometrically different, four-terminal configurations used in the Van der Pauw resistivity measurement. Two transmutation-counterdoped samples are shown (one annealed at 850°C for 1 hr and the other at 1000°C for 1 hr) along with a typical conventionally doped Si:Ga sample. Full scale on the R_{12}/R_{34} axis represents a 10% variation in the ratio. The result for the sample annealed at 1000°C is encouraging because it indicates that it is possible to maintain good uniformity during high-temperature processing.
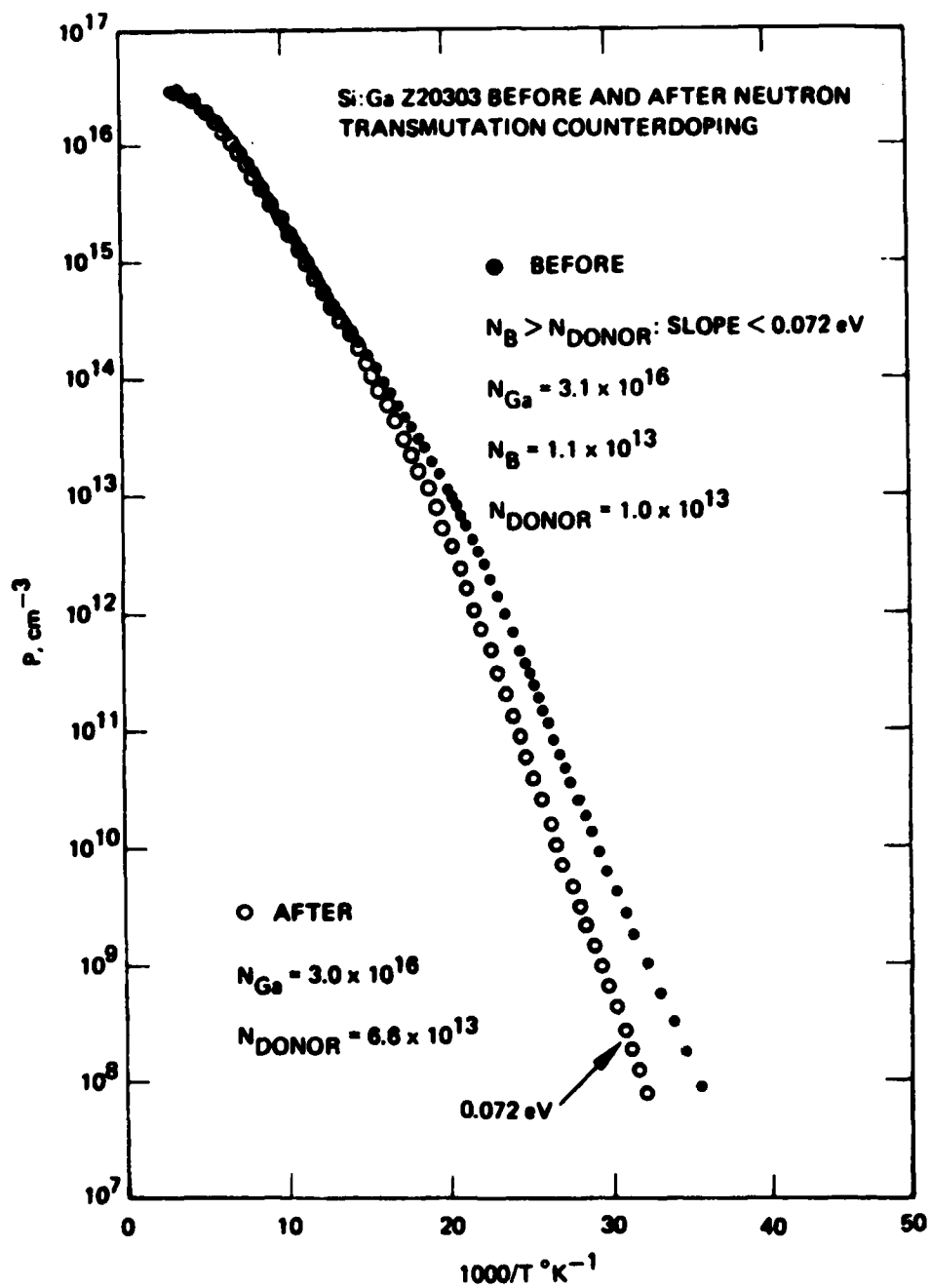
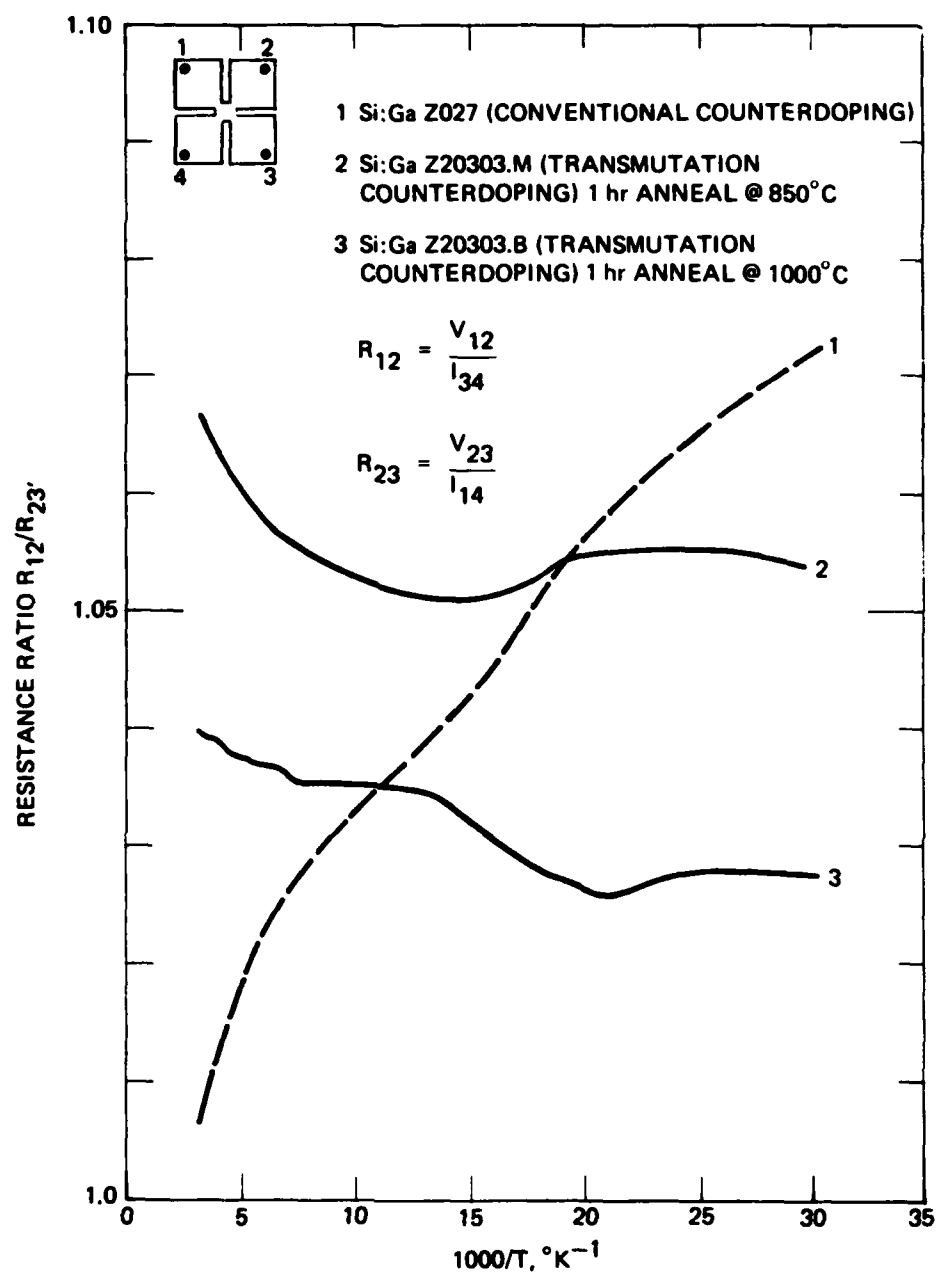Figure B-4. Si:Ga before and after neutron transmutation counterdoping.

140

Figure B-5. Plots of resistance ratio, showing uniformity of doping in transmuted material.

APPENDIX C

EXPERIMENTAL OBSERVATIONS OF IMPURITY BAND CONDUCTION IN Si:Ga

The onset of impurity banding as temperature is reduced
sufficiently is characterized in Hall-effect and resistivity-versus-
temperature measurements by an increase in measured carrier concentra-
tion, a drastic falling-off of carrier mobility (since the mobility
associated with impurity conduction is very low), and a flattening of
the resistivity curve. These features are illustrated in Figures C-1
and C-2, which show Hall-effect data for a heavily doped Si:Ga sample.
The parameter N_{BLIP} shown is the carrier concentration under background-
limited conditions. If the free carrier concentration is higher than
N_{BLIP}, BLIP operation cannot be achieved.

The exact regions of Ga and donor concentrations for which
impurity-band conduction is expected to be decidedly detrimental to
detector operation have not been well defined. In another contract-
funded program and in an IR&D effort, we have begun a study to define
quantitatively the effects of material parameters on the impurity hop-
ping mechanism in Si:Ga. Some of the initial results from this investi-
gation proved to be relevant to LADIR and related programs.

A.   SAMPLE SELECTION AND SAMPLE CONFIGURATION

In our initial studies, the Si:Ga investigated is typical of the
material used in IR detector programs, and the measurement conditions of
temperature and electric field are similar to the IR detector operating
conditions. Figure C-3 shows the matrix of material parameters (N_{Ga} and
net compensation) which we have begun to investigate. As indicated in
the figure, for some samples additional phosphorus was added by neutron
transmutation in order to better understand the effects of compensation
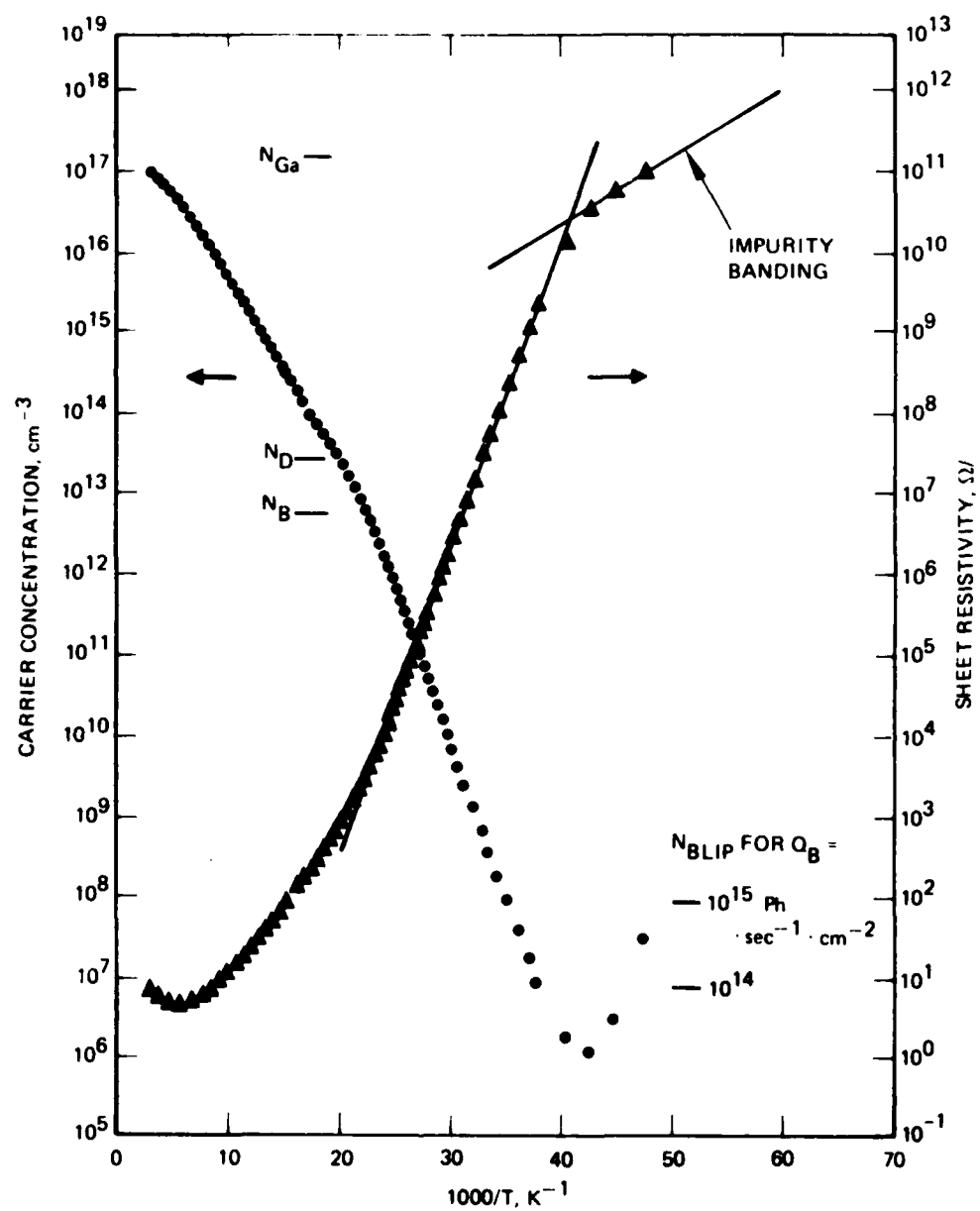on detector transport properties.

Figure C-1. Carrier concentration versus inverse temperature, showing onset of impurity banding.
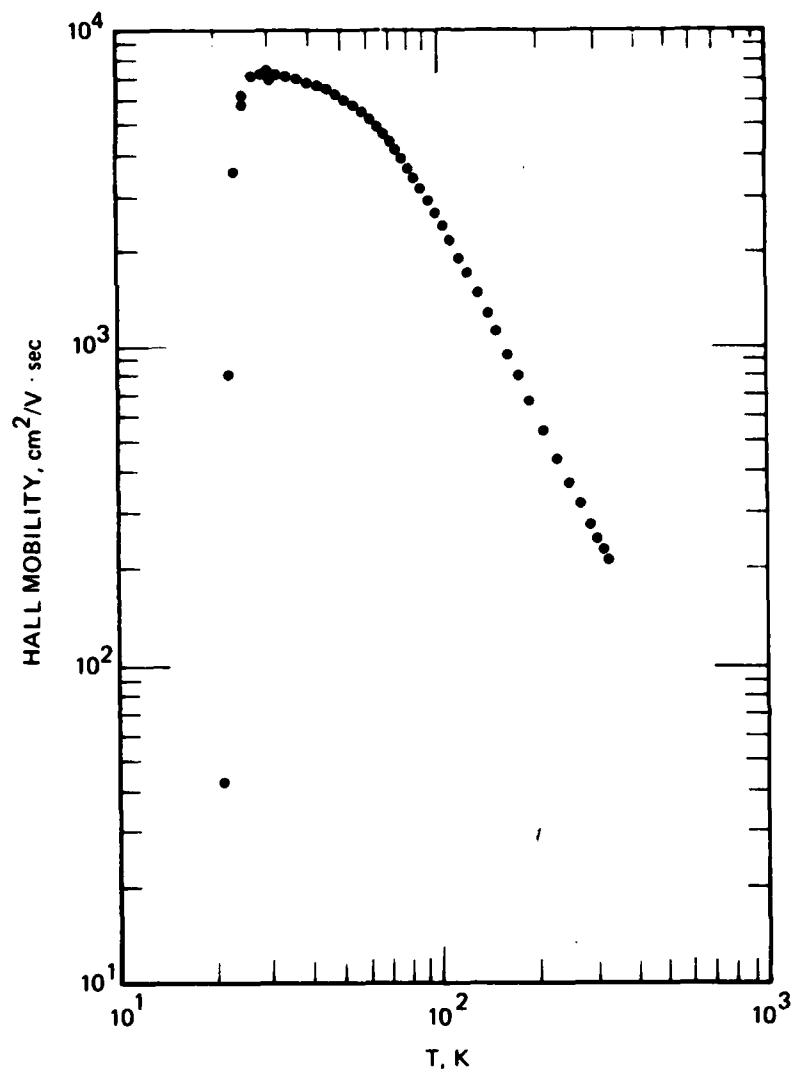
Figure C-2. Carrier mobility versus temperature, showing drastic fall-off in mobility connected with impurity banding.
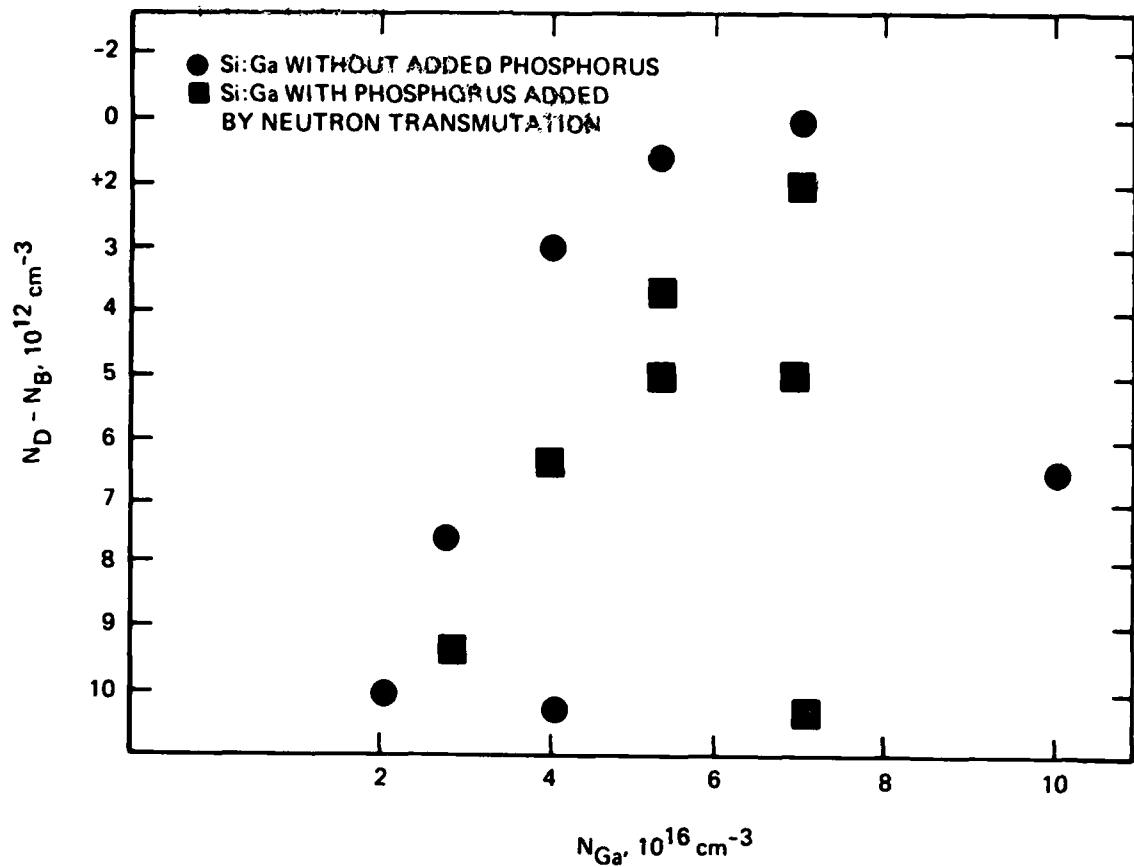
144

Figure C-3. Matrix of samples for impurity band conduction study
in Si:Ga.

Figure C-4 shows the sample configuration used in our studies. The
samples are large-area (1-cm^2) structures (to reduce resistance),
$\sim$15 mils thick, with boron ion-implanted p$^+$ contacts on the top and
bottom. A metalization is applied to the bottom and to a strip on the
top to facilitate contacting the sample. The electrical properties of
the samples can be investigated in "the dark" or with illumination
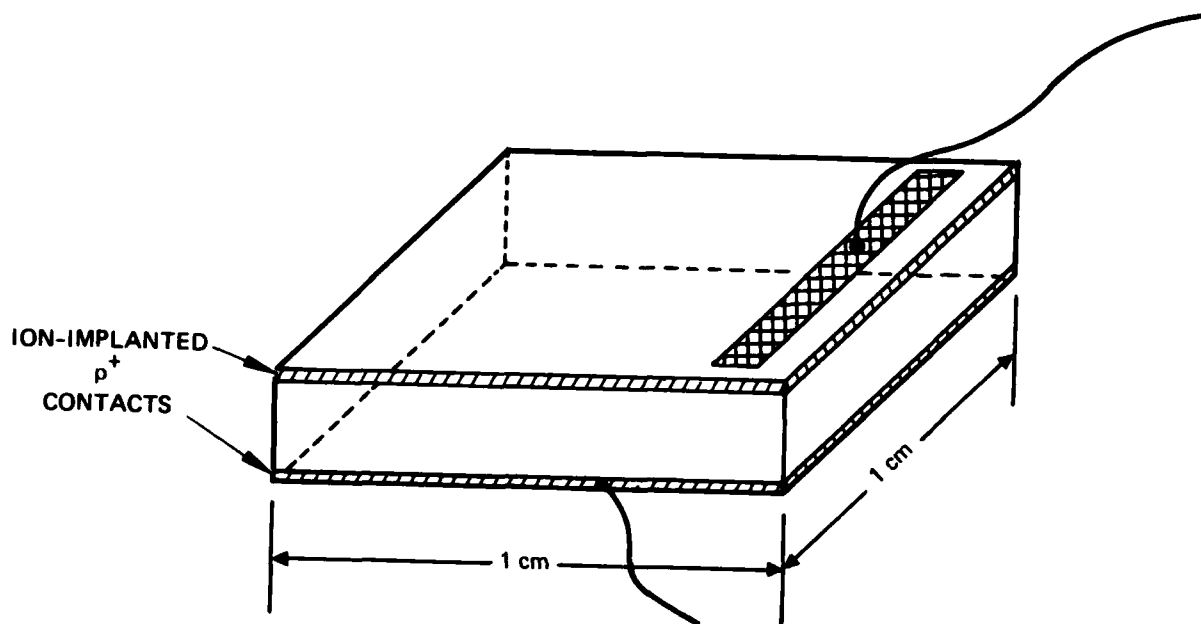through the transparent top contact.

145

Figure C-4. Sample configuration for study of impurity band
conductivity in Si:Ga.

B.   EXPERIMENTAL RESULTS

The measured resistivity as a function of temperature provides the
clearest indication of the onset of impurity hopping conductivity.
Normally, in the regime dominated by thermally generated carriers, the
measured resistivity increases exponentially as the temperature is
reduced with an activation energy close to the Ga energy level
($\sim$0.07 eV). The onset of impurity hopping is marked by a breaking away
of the measured $\rho(T)$ curve from a steep dependence on temperature to a
much shallower slope associated with impurity-hopping-dominated conduc-
tivity. Therefore, to look for the onset of impurity hopping, we have
measured current-voltage (I-V) characteristics as a function of temper-
ature from 4.2 K to approximately 30 K. From these I-V measurements, we
extracted the measured resistivity at chosen bias voltages and then
plotted resistivity versus the reciprocal of temperature, as illustrated

146

in Figures C-5 and C-6. These measurements were made under very low background conditions. Figure C-5 shows ρ versus 1000/T for samples from the seed and tang ends of Z092Ga grown for the FTD-ATAC programs. The doping is $\sim 7 \times 10^{16}$ Ga/cm^3 at the seed and $\sim 5 \times 10^{16}$ Ga/cm^3 at the tang for this crystal. The marked dependence on Ga doping of $\rho(T)$ is clearly illustrated in the data presented in Figure C-5. We also observe a dependence on electric field of the measured resistivity for the samples shown in Figure C-5. Figure C-6 shows similar ρ versus 1000/T data for samples from the seed end of Z092Ga ("as grown" as well as with additional compensation added by transmutation). A strong dependence on compensation level is indicated in these initial results.

Whether impurity-hopping conductivity will interfere substantially with the observation of photogenerated conductivity depends primarily on the background and temperature of operation of the detector. For example, at 25 K and at a background of 5×10^{15} photons/sec-cm^2, the resistivity due to photogenerated carriers is expected to be between 10^6 and 10^7 Ω-cm, which is lower than the impurity-hopping resistivity for the more lightly compensated samples shown in Figure C-6. The conductivity due to the background radiation might be expected to dominate under these conditions, as desired for proper detector operation, but experimental verification of this is needed. Further work planned in this area will allow a more precise determination of the doping parameters required for optimum detector operation under specific conditions of background, temperature, applied electric field, and frequency of operation.
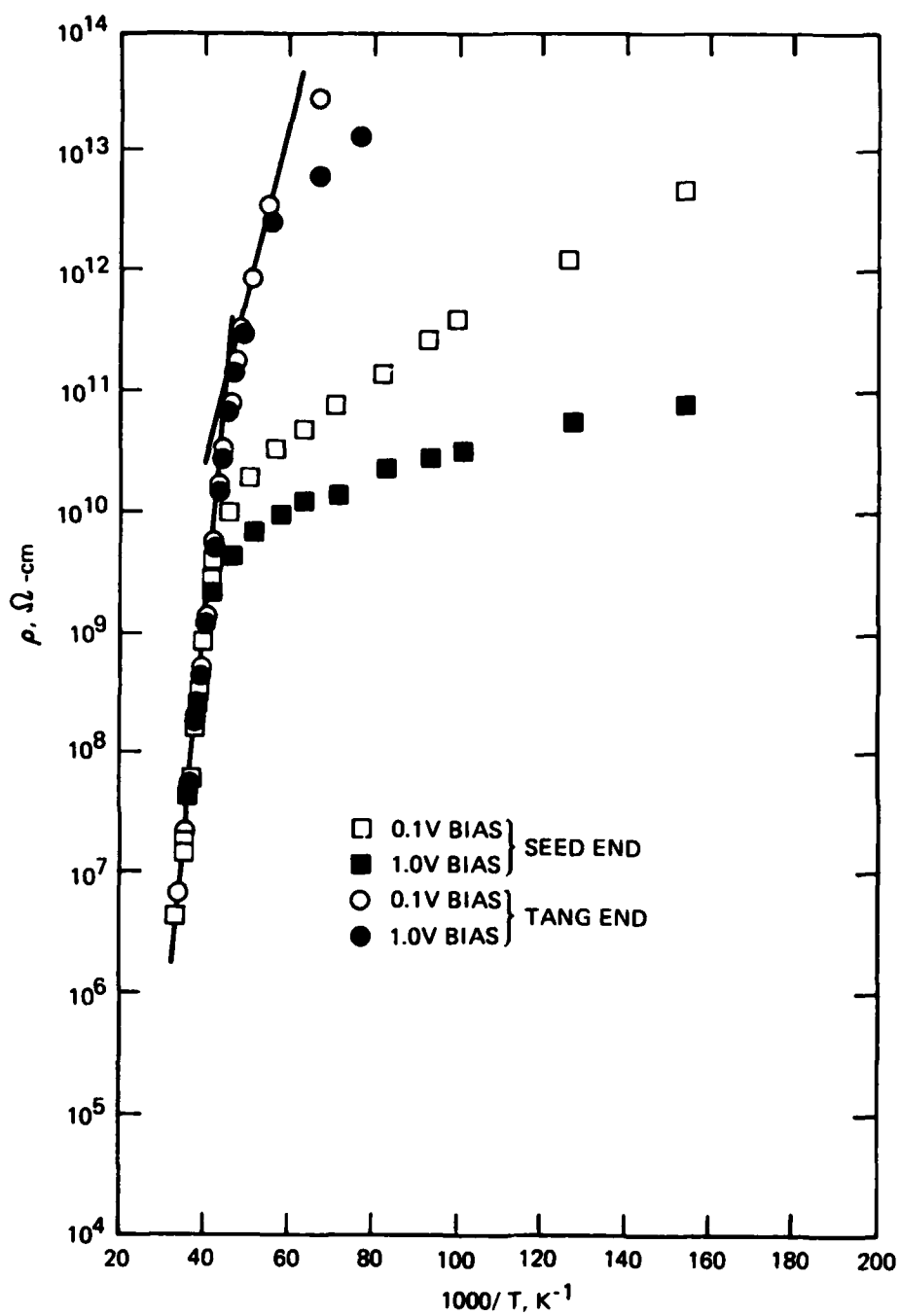
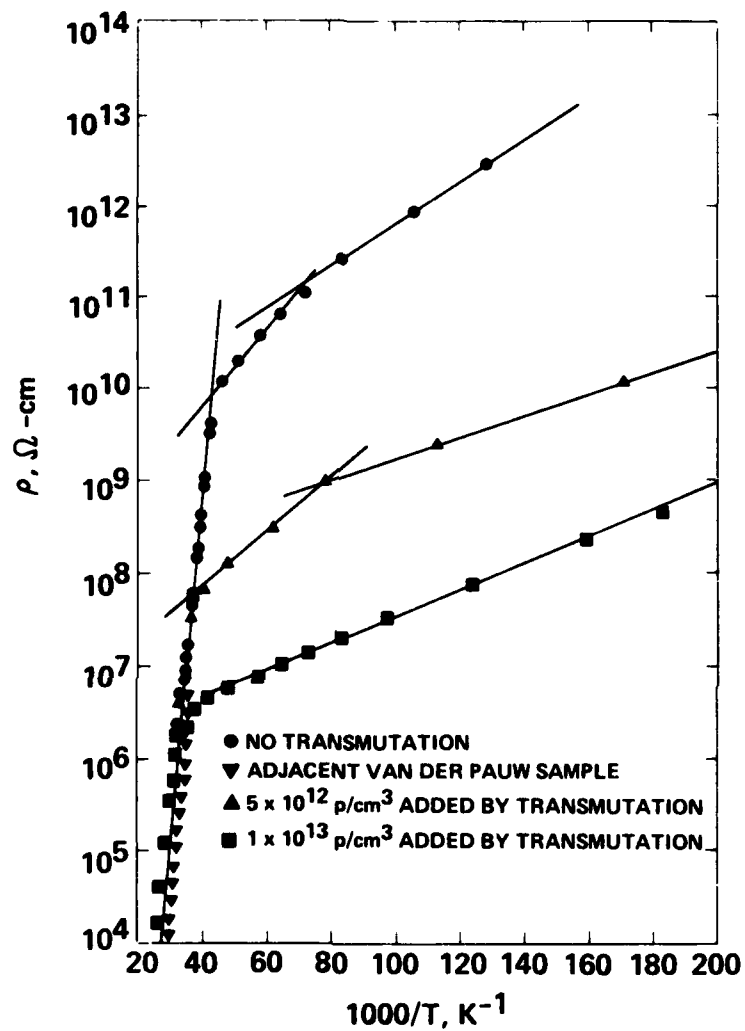Figure C-5. Resistivity versus 1000/T measurements for crystal Z092 Ga.

Figure C-6. Resistivity versus 1000/T measurements
for FTD ingot seed end doped with
7×10^{16} Ga/cm^3.